Short-term irradiance nowcasting based on camera and satellite images

Philipp Gregor

München 2023

Short-term irradiance nowcasting based on camera and satellite images

Philipp Gregor

Dissertation
der Fakultät für Physik
der Ludwig-Maximilians-Universität
München

vorgelegt von
Philipp Gregor
aus Marktoberdorf

München, den 06.07.2023

Erstgutachter: Prof. Dr. Bernhard Mayer
Zweitgutachter: Univ.-Prof. Mag. Dr. Martin Weissmann
Tag der mündlichen Prüfung: 26.09.2023

Contents

Zusammenfassung

Der Ausbau der erneuerbaren Energien ist ein entscheidender Beitrag zum Klimaschutz. Dabei ist Photovoltaik (PV) eine der am weitesten verbreiteten Quellen für sauberen und nachhaltigen Strom. Die Stromerzeugung durch PV hängt allerdings in hohem Maße von der solaren Einstrahlung ab und ist damit anfällig für atmosphärisch bedingte Schwankungen. Innerhalb einzelner Minuten können Wolken auch ausgedehnte PV-Anlagen beschatten, was zu Fluktuationen in der Stromerzeugung führt. Diese Schwankungen stellen eine Herausforderung für die Stabilität der Stromnetze dar. Die genaue Kenntnis der zu erwartenden Einstrahlung trägt zur verbesserten Nutzbarkeit von PV-Strom bei. Daher sind kurzfristige Prognosen der Einstrahlung erforderlich, diese werden auch Nowcast genannt. Wolkenbilder können als Grundlage für Nowcasts der nächsten Minuten und Stunden genutzt werden. Diese werden analysiert, um Position, Bewegung und, wenn möglich, auch die optischen Eigenschaften von Wolken abzuleiten. Mit Fischaugenkameras, sogenannten all-sky imagern (ASI), können lokal Wolkenbilder in hoher zeitlicher und räumlicher Auflösung aufgenommen, aber nur bedingt die optischen Eigenschaften abgeleitet werden. Multi-spetrale Bilder von geostationären Meteosat Second Generation (MSG) Satelliten erlauben die Ableitung von wolkenoptischen Eigenschaften bei großer räumlicher Abdeckung, sind allerdings nur in grober Auflösung von einigen Kilometern verfügbar. In dieser Arbeit wird MACIN vorgestellt, ein neuartiges Modell für das Nowcasting von Direktstrahlung, das durch eine von der Datenassimilation inspirierte Methode verschiedene Beobachtungen nutzen kann. MACIN kann beispielsweise Bilder von mehreren Kameras und Zeitpunkten verwenden. Wolkenmasken werden mit einem neuronalen Netz (CNN) aus Kamerabildern abgeleitet und mittels Stereographie wird die Wolkenhöhe ermittelt, wodurch die Position von Wolken über einer PV-Anlage berechnet werden kann. Aus aufeinanderfolgenden Bildern wird die Wolkenbewegung bestimmt, wodurch die Wolkenposition extrapoliert werden kann. Mit aktuellen Einstrahlungsmessungen können Nowcasts der Direktstrahlung aus den prognostizierten Wolkenfeldern berechnet werden. Eine Erweiterung des eingeführten Modells nutzt zusätzlich MSG-Satellitenbilder, um die wolkenoptischen Eigenschaften genauer zu bestimmen. Zur Validierung und Evaluierung wurde MACIN auf synthetische Bilder von simulierten Wolken und reale Beobachtungen angewendet. Das neue Strahlungstransportmodell LASCAT wurde eigens zur schnellen Berechnung synthetischer Bilder eingeführt. Die erfolgreiche Validierung der abgeleiteten Wolkeninformation ergab eine Genauigkeit der Pixelklassifizierung der Wolkenmasken von über 94 %, einen relativen Fehler der Wolkenhöhe im Bereich von 4 % und einen Fehler der Wolkenbewegung von etwa $\pm 0.1\,\mathrm{m\,s^{-1}}$. Die Nowcasts der Direktstrahlung zeigen signifikante Verbesserung gegenüber der Persistenz. Experimente mit den synthetischen Daten beleuchten den Einfluss der Wolkenentwicklung und der ASI-Bildgeometrie auf den Vorhersagefehler. Nowcasts mit dem erweiterten Modell zeigen zusätzliche Verbesserungen und demonstrieren das Potential des vorgestellten Modells verschiedene Beobachtungen wie Kamera- und Satellitenbilder gewinnbringend zu kombinieren.

Abstract

The transition towards renewable energy is crucial to address climate change. Photovoltaic (PV) power is one of the most widespread and promising sources of clean and sustainable energy. However, PV power production is highly dependent on incident irradiance, making it susceptible to fluctuations caused by atmospheric conditions. Clouds can shadow PV power plants in a single minute, leading to highly variable power production. This intermittency challenges the stability of power grids with high penetration of PV. Accurate knowledge of upcoming fluctuations can help to tackle this challenge. Therefore, short-term predictions are required, nowcasts of incident irradiance. Nowcasts of the next minutes to hours can be derived from cloud images analyzed to retrieve position, motion, and possibly also optical properties of clouds. On-site all-sky imagers (ASIs) capture cloud images in high spatial and temporal resolution, but usually allow only limited retrievals of cloud optical properties. Meteosat second generation (MSG) geostationary satellites provide multi-spectral images, which offer large spatial coverage at the cost of kilometer scale resolution. Cloud optical properties can be derived from these multi-spectral images. This work proposes a novel model for all-sky image based cloud and direct irradiance nowcasting (MACIN) that can make use of various observations with a method inspired by data assimilation. MACIN is designed to use images from multiple ASIs and multiple times. Cloud masks are generated from images using a convolutional neural network (CNN) and cloud-base height is derived by stereography. The derived cloud information is utilized in MACIN to describe cloud positions above the PV plant. Cloud motion derived from consecutive images is used by MACIN to extrapolate the cloud positions up to lead times of 30 min. Latest on-site irradiance measurements allow deriving direct normal irradiance (DNI) nowcasts according to the extrapolated cloud positions. An extended MACIN-S makes additional use of MSG satellite images for an enhanced estimate of cloud optical properties. MACIN is thoroughly validated using synthetic ASI images of modeled cloud scenes and also evaluated on real data. This work introduces LASCAT, a novel model for 3D radiative transfer. It is used for the fast computation of required synthetic images. Cloud masks achieving over 94 % accuracy, relative cloud-base height errors of approximately 4 %, and cloud motion errors within a range of $\pm 0.1\,\mathrm{m\,s^{-1}}$ demonstrate the quality of derived cloud information in the synthetic setup. DNI nowcasting performance surpasses a persistence baseline nowcast, and particularly errors for large nowcasted areas reduce. Synthetic experiments shed light on the impact of cloud evolution and ASI viewing geometry on nowcast performance. Evaluation of MACIN-S DNI nowcasts showcases the strength in the design of the proposed nowcasting model. The approach inspired by assimilation allows for the integration of additional MSG satellite observations, which improve nowcast performance. Although nowcasting direct irradiance is the main focus of this work, it also highlights the potential benefits of MACIN-S for PV power nowcasting. In summary, this work presents an innovative approach for nowcasting direct irradiance based on camera and satellite images. Comprehensive validation in a synthetic setup and evaluation on real data highlight the potential of MACIN and MACIN-S in addressing the challenges associated with fluctuating PV power production.

Chapter 1

Introduction

Climate change requires the increased use of renewable energy. Photovoltaic (PV) and concentrating solar power (CSP) plants are an important contribution. As of 2022, a total of 67.4GW PV peak power was installed in Germany, producing 60.8TW h over the course of the year (UBA, 2023). This contributed more than 11% to the countries electric energy consumption in 2022. While PV plays an important role in power production, it comes with the major drawback of volatility due to weather and the position of the Sun. The Sun's position can be calculated precisely for any desired time and location on Earth. More challenging to predict are short-term fluctuations in PV power production due to cloud shading. These fluctuations are challenging for grid integration of PV (Katiraei and Agüero, 2011). They may cause grid instabilities and require the allocation of reserve power plants or storage for compensation. Short-term predictions – so-called nowcasts – of irradiance for the next minutes to hours can help with improved grid integration of PV (e.g.; West et al., 2014; Law et al., 2016; Boudreault et al., 2018; Saleh et al., 2018; Samu et al., 2021; Chen et al., 2022). The NETFLEX project investigated the potential of such predictions for the intelligent management of biogas power plants in regional grids with high PV penetration. A subproject focused on nowcasting of irradiance for a combined PV and biogas power plant as described in this work.

Many nowcasting systems make use of images of the current cloud situation (e.g.; Peng et al., 2015; Schmidt et al., 2016; Sirch et al., 2017). These images are processed to derive position, motion, and, if possible, also optical properties of clouds. On the basis of the current cloud motion, they predict future cloud positions and estimate the corresponding irradiance. Cloud images can be captured with satellite instruments or ground-based fisheye cameras, also known as all-sky imagers (ASIs). They offer cloud imagery from below in high spatial and temporal resolution but with limited spatial coverage. ASIs are often affordable consumer-grade cameras, which are not spectrally calibrated and provide only limited information about the optical properties of clouds. ASI-based nowcasting models are usually designed for minute-ahead nowcasting. Many ASI-based irradiance nowcasting systems have been proposed over the years (e.g.; Peng et al., 2015; Schmidt et al., 2016; Kazantzidis et al., 2017; Nouri et al., 2022), which derive cloud masks and cloud motion from images, extrapolate cloud positions, and estimate future irradiance. Setups with multiple ASIs have become feasible due to the availability of consumer-grade fisheye cameras, which are inexpensive and weather resistant. Simultaneous images from different ground positions can be exploited to derive cloud base height (Nguyen and Kleissl, 2014; Beekmans et al., 2016; Kuhn et al., 2018). An even more precise three-dimensional (3D)

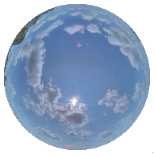

representation of clouds is derived by Nouri et al. (2018) from a setup with four ASIs using a technique called voxel carving. Rodríguez-Benítez et al. (2021) deployed three ASIs for independent irradiance nowcasts per imager, which were averaged into a single mean irradiance nowcast. The Eye2Sky network of dozens of ASI distributed in northwestern Germany was established for spatial observation of the cloud situation and nowcasting (Blum et al., 2021). This ASI network can be used, for example, to derive the spatial distribution of irradiance (Blum et al., 2022).

Commercial PV and CSP plants often span hundreds of meters, while irradiance is measured by single devices with sensors covering only a few square centimeters. Irradiance nowcasts are commonly validated against localized irradiance measurements, which is in contrast to the reality of spatially extent PV plants. Kuhn et al. (2017a) developed a method to derive irradiance maps from a camera that monitors the shadows on the ground. These area irradiance maps were used in Kuhn et al. (2017b) to validate irradiance nowcasts for the area of a CSP. Nowcast improvements over persistence were found, especially for situations with large variability. Multiple irradiance measurements distributed over an area of approximately 1 km were used as a reference by Nouri et al. (2022). They found smaller nowcast errors if nowcasted and measured irradiances for all sites were averaged before comparison. This indicates that nowcast errors for areas can be smaller than for a single point.

A major challenge in nowcasting based on ASI is the identification of clouds in images to create cloud masks. Li et al. (2011) proposed a method based on pixel color ratios and histogram thresholding for the computation of cloud masks. The large field of view of ASIs comes with varying sky color within single images, even under cloud-free conditions. An additional clear sky library, a library of cloud-free images, can be used to extend the method and account for these intra-image background variations (e.g.; Shields et al., 2009; Chow et al., 2011; Schmidt et al., 2016). More recently, advances in convolutional neural network (CNN) based image segmentation have been exploited for the derivation of cloud masks. Multiple studies demonstrated the use of CNNs for cloud image segmentation and irradiance nowcasting (Ye et al., 2017; Dev et al., 2019; Xie et al., 2020; Hasenbalg et al., 2020). Fabel et al. (2022) trained a CNN to segment cloud images into clouds in three height layers instead of a binary cloud or cloud-free segmentation. Masuda et al. (2019) developed a technique to derive cloud optical depths from ASI images. They combined synthetic cloud images of modeled cloud scenes, a spectral camera model, and a CNN. A synthetic setup was also used by Kurtz et al. (2017) based on high-resolution large eddy simulations (LES) of clouds and synthetic ASI images of these clouds. The synthetic setup allows for extended validation of developed methods, as the geometry and properties of the imaged clouds are known perfectly. Furthermore, experiments for the investigation of error sources can be designed with the synthetic setup. For example, Kurtz et al. (2017) investigated errors due to the viewing geometry of ASIs with the synthetic setup.

In contrast to ASI images, satellite-based imagery offers the advantage of larger spatial coverage and multispectral information. Meteosat second generation (MSG) geostation-

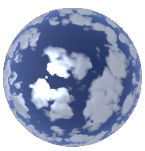

ary satellites offer continuous reflectance measurements for Europe. However, the spatial resolution is on the order of multiple kilometers. The larger spatial coverage allows for larger nowcast horizons. Therefore, satellite-based nowcasting models are usually designed for hour-ahead nowcasting (e.g.; Wang et al., 2019; Hammer et al., 2015; Sirch et al., 2017). Attempts have been made to bring ASI and satellite cloud information together for improved nowcasting. Sirch (2018) used high spatial cloud outlines from ASI images to potentially improve satellite-derived cloud positions in a direct normal irradiance (DNI) nowcasting model. However, no benefits were found. A CNN with elaborate structure was trained in Paletta et al. (2023) to make use of time series of satellite and ASI images together to improve irradiance nowcasting. They found an improved nowcast performance of combined satellite and ASI-based nowcast over nowcasts based exclusively on ASI images for lead times of about 20 min and more. Another way of combining satellite-based and ASI-based nowcasts is suggested by López-Cuesta et al. (2023). They compute independent satellite- and ASI-based nowcasts in this approach, and merge them with a random forest into a combined nowcast. For lead times less than 50 min, significant improvements in nowcast performance were found.

Commonly nowcasted irradiance quantities are global horizontal irradiance (GHI) and DNI. In general, irradiance is the radiative power on a horizontal unit area and can be divided into direct and diffuse irradiance. DNI accounts for all light coming directly from the Sun without scattering in the atmosphere on a plane perpendicular to the incident direction. Diffuse horizontal irradiance (DHI) accounts for all light scattered at least once in the atmosphere and incident in a horizontal plane. GHI is the sum of diffuse and direct irradiance in a horizontal plane. DNI is directly influenced by clouds and the atmosphere in line of sight towards the Sun. DHI depends on the complex 3D-radiative transfer through the atmosphere, e.g., also the constellation of clouds. Fig. 1.1 gives irradiance measurements for three example days, a clear-sky day without clouds, a fully occluded day with constant cloud cover, and a day with broken clouds. For clear situations, as shown in Fig. 1.1a, mainly the daily cycle is important for the prediction of irradiance. For overcast conditions, as depicted in Fig. 1.1b, DNI can be constantly shaded and variations in optical properties of the dense cloud layer cause DHI variations. PV power production is related to global irradiance, which is significantly lower under overcast conditions. With the overall small PV power production, fluctuations in DHI pose a smaller challenge to grid stability in overcast conditions than variations in DNI for broken cloud situations. Fig. 1.1c shows a day with broken clouds and GHI ramps of several hundred $\mathrm{W\,m^{-2}}$ in a single minute. Such situations pose a major challenge due to the large variability in PV power and the possibly large contribution of PV to the overall power production. Although also DHI fluctuates for broken cloud situations, these fluctuations are usually smaller in magnitude and less rapid than for DNI. In this case, the fastest and largest changes in GHI can be mainly attributed to fluctuations in DNI. Therefore, irradiance nowcasting often focuses on DNI first and less on DHI (Chow et al., 2011). This work focuses on DNI for the same reason; in the outlook, an extension to the nowcasting of GHI and PV power is given.

This work introduces a novel model for all-sky image based cloud and direct irradiance

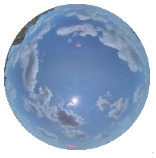

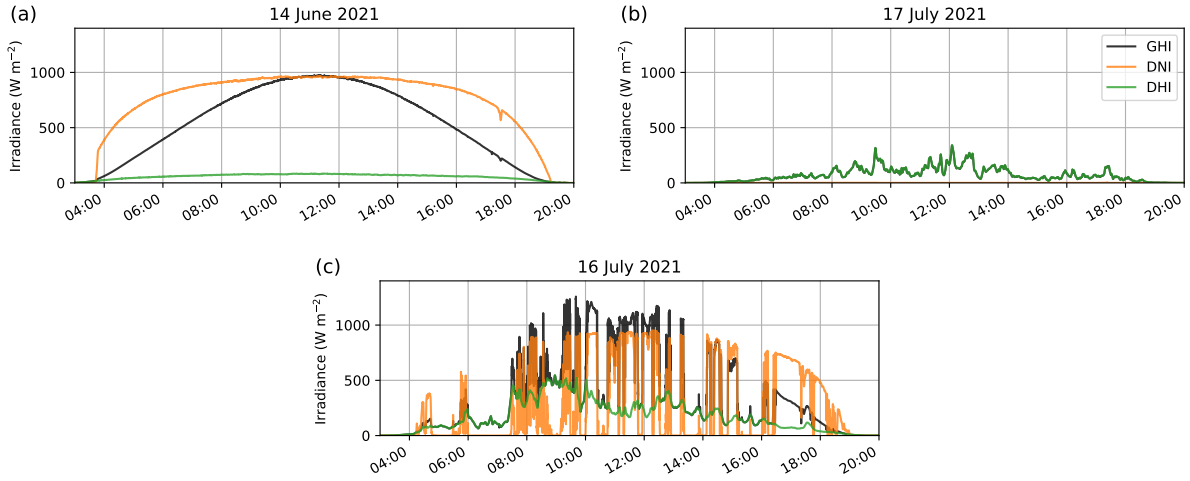

Figure 1.1: Measurements of global, direct and diffuse irradiance in Egling a.d. Paar for 3 example days in June and July 2021. Irradiance measurements indicate **(a)** clear-sky conditions on 14 June 2021, **(b)** overcast sky on 17 July 2021, and **(c)** broken clouds on 16 June 2021.

nowcasting (MACIN), which uses methods inspired by data assimilation and makes use of cloud images from multiple ASIs. A synthetic setup is introduced to validate MACIN and its components and investigate the error sources. MACIN is applied to real-world data to evaluate nowcast performance. An extension to MACIN is developed and evaluated to include satellite data and to evaluate improvements with these additional data. This extended model for all-sky image based cloud and direct irradiance nowcasting using additional satellite data (MACIN-S) demonstrates the ability of the assimilation-inspired technique to make use of different observations for improved nowcasts. Additionally, a model for irradiance nowcasts based exclusively on satellite images is introduced to schematically demonstrate the use of satellite data for irradiance nowcasting.

This work is structured as follows:

- Section 2 gives the theoretical background on radiative transfer, clouds, and data assimilation and introduces important quantities used throughout this work.
- Section 3 describes the data and methods used for irradiance nowcasting based on all-sky imager and satellite images. This includes methods used to generate synthetic input and reference data for ASI nowcasting. Real-world measurements and ASI images from a PV plant are introduced, as well as satellite measurements. Last but not least, the developed irradiance nowcasting models and their components are described in this section.
- Section 4 is subdivided into four parts. The first part focuses on the validation of MACIN and its components using synthetic data and follows Gregor et al. (2023). Additional synthetic experiments are presented in this part as well to investigate error

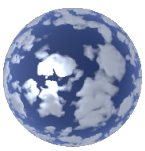

sources even more in detail. The performance of MACIN on real-world data is evaluated in the second part of this section. The third part focuses on the performance of nowcasts based exclusively on satellite images, while the fourth part evaluates the nowcast performance of irradiance nowcasts using both ASI and satellite images.

- Section 5 gives a conclusion of this work, as well as an overview of the remaining challenges and possible future work. Further steps to convert DNI nowcasts from MACIN into actual PV power nowcasts are described as an outlook. The evaluation of these nowcasts demonstrates the potential for energy applications.

Parts of this work were published in Gregor et al. (2023).

As mentioned before, this work was carried out in the framework of the project NETFLEX which investigated the potential of managed biogas plants for stabilizing regional grids with high penetration of PV. The project was centered on a combined biogas and PV power plant in Bavaria. Therefore, this work focuses on single MW scale PV power plants and minute-ahead nowcasts, which can theoretically be used for fine-grained management of biogas plants but also for other applications. The Fachagentur Nachwachsende Rohstoffe funded the NETFLEX project on behalf of the German Federal Ministry of Food and Agriculture.

All-sky images are given on the lower page corners of this work for an illustration of the used data. Odd pages give images captured by the ASI-16126 in Egling a.d. Paar in 2 min steps starting from 11:00:00 UTC on 20 July 2021. Synthetic images for LES clouds are given on even pages, starting at model time 3 h and decreasing in 2min time steps.

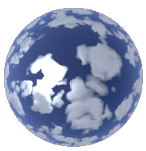

Chapter 2

Theory

2.1 Radiative Transfer

The propagation of electromagnetic waves through the atmosphere determines the radiative energy available on the ground for photovoltaic power plants. The main effects relevant for describing the radiative transfer in the context of this work are interaction with molecules, particles, and other matter by scattering and absorption. This section introduces fundamental quantities associated with radiative transfer and describes the two relevant types of scattering as well as the radiative transfer equation (RTE). It is based on Andrews (2000), Zdunkowski et al. (2014), and Liou (2002) with adapted notation. For a more thorough and complete description of radiative transfer in the atmosphere, the reader is referred to this literature.

2.1.1 Radiative quantities

Fundamental quantities and definitions associated with radiative transfer are introduced in the following. The main effect of radiative transfer is the transport of energy through the atmosphere. The amount of energy is commonly given by one of the following quantities:

- Radiance L: Radiance gives the radiative energy $\mathrm{d}Q$ per area $\mathrm{d}A$ and time $\mathrm{d}t$ from or to a solid angle $\mathrm{d}\Omega$ as

$$L = \frac{\mathrm{d}Q}{\cos\theta \mathrm{d}A \mathrm{d}\Omega \mathrm{d}t} \tag{2.1}$$

  in $\mathrm{Wm}^{-2}\mathrm{sr}^{-1}$. The angle θ gives the zenith angle of $\mathrm{d}\Omega$ with respect to the surface normal and $\cos\theta$ accounts for the orientation of the surface.

- Irradiance E: The radiative energy per time per area gives the irradiance

$$E = \frac{dQ}{dAdt} = \int_{2\pi} L(\Omega)\, \cos\theta\, \mathrm{d}\Omega \tag{2.2}$$

  in Wm^{-2} with the angle between Ω and the surface normal vector θ. It can be derived from the radiance by integration over a half-sphere (2π).

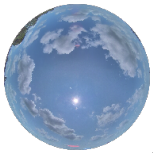

- Actinic flux F: Actinic flux gives all the light available for a place in the atmosphere. For this work, it is defined as the integral of radiance over the full sphere

$$F = \int_{4\pi} L(\Omega)\,\mathrm{d}\Omega \tag{2.3}$$

in Wm^{-2}.

In the atmosphere, electromagnetic waves interact with molecules, particles, and matter in general in two ways: scattering and absorption. These interactions can be described using the following physical quantities:

- σ_{sca}, σ_{abs}: The scattering and absorption cross section give the magnitude of scattering and absorption respectively of electromagnetic waves interacting with a single particle or molecule. The unit is m^2.

- Q_{sca}: The scattering efficiency is the ratio of the scattering cross section and the geometric cross section of the particle or molecule

$$Q_{\mathrm{sca}} = \frac{\sigma_{\mathrm{sca}}}{\pi\, r^2} \tag{2.4}$$

with the particle radius r.

- σ_{ext}: The extinction cross section gives the overall magnitude of interaction of electromagnetic waves with a single particle or molecule $\sigma_{\mathrm{ext}} = \sigma_{\mathrm{sca}} + \sigma_{\mathrm{abs}}$.

- β_{sca}, β_{abs}, β_{ext}: The scattering, absorption and extinction coefficient give the magnitude of interaction of electromagnetic waves with all molecules in a unit volume. For n molecules in the unit volume, the coefficients depend on the respective cross sections by

$$\beta_{\mathrm{sca}|abs|ext} = n \cdot \sigma_{\mathrm{sca}|abs|ext} \tag{2.5}$$

in m^{-1}.

- ω_0: The single scattering albedo gives the ratio of scattered over extincted radiation as

$$\omega_0 = \frac{\beta_{\mathrm{sca}}}{\beta_{\mathrm{ext}}}. \tag{2.6}$$

- τ: The optical thickness is the integral of the extinction coefficient over a path s

$$\tau = \int_s \beta_{\mathrm{ext}}(s')\,\mathrm{d}s'\,. \tag{2.7}$$

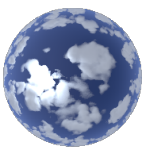

- $\mathcal{P}(\Omega', \Omega)$: The scattering phase function is the probability of scattering light from incident direction Ω' into direction Ω. This function strongly depends on the wavelength of scattered light, as well as the particle or molecule it is scattered by. Sect. 2.1.2 gives more detailed information on phase functions for scattering on molecules and particles.

Radiance and irradiance, as well as the interaction quantities above, are given here as wavelength integrated. They can also be formulated as spectral quantities per wavelength. Mainly the radiative energy integrated over the solar spectrum over all wavelengths up to approximately 3.5 µm is of interest for this work. Spectrally integrated quantities for this solar spectrum will be assumed if not stated otherwise. Note, that the absorption and scattering cross sections and coefficients and therefore also the optical depths can be combined linearly. Therefore, these quantities can be separated to differentiate the effects of clouds, aerosol and molecules, e.g., $\tau = \tau_{\text{cld}} + \tau_{\text{aerosol}} + \tau_{\text{mol}}$.

For solar energy applications within this work, standardized definitions of irradiance are used (ISO/TR 9901, 2021). These distinguish between GHI, DHI and direct normal irradiance DNI. GHI gives downward irradiance on a horizontal plane. DHI gives downward irradiance on a horizontal plane, but only considers light that was scattered at least once. DNI gives irradiance of direct, unscattered sun light for a plane perpendicular to the angle of incidence. Thus, GHI consists of direct and diffuse irradiance as

$$\text{GHI} = \text{DHI} + \text{DNI} \cos\theta \tag{2.8}$$

with sun zenith angle θ.

2.1.2 Mie and Rayleigh scattering

A significant fraction of solar radiation is scattered on its way through the atmosphere. Apart from scattering cross sections mentioned before, the angular distribution of scattered radiation is a key component for understanding and modeling radiative transfer. The Maxwell equations describe the propagation of electromagnetic waves. Mie-Theory is based on the Maxwell equations and describes the scattering of electromagnetic waves on spherical particles. Mie scattering is often assumed for particles in the atmosphere with sizes in the order of the wavelength. The Rayleigh approximation (Rayleigh, 1871) gives a simpler formulation for a special case of the Mie-Theory. It is applicable for molecules and other particles that are small compared to the wavelength of scattered radiation. Within this work, scattering will be separated into Rayleigh scattering for atmospheric molecules and Mie scattering for cloud droplets and aerosols. The two types of scattering differ in characteristics of the scattering phase function. Additionally, the scattering efficiency depends more on wavelength for Rayleigh scattering than for Mie scattering. The latter can be visualized by the fact that the clouds are grayish, while the cloud-free sky is blue. Rayleigh scattering is more efficient for shorter wavelengths, meaning that more blue light

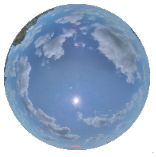

is scattered by molecules than red light, resulting in a blue sky. In contrast, the efficiency of Mie scattering in clouds is relatively independent of wavelength, and clouds appear white or gray. A non-normalized version of the scattering phase functions for examples of Mie and Rayleigh scattering is depicted in Fig. 2.1. The Rayleigh scattering phase function is relatively uniform with a small forward and backward tendency. It can be described by

$$\mathcal{P}_{\mathrm{R}}(\Theta) = \frac{3}{4}\left(1 + \cos^2\Theta\right) \tag{2.9}$$

Mie scattering features a large forward and backward peak as well as an overall complex structure. To simplify Mie scattering for radiative transfer modeling, the Mie phase

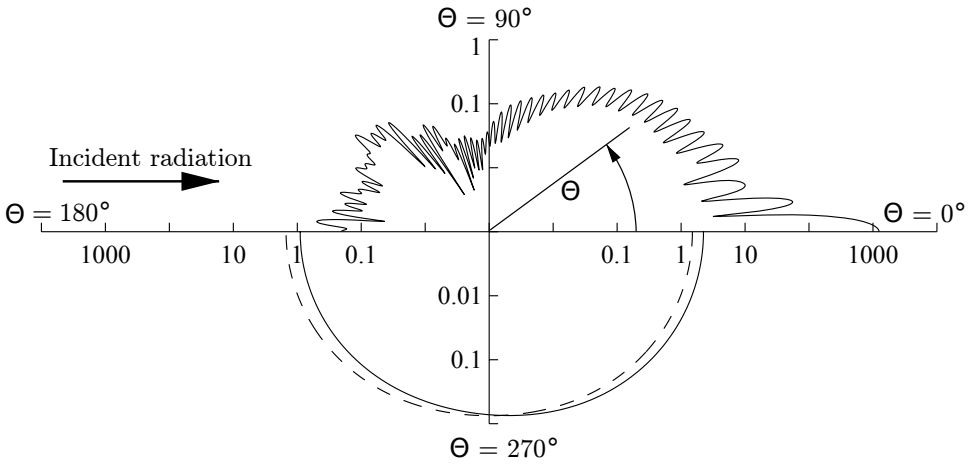

Figure 2.1: Example angle distribution of Mie (upper half) and Rayleigh scattering (lower half, dashed). Θ gives the scattering angle relative to incidence. Note the logarithmic scale on the axes. Taken from Fig. 9.7 in Zdunkowski et al. (2014). *©W. Zdunkowski, T. Trautmann & A. Bott, 2007; Reproduced with permission of The Licensor through PLSclear.*

function is commonly approximated by the Henyey-Greenstein phase function

$$\mathcal{P}_{\mathrm{HG}}(\Theta, g) = \frac{1}{4\pi}\frac{1 - g^2}{(1 + g^2 - 2g\cos\Omega)^{1.5}} \tag{2.10}$$

with asymmetry parameter g. For water clouds, g is typically on the order of 0.85.

A more detailed introduction into atmospheric scattering and Mie-Theory can be found, e.g., in Zdunkowski et al. (2014).

2.1.3 Radiative transfer equation

The radiative transfer equation (RTE) was proposed by Chandrasekhar (1950) and uses the quantities introduced before. It describes the change in radiance over path s in direction Ω based on all the relevant processes:

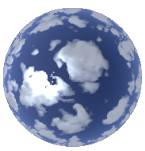

- attenuation due to scattering and absorption

$$-\beta_{\text{ext}} L(\Omega) \tag{2.11}$$

- scattering of radiation from all directions into Ω

$$\frac{\beta_{\text{sca}}}{4\pi} \int_{4\pi} L(\Omega')\, \mathcal{P}(\Omega', \Omega)\, \mathrm{d}\Omega' \tag{2.12}$$

- thermal emission for temperature T according to Planck's law (Planck, 1901)

$$\beta_{\text{abs}} B(T) \tag{2.13}$$

The radiative transfer equation can be written as

$$\frac{\mathrm{d}L(\Omega)}{\mathrm{d}s} = -\beta_{\text{ext}} L(\Omega) + \frac{\beta_{\text{sca}}}{4\pi} \int_{4\pi} L(\Omega')\, \mathcal{P}(\Omega', \Omega)\, \mathrm{d}\Omega' + \beta_{\text{abs}} B(T). \tag{2.14}$$

In the solar spectrum, thermal emission for typical temperatures in the atmosphere of the Earth can be neglected $B(T) \approx 0$.

The Bouguer-Lambert-Beer law describes the reduction of radiance over a path of optical thickness τ

$$L = L_0\, e^{-\tau} \tag{2.15}$$

with the initial radiance L_0 and is a simplification of the RTE in case of no in-scattering and no emission. Due to the oriented nature of direct irradiance on a path towards the Sun, this exponential relation can be used to describe the reduction of DNI as

$$\text{DNI} = \text{DNI}_0\, e^{-\tau}. \tag{2.16}$$

The relative reduction itself describes the transmittance

$$T = e^{-\tau}. \tag{2.17}$$

2.2 Clouds

Clouds are a major modulator of irradiance, especially on short timescales of minutes to hours. Therefore, this work focuses on the nowcasting of irradiance with respect to clouds. Clouds are accumulations of particles of liquid and solid water. They extend over hundreds of meters to kilometers, while being made up of water particles on micrometer scales. A sufficient amount of water droplets, ice crystals and intermediate states is necessary for clouds to significantly impact solar radiation and be visible. However, a strict threshold is hard to define. Clouds are generally advected by wind, but also reshape due to gradients in

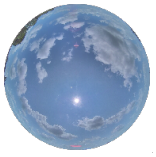

the wind field and turbulence. Growth, e.g., by condensation of additional water vapor, and shrinking, for example, due to evaporation can be observed in nature as well. Important factors for reshaping are the vertical motion of air, wind shear, radiative heating and cooling, and the entrainment of dry and moist air. In short, many processes determine the evolution of clouds over time, which includes changes in position, shape, and optical properties of clouds. A more detailed introduction to clouds can be found in, e.g., Lohmann et al. (2016).

All cloud droplets and ice crystals can interact with solar radiation by scattering and absorption. For modeling radiative transfer in cloudy atmospheres, this interaction is usually not considered particle by particle but summed for all particles in a discrete volume. The relevant properties of the water cloud used for radiative transfer modeling in this work are the liquid water content lwc and the mean effective radius r_{eff}, both for a discrete volume. Here, lwc gives the total amount of water contained, usually in $\mathrm{g\,m^{-3}}$. The effective radius gives a single droplet radius, which is representative of the radiative effect of all the cloud droplets in the volume. As a rule of thumb, water cloud optical depth in a layer of height Δz, can be estimated as

$$\tau_{\text{cld}} \approx \frac{3 \cdot \text{lwc}}{2 \cdot \rho_{\text{w}} \cdot r_{\text{eff}}} \Delta z \tag{2.18}$$

with the density of water ρ_{w}. Large eddy simulation (LES) models are numerical models for modeling the atmosphere on scales of 10s to 100s of meters. They can be used to simulate the evolution of clouds over time. However, modeled scales are still orders of magnitude larger than cloud droplet sizes. Microphysical processes like cloud droplet growth are therefore described by parameterizations. Comparisons of LES models demonstrated the capability of these models to compute realistic clouds situations (e.g.; Neggers et al., 2003; Stevens et al., 2005).

2.3 Data assimilation

Numerical weather prediction (NWP) models are designed to forecast future atmospheric states based on the current state. Therefore, these models need to extrapolate an initial state by modeling the relevant physical processes. A good initial state is a prerequisite for a good forecast. Data assimilation (DA) addresses the problem of finding the initial state based on observations and previous model runs. This section gives a brief introduction to DA based on Pu and Kalnay (2019) and Katsafados et al. (2022) and focuses on the 4D-Var DA method proposed by Le Dimet and Talagrand (1986).

Continuous in situ and remote sensing measurements provide valuable data on the current atmospheric state. These measurement data come with several challenges for the determination of an initial state. Measurements are rarely evenly distributed on the regular grid of a numerical weather model, are subject to uncertainties, and are available at

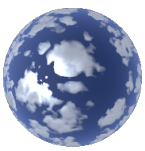

varying times. Additionally, observed quantities may not correspond to model variables directly but require an operator that describes the relation between them and allows for comparison. Missing observations can be compensated for by the use of a background state. A previous predicted model state for the new forecast start time is thereby used as a data source in addition to the new observations. Data assimilation methods are designed to determine an initial model state for the new forecast start time considering these challenges and based on observations and background state.

A four-dimensional variational (4D-Var) data assimilation method was proposed by Le Dimet and Talagrand (1986) to find an analysis state. It relies on a cost function which accounts for differences between initial state and states from previous forecasts, as well as all observations over an assimilation interval. The cost function is minimized to find an analysis state, which is the initial state that best matches previous forecasts and measured data. The 4D-Var cost function can be formulated following Pu and Kalnay (2019) as

$$J\left[\mathbf{x}(t_0)\right] = \frac{1}{2}\left[\mathbf{x}(t_0) - \mathbf{x}^b(t_0)\right]^T \mathbf{B}_0^{-1}\left[\mathbf{x}(t_0) - \mathbf{x}^b(t_0)\right] \tag{2.19}$$

$$+\frac{1}{2}\sum_{i=0}^{N}\left[\mathbf{H}(\mathbf{x}_i) - \mathbf{y}_i^o\right]^T \mathbf{R}_i^{-1}\left[\mathbf{H}(\mathbf{x}_i) - \mathbf{y}_i^o\right] \tag{2.20}$$

with initial state $\mathbf{x}(t_0)$, background state $\mathbf{x}^b(t_0)$ from previous forecasts, background error covariance $\mathbf{B}_0$, observations y_i^o and observation error covariance matrices $\mathbf{R}_i^{-1}$ for N observations. The observation operator $\mathbf{H}$ converts a model state to the observation space to match the location and time of the measurement.

For use in this work, the 4D-Var method is used with several adaptations and simplifications. Due to dense measurements and large forecast errors and therefore background error covariance, no background state is considered. The comparison of observations and model state is done in model space instead of observation space for simplification. Additionally, the error covariance matrix is assumed to be diagonal, i.e., measurement errors are assumed to be uncorrelated in most cases. When the methods in this work are described as assimilation-based or inspired by data assimilation, this is done to reflect the idea of using 4D-Var data assimilation with adaptations and simplifications. For improved readability, the method inspired by assimilation is in some places also directly referred to as "data assimilation". This is done without the intention of overselling the method, but for better readability. As the background state is omitted, the method used in this work is more an initial state estimation by combination of observations than data assimilation.

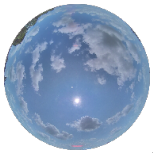

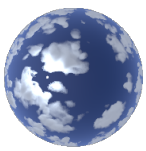

Chapter 3

Methods

3.1 Radiative transfer solvers

The radiative transfer equation (Eq. 2.14) can be solved numerically in multiple ways. The Monte Carlo solver MYSTIC (Mayer, 2009) and the independent column solvers two-stream (Zdunkowski et al., 2014) and DISORT (Stamnes et al., 1988; Buras et al., 2011; Motamedi et al., 1989) are used in this work and will be introduced briefly in Sect. 3.1.1. Additionally, a novel method to efficiently compute radiances and generate synthetic images for modeled cloud situations is explained in Sect. 3.1.2.

3.1.1 Existing radiative transfer solvers

MYSTIC traces single photons physically through 3D cloudy atmospheres. Scattering and absorption of a photon is described by drawing random numbers according to the physically correct distributions. By tracing many photons, a physically correct distribution of photons in the atmosphere can be derived. This represents the distribution of radiation in the atmosphere and can be converted into, e.g., radiances and irradiances.

In contrast to MYSTIC, DISORT (Stamnes et al., 1988; Motamedi et al., 1989) solves the RTE only for a horizontally homogeneous atmosphere instead of full 3D atmospheres. The assumption of horizontally homogeneous atmospheres is commonly applied per column in numerical weather model grids and known as independent column approximation. The atmosphere is effectively reduced to the vertical dimension. DISORT solves the RTE for such 1D atmospheres based on Legendre polynomials, which describe streams in discrete angles defined by the user. The two-stream solver can be seen as a simplification of DISORT where only two streams in upward and downward direction are considered to solve the RTE. The restriction to two streams limits the physical accuracy in favor of computational speed.

The MYSTIC, DISORT and two-stream RTE solvers are embedded in the libRadtran library for radiative transfer (Mayer and Kylling, 2005; Emde et al., 2016), which also provides optical properties for a given atmospheric composition and cloud situation.

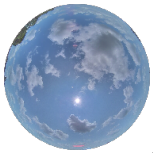

3.1.2 Ray-marching image generation – LASCAT

Gregor et al. (2023) uses a computationally efficient approximation of the RTE to generate artificial images for synthetic cloud scenes. While unnamed in Gregor et al. (2023) and referenced as ray-marching image generation, this approximation will be introduced in the following as last scattering approximation model for 3D radiative transfer (LASCAT). LASCAT computes radiances in the solar spectrum for a given point by solving the RTE for the path between the last scattering and a virtual sensor. The theoretical foundation of LASCAT as well as a description of the implementation are outlined in this section.

Theoretical foundation

For a given atmosphere with optical properties, radiance at a sensor is the integral over a path s from distance 0 to ∞ in direction Ω over all light scattered towards the sensor and attenuated between scattering and additionally a background radiance at top of atmosphere (toa) attenuated by the atmosphere

$$L(\Omega, 0) = L(\Omega, \text{toa}) e^{-\int_0^{\text{toa}} s \cdot \beta_{\text{ext}} \mathrm{d}s} + \int_0^{\text{toa}} \left[e^{-\int_0^{s} s' \cdot \beta_{\text{ext}} \mathrm{d}s'} \beta_{\text{ext}}\, \omega_{0,s} \underbrace{\int_{4\pi} L(\Omega', s)\, \mathcal{P}_s(\Omega', \Omega)\, \mathrm{d}\Omega'}_{= L_{\text{in-scat}}(\Omega, s)} \right] \mathrm{d}s \tag{3.1}$$

where the index s denotes the local value at this position along the path. $L_{\text{in-scat}}(\Omega, s)$ needs to be known to compute the radiance at a sensor. It can be split up

$$L_{\text{in-scat}}(\Omega, s) = L_{\text{in-scat, dir}}(\Omega, s) + L_{\text{in-scat, dif}}(\Omega, s) \tag{3.2}$$

into contributions due to in-scattering of direct light $L_{\text{in-scat, dir}}(\Omega, s)$ and in-scattering of diffuse light $L_{\text{in-scat, dif}}(\Omega, s)$. $L_{\text{in-scat, dir}}(\Omega, s)$ can be computed using the so-called local estimate

$$L_{\text{in-scat}}(\Omega, s) = e^{-\tau_{s,\text{toa}}}\, L_{\text{sun}}(\Omega_{\text{sun}}, \text{toa})\, \mathcal{P}_s(\Omega_{\text{sun}}, \Omega) \tag{3.3}$$

where $L_{\text{sun}}(\Omega_{\text{sun}}, \text{toa})$ is the incoming radiance at toa in direction Ω_{sun} from the position s on the path towards the Sun. This implicitly assumes

$$L_{\text{sun}}(\Omega, \text{toa}) = 0 \quad \text{if} \quad \Omega \neq \Omega_{\text{sun}}. \tag{3.4}$$

The optical thickness between s and toa is given as

$$\tau_{s,\text{toa}} = \int_s^{\text{toa}} s' \cdot \beta_{\text{ext}}\, \mathrm{d}s' \,. \tag{3.5}$$

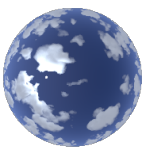

In contrast to direct radiation, the angular dependence and amount of diffuse radiation for all positions are expensive to derive, as a physically correct RTE solver like MYSTIC is required. Computer graphics methods comparable to LASCAT (e.g. Schneider, 2018) roughly approximate the contribution of diffuse radiation. For example, multiple scattering in clouds is not represented correctly there. Although geometrically not correct, independent column solvers such as the two-stream solver can compute irradiances and actinic fluxes while accounting for multiple scattering. LASCAT utilizes pre-computed actinic fluxes to approximate $L_{\text{in-scat, dif}}(\Omega, s)$. The pre-computed actinic flux at s is divided into a direct and a diffuse component $F_{\text{act,dif}}(s)$. Actinic flux does not give any directional information. Therefore, the phase function is assumed to be independent of direction, i.e. isotropic. The in-scattered diffuse radiance is therefore approximated as

$$L_{\text{in-scat, dif}}(\Omega, s) = \frac{F_{\text{act,dif}}(s)}{4\pi}. \tag{3.6}$$

The validity of this assumption is limited for diffuse light, e.g. in optically thin clouds. Light may be scattered twice or three times only with a large fraction of forward scattering because of the anisotropy of Mie scattering. For optically thick clouds and higher orders of scattering, the approximation of isotropy becomes more reasonable.

For consistency, also the in-scattered direct radiance can be calculated from a pre-computed direct actinic flux $F_{\text{act,dir}}(s)$ by assuming

$$L_{\text{sun}}(\Omega_{\text{sun}}, \text{toa}) e^{-\tau_{s,\text{toa}}} \approx F_{\text{act,dir}}(s). \tag{3.7}$$

LASCAT can make use of actinic fluxes pre-computed with any RTE solver as long as the actinic fluxes are provided for the entire 3D atmosphere. Radiances for many directions can be computed in parallel, because of the independence of sampled paths. In this work and Gregor et al. (2023), LASCAT is implemented with actinic fluxes computed by a tilted independent column two-stream solver, and the integration over the path is done in discrete steps by so-called ray-marching. It is used to generate images of modeled cloud scenes and is referenced as ray-marching image generation. The RT method of successive orders of scattering (Deuzé et al., 1989; Lenoble et al., 2007) and LASCAT share the idea of treating light differently depending on how often it was scattered. In contrast to successive orders of scattering, LASCAT only distinguishes between light, which is scattered either not at all, once or multiple times, and treats orders of scattering larger than one equally. Furthermore, successive orders of scattering was developed for horizontally homogeneous and cloud-free atmospheres with aerosol, while LASCAT is targeted at cloudy 3D atmospheres.

Ray-marching implementation

A ray-marching implementation of LASCAT is used in this work and Gregor et al. (2023). It relies on the theoretical foundation outlined above to compute radiances and synthetic ASI images. This algorithm allows for the fast computation of approximated ASI images

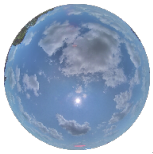

of LES cloud data and is therefore used throughout Gregor et al. (2023) and for synthetic images in this work.

The ray-marching technique is commonly used in computer graphics and the computer game industry (e.g.; Hillaire, 2016; Schneider, 2018) to visualize volumetric data, such as clouds in the atmosphere. Per image pixel, a ray in the viewing direction of the imager is constructed and marched iteratively. For each marching step, the marched mainly two effects are considered. The in-scattering of light into the direction of the imager and the attenuation of light for this step. Effectively, this is a discretized integral of all light that gets scattered into the line of sight of the imager, weighted with the attenuation in the medium.

For use in atmospheric science and this work, a more physically based model is desirable than that used, e.g., for computer games where speed and "epic sky scapes" (Schneider, 2015) are desired. The implementation of LASCAT follows the basic principles of ray-marching. For every image pixel, a ray is stepped in line of sight of a virtual sensor with discrete step size. At every step, in-scattering is computed, and together with transmittance of the path between current position and sensor the contribution to the radiance at the sensor is calculated. The implementation used in Gregor et al. (2023) and this work therefore focuses on the lower atmosphere up to 10 km. The molecular rayleigh optical depth for wavelength λ in the lower atmosphere is parametrized as a simple function of height z (in km) according to Stephens (1994) and Eq. 16 in Bodhaine et al. (1999) as

$$\tau_{\text{Stephens}}(\lambda, z) = 0.0088\lambda^{(-4.15+0.2\lambda)}e^{-0.1188z-0.00116z^2} \tag{3.8}$$

where units are neglected. This can be converted into a rayleigh optical depth of a layer between levels at height z_{i+1} and z_i by

$$\tau_R(\lambda) = \tau_{\text{Stephens}}(\lambda, z_i) - \tau_{\text{Stephens}}(\lambda, z_{i+1}). \tag{3.9}$$

Synthetic cloud data from LES are converted into effective radius and liquid water content according to, e.g. Bugliaro et al. (2011). A 3D field of cloud optical depths τ_{cld} is then computed according to Eq. 2.18. These atmospheric optical properties are used to compute actinic fluxes and the amount of in-scattering.

In order to compute actinic fluxes, independent columns through the atmosphere up to 10 km are constructed for every ground pixel of the LES data. To allow for clouds that, e.g., shade each other, the columns are tilted towards the Sun, as illustrated in Fig. 3.1. The optical properties are sampled from the nearest horizontal grid box for every layer of the tilted column. For each column, direct and diffuse irradiances are computed for all levels using the two-stream radiative transfer solver. The diffuse actinic flux $F_{\text{dif},i}$ for the layer between levels i and $i+1$ at heights z_i is calculated from the diffuse irradiance absorbed in this layer. Therefore, the absorption in this layer is computed as

$$A_i = \frac{1}{z_{i+1} - z_i}\left[(E_{\uparrow,i} - E_{\uparrow,i+1}) + (E_{\downarrow,i+1} - E_{\downarrow,i}) + (E_{\text{dir},i+1} - E_{\text{dir},i})\right] \tag{3.10}$$

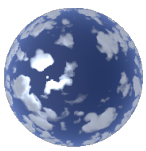

with diffuse upward and downward irradiances $E_{\uparrow,i}$ and $E_{\downarrow,i}$ as well as direct irradiance E_i at level i. The absorbed diffuse irradiance can be computed by subtracting the absorbed direct irradiance by

$$A_{\mathrm{dif},i} = A_i - \frac{1}{z_{i+1} - z_i} E_{\mathrm{dir},i+1} \cdot e^{-\tau \cdot (1-\omega_0)} \tag{3.11}$$

where $\tau = \tau_{\mathrm{cld}} + \tau_{\mathrm{R}}$ is the optical depth of the layer and ω_0 is the single scattering albedo. For $\omega_0 > 0$ the overall diffuse actinic flux can be derived from the absorption as

$$F_{\mathrm{dif},i} = \frac{A_{\mathrm{dif},i}}{\beta_{\mathrm{abs}}} \tag{3.12}$$

with the scattering cross section

$$\beta_{\mathrm{abs}} = (1 - \omega_0) \frac{\tau}{z_{i+1} - z_i} \tag{3.13}$$

The direct actinic flux can be computed using the absorption of the direct irradiance, which is

$$F_{\mathrm{dir},i} = \frac{A_i - A_{\mathrm{dif},i}}{\beta_{\mathrm{abs}}}. \tag{3.14}$$

Pre-computed fields of 3D actinic fluxes are then used for the ray-marching. Radiance L at the sensor of a virtual ASI is summed stepwise in line of sight. The appropriate actinic fluxes and optical depths are retrieved from the input fields. As the ray-marching steps are not equal to the vertical grid spacing, optical depths are rescaled to the step length. For diffuse light, the directional distribution is difficult to assess. Since multiple scattering in clouds is the main consideration for this application, isotropic scattering of diffuse light is assumed. Therefore, the in-scattering probability of diffuse light into line of sight is assumed to be $\frac{1}{4\pi}$. In-scattered diffuse radiance at step j is approximated by

$$L_{\mathrm{dif},j} = \frac{1}{4\pi} \cdot F_{\mathrm{dif},i} \cdot \left[\omega_{0,\mathrm{R}} \cdot (1 - e^{-\tau_{\mathrm{R}}}) + \omega_{0,\mathrm{cld}} \cdot (1 - e^{-\tau_{\mathrm{cld}}}) \right] \tag{3.15}$$

where i corresponds to the grid box index relevant for the jth step. As the direction of direct light is known, the Rayleigh phase function

$$\mathcal{P}_{\mathrm{R}}(\Omega) = \frac{3}{16\pi} (1 + \cos^2 \Omega) \tag{3.16}$$

and the Henyey-Greenstein function as approximation of a phase function for Mie scattering

$$\mathcal{P}_{\mathrm{HG}}(\Omega, g) = \frac{1}{4\pi} \frac{1 - g^2}{(1 + g^2 - 2g \cos \Omega)^{1.5}} \tag{3.17}$$

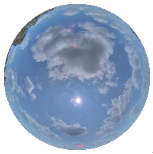

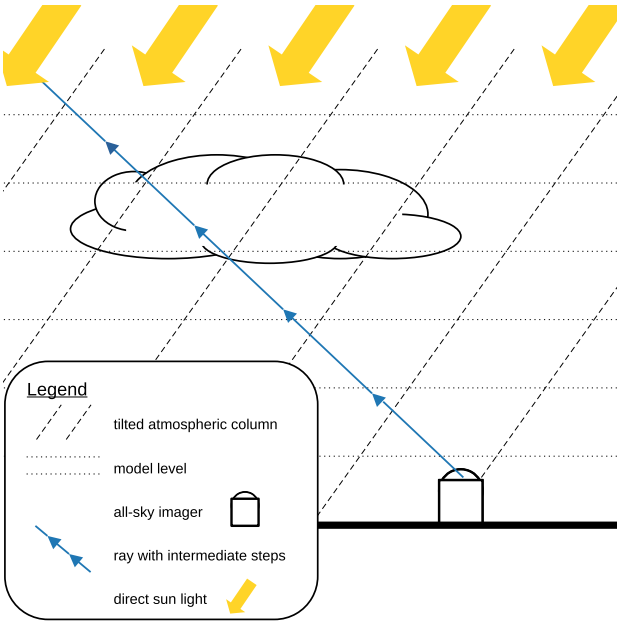

Figure 3.1: Schematic of the ray-marching along an exemplary ray from the imager through the tilted atmospheric columns as used in the implementation of LASCAT.

can be used to calculate the probability of in-scattering with the scattering angle Ω and asymmetry parameter g. Note, that the normalization of $\mathcal{P}_\mathrm{R}$ differs from Eq. 2.9 due to the 3-dimensionality here.

In-scattered direct radiance is computed by

$$L_{\mathrm{dir},j} = F_{\mathrm{dir},i} \cdot \left[\mathcal{P}_\mathrm{R}(\Omega_{\text{sun-ray}}) \cdot \omega_{0,\mathrm{R}} \cdot (1 - e^{-\tau_\mathrm{R}}) \right. \tag{3.18}$$

$$\left. + \mathcal{P}_{HG}(\Omega_{\text{sun-ray}}, g) \cdot \omega_{0,\mathrm{cld}} \cdot (1 - e^{-\tau_\mathrm{cld}}) \right] \tag{3.19}$$

with the angle between the ray which is marched in line of sight and the unit vector towards the Sun $\Omega_{\text{sun-ray}}$. Not all light scattered into line of sight reaches the imager, as it may be scattered or absorbed between the step position and the virtual ASI according to the optical depth along this way τ_j. The radiance for J steps is calculated as

$$L = \sum_{j=1}^{J} (L_{\mathrm{dir},j} + L_{\mathrm{dif},j}) \cdot e^{-\tau_j} + L_\mathrm{bg} \cdot e^{-\tau_J} \tag{3.20}$$

with a background intensity L_bg to add the direct light of the Sun disc and light scattered into line of sight above 10 km. The optical depth above 10 km is computed using the libRadtran software package for the US standard atmosphere and in-scattering for this upper atmosphere is computed once at 10 km. The asymmetry parameter for the scattering in clouds is assumed to be $g = 0.85$ and the single scattering albedo for Rayleigh scattering is set to $\omega_{0,\mathrm{R}} = 0.999999$. To obtain a blue, green, and red channel for each pixel, the computation is done for the wavelengths 450 nm, 550 nm, and 600 nm. The intensities

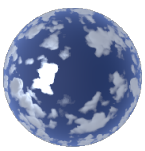

for these wavelengths are scaled according to the solar spectrum of Kurucz (1994). The ray-marching is ended if the distance marched is greater than 100 km, the height of 10 km above ground is exceeded, or the optical depth is accumulated along the line of sight of $\tau_j > 50$. In accordance with the two-stream model, the optical depth, single scattering albedo, and asymmetry parameter for Mie scattering are delta scaled for use here. Finally, post-processing is applied to convert the calculated pixel intensity to pixel values using white balance according to the solar spectrum, a black level, maximum light intensity, and a gamma correction.

The ray-marching implementation of LASCAT can be summarized as follows. First, the direct and diffuse actinic fluxes for all points in the atmosphere are pre-computed. The ray-marching algorithm steps through these pre-computed fields. For every step, local optical properties are considered to compute the fraction of the actinic fluxes which is actually in-scattered towards the imager and therefore contributes to the computed intensity. This is done for three wavelengths that represent the color channels of an RGB camera. Through a post-processing routine in the style of a digital camera, an RGB image is generated.

The computational speed of the method is the result of simple approximations and independent calculations for all pixels. Therefore, it is well portable to GPUs and was implemented for this work using the OpenGL graphics computing framework. Further simplifications, e.g. not splitting the atmosphere between above and below 10 km, as well as adaptations like the full compliance to optical properties used in radiative transfer models, are left for future work. While the pixel intensity determined by ray-marching theoretically could be interpreted as radiance, this is left for further studies evaluating the physical quality of the derived pixel intensities.

3.2 Data

This section describes the data that were later used as input and reference for nowcasting. This work uses synthetic data for modeled cloud scenes, as well as real-world data measured on-site on a PV power plant and by satellites. The synthetic setup with images and DNI computed for modeled cloud scenes is given in Sect. 3.2.1. An on-site measurement setup with two ASIs and irradiance measurements on a PV plant is described in Sect. 3.2.2. Satellite measurements for a region around the PV plant are described in Sect. 3.2.3. This includes satellite images together with further processing to obtain cloud optical depth layers and DNI estimates.

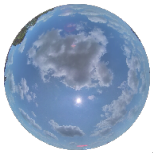

3.2.1 Synthetic data

Synthetic data generation

This subsection corresponds to Sect. 2.1 in Gregor et al. (2023), but omits the marginal description of the ray-marching image generation LASCAT given there. Instead, a more detailed explanation of this technique can be found in this work in Sect. 3.1.2. The ASI geometry referred to in the following is taken from the intrinsic ASI-16142 calibration described in Sect. 3.2.2.

The synthetic data were prepared by Jakub and Gregor (2022). This dataset is a 6 h LES run computed with the University of California Large-Eddy Simulation (UCLALES) model (Stevens et al., 2005). The horizontal resolution is 25 m, and LES output fields are given every 10 s. The initial atmospheric profile was chosen to produce a single shallow convection cloud layer with a cloud-base height of roughly 1000 m developing from a cloud fraction of 0 % in the beginning to roughly 100 % at the end of the simulation after 6 h. The reader is referred to Jakub and Gregor (2022) for more details and impressions of the cloud scenes used in this study.

This dataset provides realistic cloud situations and allows for detailed benchmarking. Cloud liquid water content (lwc) is the most important variable of the dataset for this study. To calculate the optical properties of clouds, the effective radius is also needed. As the LES output field does not contain this information, a fixed cloud droplet number density of $120 \times 10^6\,\mathrm{m}^{-3}$ was assumed. The effective radius of cloud droplets was calculated following Bugliaro et al. (2011). For simplicity, other atmospheric parameters like water vapor, temperature, pressure, and molecular composition from the LES output are neglected within this study, and the US Standard Atmosphere (Anderson et al., 1986) is assumed. While these atmospheric parameters and their variations are generally not negligible for radiative transfer, the setup for this study was simplified to focus on clouds as a major modulator of irradiance. Within this study, the Sun was assumed to be at a constant zenith angle of 30° to the south.

We assume a fish-eye camera model corresponding to the OpenCV fish-eye camera model (Bradski, 2000) for synthetic images generated from these LES cloud fields. The parameters for this projection model were derived from the calibration of a CMS Schreder ASI-16 camera. This ASI features a 180° FOV fish-eye objective to capture hemispheric images of the cloud situation. This study employs two distinct approaches to generating all-sky images from LES cloud scenes. We generate images with the viewing geometry derived according to the fish-eye camera model for the ASI-16 camera. As our methods are developed to work with cameras that are not necessarily calibrated spectrally, the images are only roughly optimized to resemble the colors of the ASI-16. We use a simple spectral camera model with white balance, black level, gamma correction, and an upper intensity limit to convert radiances into pixel values.

One of the image generation methods uses synthetic radiances from the Monte Carlo 3D

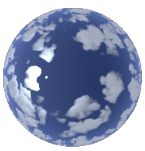

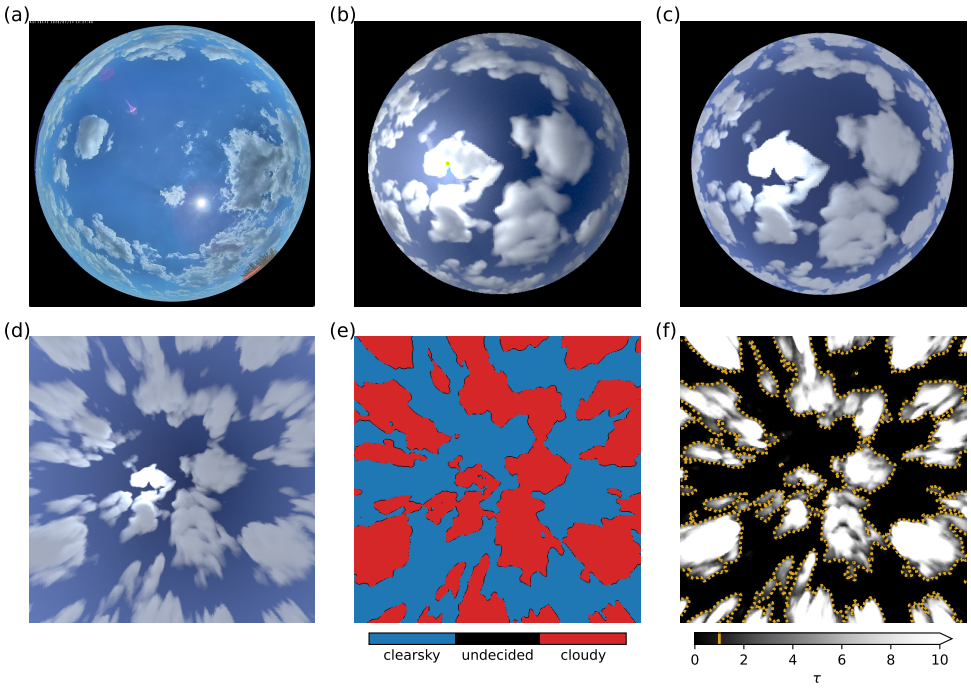

Figure 3.2: **(a)** Real ASI image captured with a CMS Schreder ASI-16 in the Bavarian countryside (48°10′50.3″ N, 11°00′27.4″ E) on 14 July 2020. **(b–d)** Synthetic images for an LES time of 9900 s generated using **(b)** MYSTIC, **(c)** ray-marching, and **(d)** ray-marching followed by projection. **(e)** Cloud mask derived from the projected ray-marching image and **(f)** LES cloud optical depth τ in the line of sight with the additional yellow contours illustrating $\tau_{\text{thresh}} = 1.0$. Only a few pixels are labeled "undecided" by the CNN, as depicted in panel **(e)**. *Colors were adapted from Gregor et al. (2023).*

radiative transfer model MYSTIC (Mayer, 2009), which does not introduce any simplifying assumptions in radiative transfer. These radiances can be converted into synthetic images using the camera model. While MYSTIC radiances are physically correct, they are computationally expensive. Computation of these radiances for a single image requires multiple CPU hours; therefore, this approach was only used for 29 images with a resolution of 240 pixels × 240 pixels. In contrast, our second approach [LASCAT] is only a rough approximation of radiative transfer. This technique is implemented using the OpenGL framework and allows us to generate 960 pixel × 960 pixel images within seconds. Generated images are interpolated to the original ASI resolution in a post-processing step for both generation methods. Figure 3.2a–c show a real-world image as well as images generated using MYSTIC and ray-marching. Because of the low computational cost of image generation, we work with ray-marching images throughout this work if not stated otherwise. We derived cloud masks from both MYSTIC and ray-marching images to confirm the usability of the latter for our purpose.

As a first step in working with generated images, the camera model is applied to project them onto a horizontal, ground-parallel image plane. During re-projection, image features

may be distorted and blurred. However, re-projection allows one to work on an image that is plane parallel to the ground, simplifying further image processing. Figure 3.2c and d display an image as captured by the ASI and its projected correspondence as generated using ray-marching. While the original ASI resolution is 1920 pixels × 1920 pixels, we project images to 480 pixels × 480 pixels for use within our nowcasting model.

Synthetic validation setup

This subsection corresponds to Sect. 2.3 in Gregor et al. (2023). A description of error measures is omitted here and can be found in Sect. 3.7. References were adapted for the integration in this work. This section describes the setup used for the synthetic validation of derived cloud masks, cloud-base heights, and cloud motion as well as nowcasting performance. The setups for the additional experiments for error investigation are included in the description of the experiments and results in the respective parts of Sect. 4.1.2.

The synthetic setup allows us to compare quantities derived by the nowcasting model to synthetic reference values. Within this study, we simulate a setup around a fictional 500 m × 500 m area PV power plant. As depicted in Fig. 3.3, all-sky images are generated for synthetic imagers at positions P1 and P2 centered on the northern and southern boundaries of this area. Direct normal irradiance values were calculated for point P1 and the full 500 m × 500 m area A1 as explained later on. Images are rendered with MYSTIC and ray-marching, as explained in Sect. 3.2.1, for a synthetic ASI at P0 at the southeastern edge of A1 to compare both methods. Ray-marching images for P1 and P2 are used for actual nowcasting and all other applications in this study.

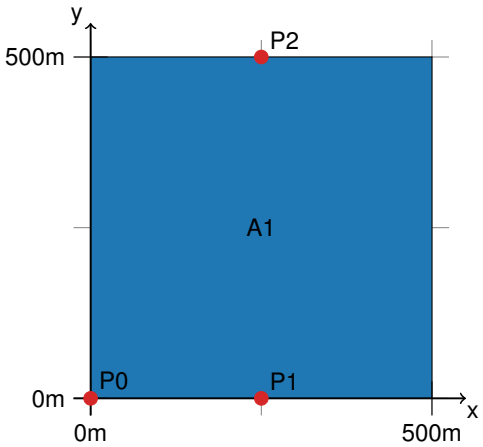

Figure 3.3: Spatial setup for the synthetic experiments conducted in this study. Shown are the ground coordinates within the LES domain. Synthetic all-sky images were generated at points P0, P1, and P2. Direct normal irradiance was simulated for point P1 and area A1. Nowcasts rely on images from P1 and P2 and predict values for point P1 and area A1. *Colors were adapted from Gregor et al. (2023).*

Validation quantities used within the experiments in Sect. 4.1 are explained in the follow-

ing. Cloud optical depth (τ) is traced in the line of sight for every pixel of the corresponding ASI image and used to validate derived cloud masks. By applying a threshold to the resulting τ fields, we can calculate reference cloud masks. Figure 3.2f shows an example τ field. These are used for the validation of the derived CNN cloud masks. The cloud-base height reference is computed in compliance with the view of an ASI. The last scattering of light before reaching the ASI sensor gives the origin of pixel information – in this case, cloud height as seen from below. MYSTIC can be used not only to compute radiances but also to obtain these scattering positions. A cloud motion reference is hard to define, as clouds in the LES simulation – as in nature – are not moving as solid objects but may change size and shape or even appear and disappear. Therefore, wind velocities at cloud level may not be an exact benchmark for the overall observable cloud motion. Within this study, we use the vertically integrated liquid water path (lwp) from the LES fields as an indicator of horizontal cloud distribution. The maximum cross-correlation between the domain-wide lwp of two successive time steps is assumed to be a reference for average cloud motion. This reference describes the mean displacement for all time steps of the LES cloud data. However, clouds are convectively reshaping, growing, and shrinking in these data, which makes this cloud motion definition vague. The synthetic data allow for a more direct validation of cloud motion. LES cloud fields can be frozen for a time step and their position shifted. This basically simulates scenes of pure advection without any convective effects. To simulate this advective case for cloud motion validation, we use two images of the same cloud scene but taken from different positions. The choice of an assumed time difference between the images Δt defines the advective cloud velocity. For simplicity, we use images taken within a 500 m north–south distance, as represented by P1 and P2. Assuming $\Delta t = 60\,\mathrm{s}$, we obtain theoretical cloud velocities of $-8.3\,\mathrm{m\,s^{-1}}$ meridionally and $0\,\mathrm{m\,s^{-1}}$ zonally.

The Monte Carlo 3D radiative transfer solver MYSTIC was used to compute radiances for images and true direct normal irradiances at ground level. We calculated direct normal irradiance for two different synthetic references, as depicted in Fig. 3.3. A DNI point reference is simulated at P1, and an area reference of the 500 m × 500 m region A1 is simulated with ASIs centered at the northern and southern boundaries at P1 and P2. As a benchmark for the DNI nowcasting model, persistence nowcasts for start time t_0 and nowcast time t are calculated from simulated DNI "measurements" at $\mathrm{DNI_{P1}}$ as follows:

$$\mathrm{DNI_{pers}}(t) = \mathrm{DNI_{meas}}(t_0). \tag{3.21}$$

3.2.2 Ground-based observations

Measurement Setup

In this thesis a PV power plant included in the project NETFLEX is used as a case study and practical motivation. The PV power plant is located in the Bavarian countryside near the town of Egling and consists of two PV fields of approximately 250 meter × 250 meter

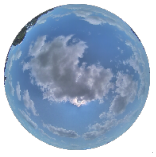

each and about 7 MW installed peak power with a capped grid feed-in of about 5 MW. Fig. 3.4 gives a map of the PV plant. Two measurement sites (station 1/2) were installed and maintained on the concrete containers of the PV plant from 01 October 2019 to 01 August 2022. Power connection was provided within the containers, internet connection was enabled with an LTE-modem per measurement site. The sites are located at coordinates given in Tab. 3.1 with a distance of approximately 531 m between ASIs.

	latitude	longitude	altitude (m A.S.L.)
ASI-16126	48.185338°N	11.0069°E	558
ASI-16142	48.180633°N	11.0076°E	561

Table 3.1: Measurement locations of the two ASIs on-site of the PV-plant. The irradiance measurements were colocated 5 m south of ASI-16142

On both sites CMS Schreder ASI-16 ASIs were installed to capture images of the cloud scene. These cameras feature fish-eye lenses with a FOV of 180°, ventilation and heating as well as a sensor to measure temperature and humidity. Images with 1920 pixel × 1920 pixel were captured automatically in 10 s intervals for times between sunrise and sunset. Throughout this work, the two installed ASIs will be referred to by their serial numbers, ASI-16142 on site 1 and ASI-16126 on site 2.

An Eko STR-22 sun-tracker was installed at site 1 as shown in Fig. 3.5 for the measurement of irradiances additional to the cloud images. It is equipped with two ventilated and heated Eko MS-80 secondary standard pyranometers to measure GHI and DHI. The DHI measurement is colocated with the GHI measurement and only differs as a shadow ball of the sun-tracker masks out direct radiance. Additionally, an Eko MS-57 pyrheliometer for DNI measurements is mounted on a shoulder of the sun-tracker and is tracking the Sun. Measured DNI, DHI and GHI were logged in 2 s-intervals by a Campbell Scientific CR6 datalogger. Example irradiance measurements for three days are given in Fig. 1.1.

Maintenance and cleaning of the ASIs and irradiance measurement devices was scheduled according to measurement problems and depending on the expected contamination of the measurement devices. However, maintenance and cleaning were only possible in limited time intervals due to the rural location and long approach.

Geometric all-sky imager calibration

To map e.g. clouds from ASI images, the geometry represented by the imager needs to be known. More specifically, the viewing direction of every single pixel of ASI images is necessary. This knowledge can be obtained by geometric calibration, which is subdivided into an intrinsic and extrinsic part as described in the following. Intrinsic calibration is done to determine the viewing direction of each pixel relative to each other and the sensor of the ASI. This sensor is not necessarily oriented parallel to the ground while directions

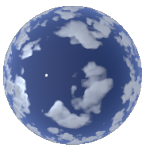

Figure 3.4: Map of the PV power plant reference in this work with locations of ASI-16126 and ASI-16142. Created using Google Earth on 28 June 2023.

Figure 3.5: ASI-16126 (left), ASI-16142 (middle) and STR-22 (right) as installed on the measurement sites.

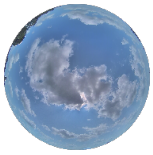

in a real-world coordinate system would be desirable. Therefore, an extrinsic calibration is done to determine the orientation of the camera in space.

Intrinsic calibration aims to derive the viewing direction of each pixel relative to the sensor. This can be described by two parts: The camera matrix and a distortion. As we use the fish-eye camera model implemented in OpenCV (Bradski, 2000), the description here follows largely the description given by the documentation. The camera matrix is used to map from pixel coordinates onto an image plane at a distance $z = 1$ from the sensor. Therefore, it contains information about an offset and scaling of coordinates in both horizontal directions. The offset effectively converts to coordinates relative to a center point at (c_x, c_y), and the scaling is given by the focal length in the respective directions (f_x, f_y) as well as a skewness α. The camera matrix thus connects the pixel coordinates u and v with the coordinates in the image plane x', y' as

$$\begin{pmatrix} u \\ v \\ 1 \end{pmatrix} = \begin{pmatrix} f_x & \alpha & c_x \\ 0 & f_y & c_y \\ 0 & 0 & 1 \end{pmatrix} \begin{pmatrix} x' \\ y' \\ 1 \end{pmatrix} \tag{3.22}$$

However, incoming light on the sensor has to pass through the ASI fish-eye lense first, which changes the direction of the light depending on its angle of incidence. This distortion maps from x and y to distorted coordinates x' and y' and is assumed to be radially symmetric, thus mapping the angle of incidence θ on the lens and the distorted θ'. θ can be calculated using the relation

$$\tan\theta = \sqrt{\frac{x^2}{z^2} + \frac{y^2}{z^2}}. \tag{3.23}$$

The distortion by the fish-eye lense is modeled as

$$\theta' = \theta + \sum_{i=1}^{4} k_i \theta^{2i+1} \tag{3.24}$$

with distortion coefficients k_i. The distorted coordinates are derived as

$$x' = x \frac{\theta'}{\sqrt{x^2 + y^2}}, \tag{3.25}$$

$$y' = y \frac{\theta'}{\sqrt{x^2 + y^2}}. \tag{3.26}$$

Using this model for the camera and distortion, calibration means to find values for the free parameters c_x, c_y, f_x, f_y and k_1, k_2, k_3, k_4 to describe the actual camera. This can be achieved by a set of known x, y and its respective u, v and optimizing the free parameters to match the conversion. As these sets are usually very hard to derive, a workaround is used. For real-world coordinates of points which are on a regular grid are at least their

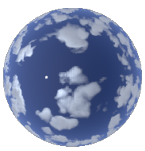

relative positions can be used. E.g. the corners of a checkerboard fulfill this requirement and can be detected automatically in images as shown in Fig. 3.6. The OpenCV library provides functions to optimize the free parameters using a set of images of a checkerboard in various positions and orientations. The respective intrinsic calibration was done with 88 of checkerboards from ASI-16126 and 82 images from ASI-16142. Resulting values for the free parameters are given in Table 3.2. Re-projection error is 0.04 pixel for ASI-16126 and 0.05 pixel for ASI-16142

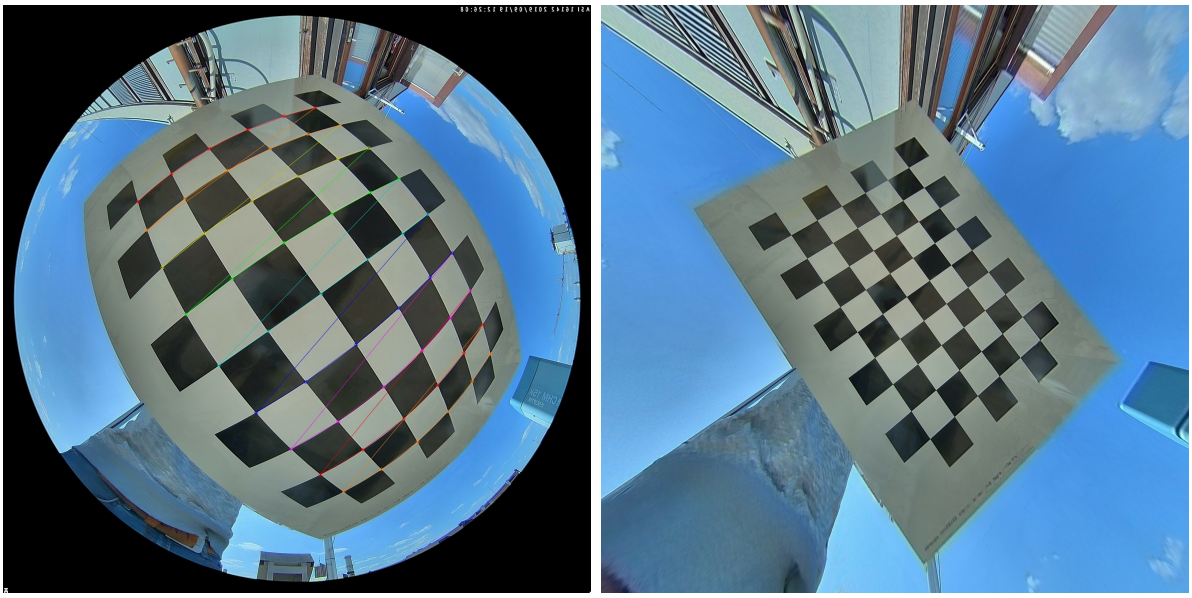

Figure 3.6: Example image of a checkerboard as used for calibration of ASI-16142 with detected checkerboard corners (left). The image after projection according to the derived intrinsic calibration is shown on the right.

Extrinsic calibration derives the viewing directions in a physical 3 dimensional coordinate system. This physical coordinate system was defined for this work with the origin at the position of the imager, the first dimension from west to east **(e)**, the second dimension from south to north (N) and the third dimension upwards from ground to local zenith (U). In this East-North-Up (ENU)-coordinate system planar information at a certain height is parallel to the ground. The intrinsic calibration enables the projection of images onto an image plane normal to the central viewing direction of the ASI. The extrinsic calibration is done to rotate this image plane into a plane parallel to the ground. In order to determine this rotation, the Sun is used. For a given image time, the sun zenith and azimuth angle and thereby a theoretical sun unit vector $\vec{s}_{ENU}$ in ENU-coordinates can be calculated using, e.g., the algorithm suggested in Blanco-Muriel et al. (2001). In case of a non-occluded Sun, it can be detected as the brightest spot in the image. To automatically detect the Sun in an image, the image is first converted into a 8-bit grayscale image and afterwards smoothed with a gaussian kernel with standard deviation of 2 pixels and kernel size 11 pixels. Then an image mask is created from the smoothed image to separate pixel values

Table 3.2: Parameters of the camera matrix and distortion coefficients as derived by intrinsic calibration. The varying number of decimal places corresponds to the actual values used throughout this work.

	ASI-16126	ASI-16142
f_x	623.5807911573587	627.1123486153717
f_y	623.7659532721502	627.0845351791108
c_x	959.3648952511157	952.8484084880499
c_y	960.1688183095001	957.5755356539634
α	0.12873137444614266	−0.4722503587850302
k_1	0.010882902055434084	0.003738368145621751
k_2	0.0007580342753094159	0.008900092963916566
k_3	−0.00552134914672609	−0.012686478988446341
k_4	0.0008343242331998851	0.0037518552472331768

larger than 250. A series of 2 erosions, 4 dilations as well as an opening morphology and a closing morphology with a $5x5$ pixel kernel are performed in order to obtain a continuous and closed estimate of the position of the Sun and ignore e.g. diffraction on the glass dome is partly mitigated A minimum circle enclosing the derived Sun pixels is computed and its center point is used as the Sun pixel in the image. Using the mapping obtained by intrinsic calibration, a viewing direction and unit vector $\vec{s}_{cam}$ in the camera coordinate system can be calculated for the Sun pixel. The extrinsic calibration is used derive the rotation R matrix for

$$\vec{s}_{ENU} = R \cdot \vec{s}_{cam} \tag{3.27}$$

The Sun position was detected in 96 images of ASI-16126 and 84 images of ASI-16142 to obtain the unit vectors. With these sets of vectors, the rotation was iteratively optimized to comply with Eq. 3.27. As the rotation between 360° and 0° poses a singularity for the optimization, the rotation matrix R was not optimized directly. Instead, quaternions were used. They are an extension of complex numbers which can describe 3-dimensional rotations. A good introduction to quaternions for a similar application can be found in the Appendix of Grob et al. (2020). For the optimized quaternion, rotation is finally converted into a rotation matrix R for further use after calibration. This rotation is the desired conversion from the image plane as projected according to the intrinsic calibration into a ground parallel image plane. The rotation matrices for ASI-16126 and ASI-16142 are

$$R_{\text{ASI-16126}} = \begin{pmatrix} 0.04982132 & 0.99845747 & -0.02450561 \\ -0.99874338 & 0.04967217 & -0.00665851 \\ -0.00543099 & 0.02480655 & 0.99967752 \end{pmatrix}, \tag{3.28}$$

and

$$R_{\text{ASI-16142}} = \begin{pmatrix} 0.02920351 & 0.99946398 & 0.01479544 \\ -0.99949952 & 0.02937822 & -0.01173149 \\ -0.01215986 & -0.01444544 & 0.99982172 \end{pmatrix}. \tag{3.29}$$

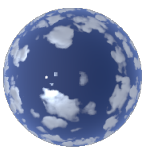

respectively. Figure 3.7 shows a clear-sky situation used for extrinsic calibration with marked center of the intrinsic calibration, derived zenith, as well as detected and theoretical sun position. On average, theoretically calculated and derived Sun position deviate by 0.14° for ASI-16142 and 0.09° for ASI-16126. Errors in the intrinsic calibration as well as the rough estimate of the Sun position in the image contribute to this angular uncertainty.

ASI images can be projected onto a ground parallel plane using the derived extrinsic and intrinsic calibration. Figure 3.2c and d show an image in original geometry and projected respectively. Projected images are used throughout this work if not stated otherwise. The angular uncertainty described above is assumed to be small and neglected.

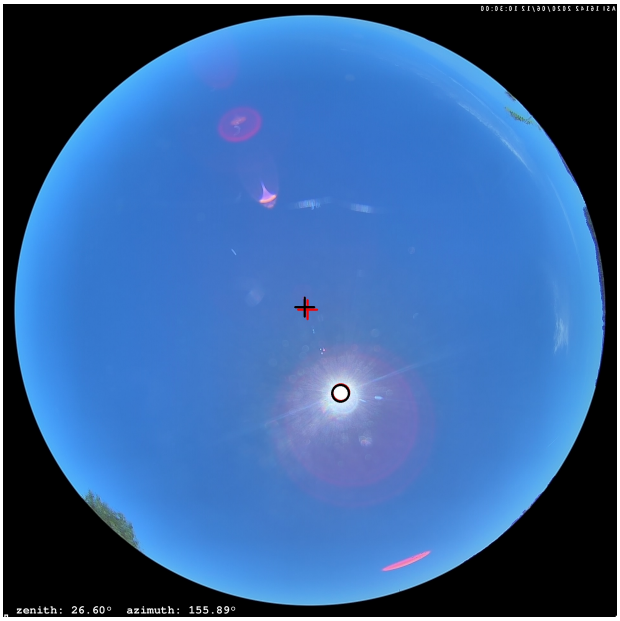

Figure 3.7: ASI-16142 image from 10:30:00 UTC on 12 June 2020 with detected Sun position (red circle), theoretical Sun position (black circle), centerpoint (c_x, c_y) from intrinsic calibration (red cross) and actual zenith (black cross). Note that flipped images are used to convert between ASI view from below and the desired ENU-coordinate system. The redish image regions are due to refraction on the glass dome of the ASI.

3.2.3 Satellite data

Satellite images depict the current cloud situation and offer large spatial coverage. The use of satellite data and its products allows for the exploitation of better information on cloud physical characteristics with respect to radiative transfer. Therefore, they can be used to estimate and nowcast direct irradiance (e.g.; Sirch et al., 2017; Wang et al., 2019). This section gives a brief introduction to satellite images overall followed by a description of further processing to derive optical properties for two cloud layers, correct geometry and estimate irradiance on the ground.

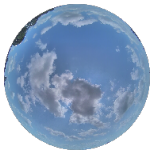

Satellite images

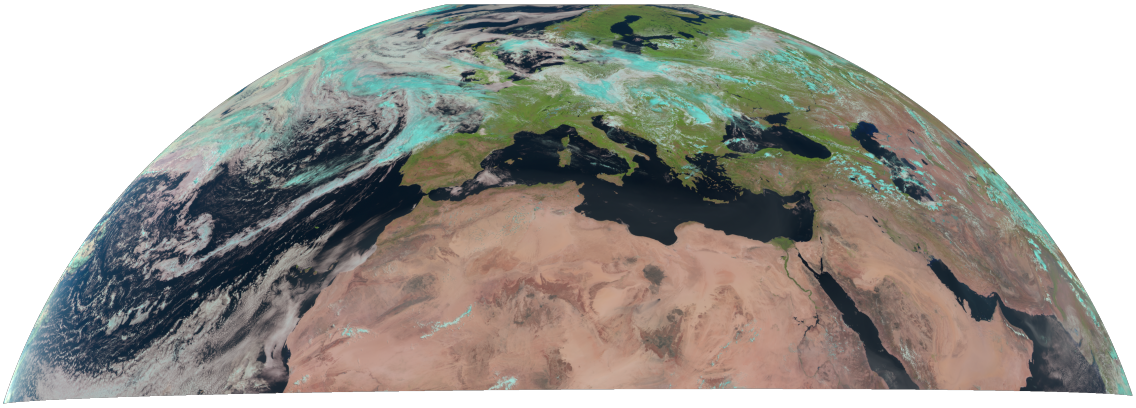

Figure 3.8: Natural color composite of MSG rapid scan 10:00:00 UTC on 02 July 2021.

The Meteosat second generation (MSG) satellites are designed for meteorological observation of atmosphere and earth. These satellites are situated in a geostationary orbit above the equator with varying longitudes and the main instrument is the Spinning Enhanced Visible and InfraRed Imager (SEVIRI). This instrument is capable of measuring spatially resolved reflectances of the full earth disk in 15 min-intervals with 12 spectral channels. 2 channels are in the visible wavelength range, 1 in the near infrared and 8 channels are for infrared wavelengths. An additional high resolution visible channel with improved spatial resolution is available, but will not be used in this work. More details about the spectral channels can be found in Schmetz et al. (2002). The sampling distance of the regular resolution channels is 3 km for the sub-satellite point, which increases for pixels with increasing distance from the sub-satellite point due to the curvature of the earth and viewing geometry. This work uses the Meteosat-10 satellite placed at a longitude of 9.5° E. It provides rapid scans of the northern third of the earth disk in 5 min-intervals instead of the usual 15 min MSG full earth scans. Figure 3.8 gives an example natural color composite image of a MSG rapid scan. This composite is created using the VIS006, VIS008 and IR_016 channel. The application in this work focuses on nowcasts for a specific PV plant in southern Germany. Therefore, a subdomain of approximately 2000 km × 2000 km centered around the PV plant near Egling a.d. Paar was chosen. An example composite image of the subdomain is given in Fig. 3.9a. The subdomain consists of 424 × 455 pixels longitudinally and meridionally respectively and is completely included in the rapid scan domain. Therefore, spectral reflectances from the rapid scan service are used in this work for DNI nowcasting. The spectral reflectance measurements will also be referred to satellite images in the following.

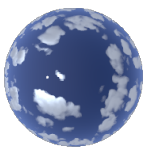

Cloud optical depth retrievals and cloud layers

Spectral images can be exploited to derive cloud information from satellite images. Clouds reflect a large fraction of incoming light in visible channels and absorb in the thermal infrared channels of satellites. This is exploited by the two algorithms APICS and CiPS which were utilized to derive cloud optical thickness from MSG images.

The APICS algorithm is described in Bugliaro et al. (2011). It applies multiple thresholds to MSG images to detect clouds and differentiate between water and ice clouds. Cloud optical thickness is computed from a combination of two channels with different wavelengths following the method of Nakajima and King (1990) and Nakajima and Nakajma (1995). Using further relevant parameters like the sun zenith angle, sensor viewing direction, surface albedo, and a radiative transfer model, cloud optical thickness is derived. In contrast to APICS, the CiPS algorithm (Strandgren et al., 2017) is not targeted at all types of clouds. CiPS is specially designed to derive properties of ice clouds. Based on MSG images and data of an additional satellite, separate artificial neural networks (ANNs) are used to derive a cirrus cloud flag, cloud top height (CTH), ice cloud optical thickness $\tau_{\text{ice,CiPS}}$ and an opacity detection flag.

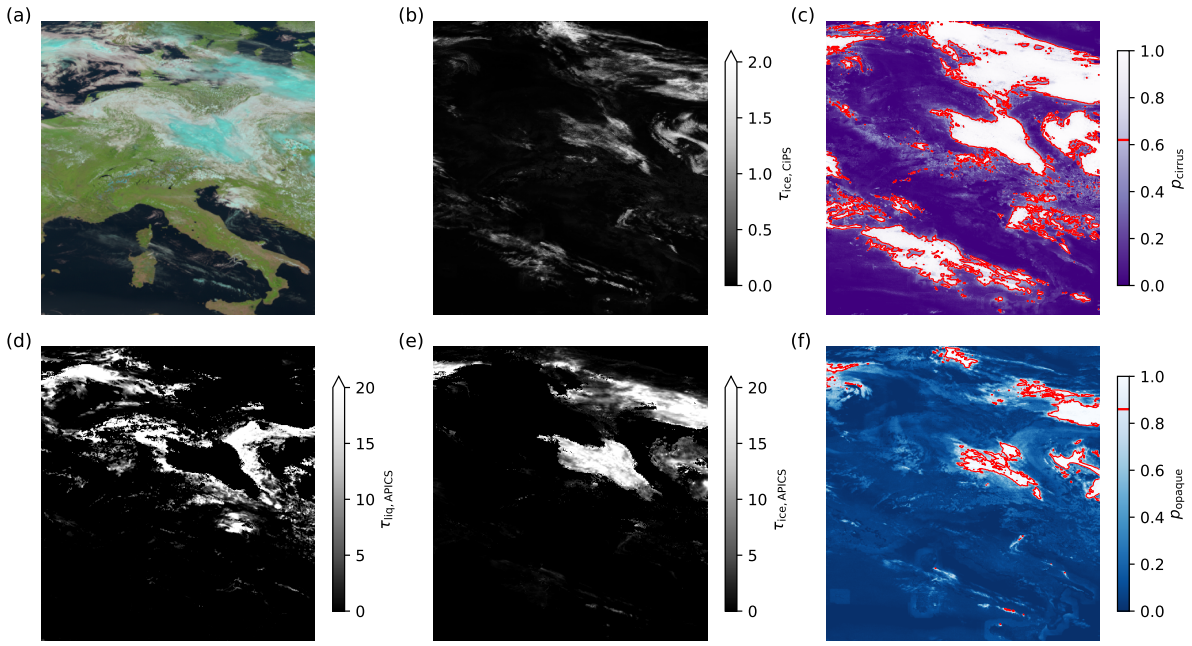

Figure 3.9: Panel **(a)** shows a natural color composite of the domain around Egling a.d. Paar for 10:00:00 UTC 02 July 2021. Derived APICS cloud optical depths for water and ice clouds are given in panel **(d)** and **(e)**, respectively. Derived CiPS cirrus cloud probability p_{cirrus}, opacity probability p_{opaque}, and ice cloud optical depth are given in panels **(b)**, **(c)**, and **(f)**, respectively. The red line in panels **(c)** and **(f)** indicates the thresholds used for inferring binary masks.

The retrieved optical properties from APICS and CiPS are used to construct two layers

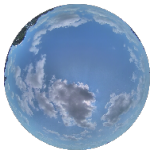

of optical properties, τ_{low} for liquid, mixed phase and optically thick ice clouds and τ_{up} for cirrus clouds. The idea is to use $\tau_{\text{ice,CiPS}}$ for thin cirrus clouds in a upper layer and otherwise use APICS for optically thicker ice clouds as well as mixed-phase and liquid water clouds in a lower layer. Two approaches to construct these layers are used in this work. The first approach follows Sirch (2018) but replaces the COCS (an earlier version of the CiPS approach) by CiPS. It relies on fixed optical depth thresholds for the separation of the layers as

$$\tau_{\text{low}} = \begin{cases} \tau_{\text{liq,APICS}} & \text{if } \tau_{\text{ice,CiPS}} < 0.1 \\ \tau_{\text{ice,APICS}} & \text{if } \tau_{\text{ice,APICS}} > 2.5 \text{ and } (\tau_{\text{ice,APICS}} - \tau_{\text{ice,CiPS}}) > 2.3 \\ 0 & \text{else} \end{cases} \tag{3.30}$$

and

$$\tau_{\text{up}} = \begin{cases} \tau_{\text{ice,CiPS}} & \text{if } \tau_{\text{ice,CiPS}} > 0 \\ 0 & \text{else} \end{cases} \tag{3.31}$$

Due to the increased sensitivity and reliability of CiPS, the thresholds were slightly adapted compared to Sirch (2018). Resulting layer optical depths are referred to as τ_{low} and τ_{up}.

The second approach aims to make full use of the advanced features of CiPS not included in COCS. CiPS provides estimates of a cirrus cloud flag (p_{cirrus}) and an opacity estimate (p_{opaque}) for every pixel additional to $\tau_{\text{ice,CiPS}}$. With the thresholds of 0.62 for p_{cirrus} and 0.86 for p_{opaque}, binary pixel masks can be created (Strandgren et al., 2017). p_{cirrus} provides information on whether a cirrus cloud was detected and p_{opaque} estimates whether the cloud optical depth in a satellite pixel is outside the range of the CiPS training data and, therefore, whether it is unreliable. The two cloud layers can then be constructed as

$$\tau'_{\text{low}} = \begin{cases} \tau_{\text{liq,APICS}} & \text{if } p_{\text{cirrus}} \leq 0.62 \\ \tau_{\text{ice,APICS}} & \text{if } p_{\text{cirrus}} > 0.62 \text{ and } p_{\text{opaque}} > 0.86 \\ 0 & \text{else} \end{cases} \tag{3.32}$$

and

$$\tau'_{\text{up}} = \begin{cases} \tau_{\text{ice,CiPS}} & \text{if } p_{\text{opaque}} \leq 0.86 \\ 0 & \text{else} \end{cases} \tag{3.33}$$

Fig. 3.9 shows cloud optical depths and other quantities as derived by APICS and CiPS for an example scene. The estimated layer cloud optical depths τ_{low}, τ_{up}, τ'_{low}, and τ'_{up} for this scene are given in Fig. 3.10.

The two layers of optical thickness τ_{low} and τ_{up} or τ'_{low} and τ'_{up} respectively are used for advection and irradiance calculations as described in the following. Cloud heights for both layers are estimated using the CiPS cloud top height product. Derived cloud top height

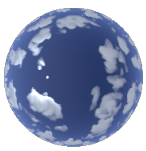

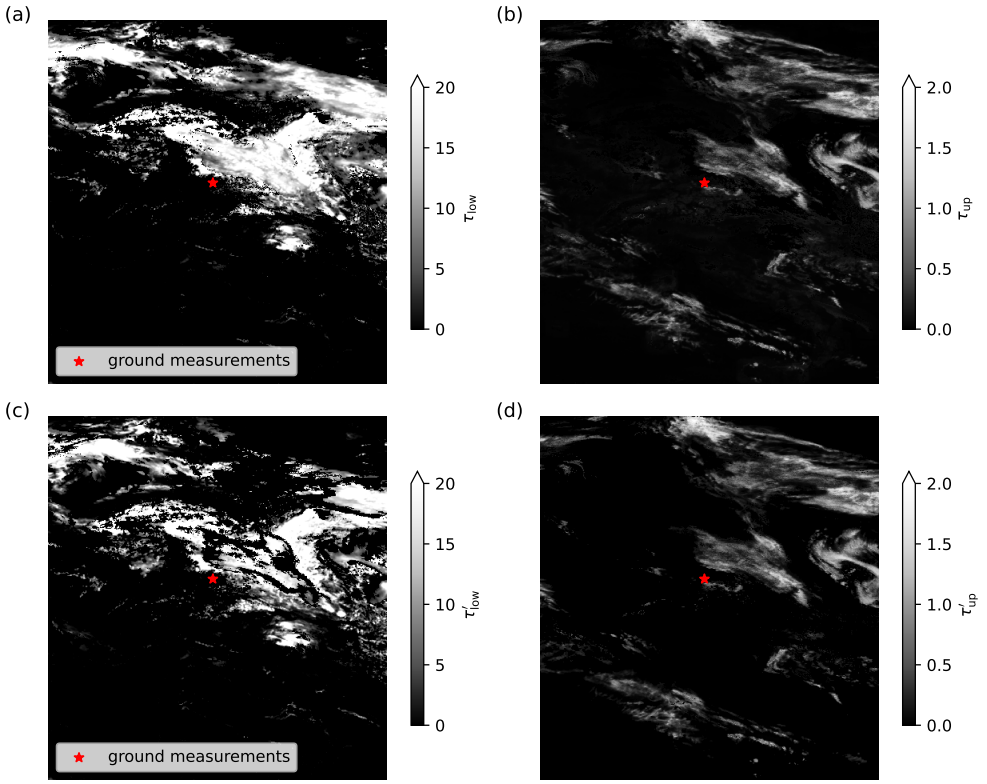

Figure 3.10: Cloud optical depths as derived using the method implemented following Sirch (2018) for **(a)** lower and **(b)** upper cloud layer. **(c)** and **(d)** give the respective layer cloud optical depths when split using the extended CiPS information. Derived for an example scene for 10:00:00 UTC on 02 July 2021. Layers are constructed from CiPS and APICS data depicted in Fig. 3.9

is used as cloud top height for the upper layer where $\tau_{\text{up}} \leq 0.1$ or if $p_{\text{cirrus}} > 0.62$ when using τ'_{low} and τ'_{up}. Otherwise, it is set as the cloud top height for the lower layer. Cloud-base height is set to 2 km below cloud top height. Note that this is an arbitrary choice and should be improved for future applications by using cloud-base heights derived by stereography on ASI images or a ceilometer as, e.g., done in Sirch (2018). The cloud-base height from CiPS is especially targeted at cirrus clouds and therefore may not be reliable for other cloud types. It is nevertheless used here, as other cloud top height products may be inconsistent with CiPS detection of cirrus clouds. In the explanations of the following sections τ_{low} and τ_{up} are used by default for the simple notation. If the difference between τ_{low}, τ_{up} and τ'_{low}, τ'_{up} is relevant, used quantities are named explicitly.

Parallax correction

Cloud top heights provided by CiPS give the height about ground and pixel latitudes and longitudes are provided along the MSG image data. However, the longitude and

latitude information is determined for pixels depicting the Earth's surface. Clouds are usually multiple kilometers above the surface. This leads to apparently shifted clouds as schematically depicted in Fig. 3.11. The shift depends on the viewing geometry, cloud height and earth shape. This effect is known as parallax in satellite applications and needs to be corrected for accurate geometric applications. Vicente et al. (2002) developed a method to determine actual longitude and latitude coordinates for all pixels depending on the cloud height. The suggested method was applied to derive parallax-corrected pixel coordinates for the upper and lower layer advection fields. Values from the resulting irregular grid are interpolated onto the initial regular grid for easier successive use.

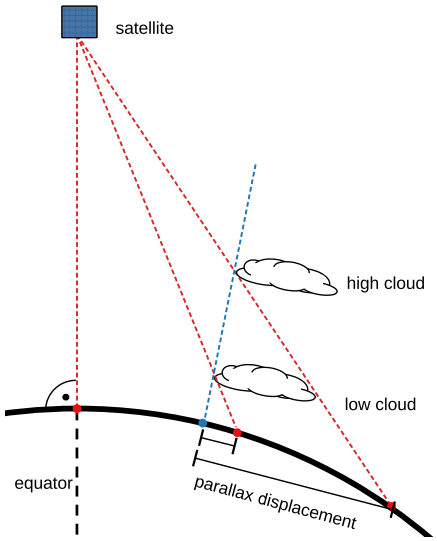

Figure 3.11: Illustration of the parallax displacement in satellite images. Due to viewing geometry and cloud height, cloud positions are mapped to a shifted position on the Earth's surface. Adapted from Sirch (2018).

Pixel coordinates can be converted into metric coordinates according to the geoinformation provided along MSG data. Due to the spherical shape of the Earth, depicted areas vary between pixels, which is still considered in the parallax correction. For simplification, however, it is assumed for all subsequent processing of satellite images that all pixels correspond to equal surface areas. The metric pixel extent is therefore derived from the MSG pixel including the PV plant location in Egling a.d. Paar and assumed to be constant for all pixels of the domain used here. It is 4.74 km in East-West direction and 5.61 km in South-North direction.

Irradiance computation

This section describes the last necessary step for the computation of irradiances from satellite images. Established radiative transfer solvers like two-stream and DISORT can make use of the cloud optical depths of derived and parallax-corrected cloud layers. These solvers compute global, direct, and diffuse irradiance for given atmospheric and cloud

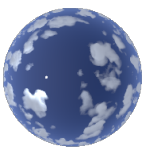

optical properties. Therefore, the main challenge of this last step is the determination of the optical properties relevant for a specific ground position. The US standard atmosphere was chosen as a background atmosphere. The AERONET network (Holben et al., 1998) measures aerosol optical depth. The AERONET level 1.5 is used to scale the aerosol optical depth at 500 nm of libRadtrans default aerosol. The European Centre for Medium-Range Weather Forecasts (ECMWF) reanalysis dataset ERA5 (Hersbach et al., 2023) gives atmospheric states for past times. This ERA5 reanalysis dataset is used to scale water vapor and ozone concentrations to conditions describing the state corresponding to the nowcast time. The relevant cloud optical depths for upper layer ice clouds and lower layer liquid water clouds are geometrically determined from cloud optical depth fields. The parallax corrected fields are used to determine cloud optical depths for the radiative transfer calculations. For a given point on the ground a vector to the Sun is constructed and traced through the atmosphere. More specifically, it is traced through the height mapped cloud optical depth fields towards the Sun as depicted in Fig. 3.12. The cloud optical depths are scaled according to the sun zenith angle and the intersection of traced path and τ_{low} as well as τ_{up}. Cloud optical depths from the upper layer are interpreted as ice cloud optical depth τ_{ic} and from the lower layer as water cloud optical depth τ_{wc}. These are the cloud optical thicknesses used as input to the radiative transfer calculations. As descried above, a US standard atmosphere profile is assumed with scaled aerosol optical depth, water vapor and ozone concentration. Ice and water clouds are added according to τ_{ic} and τ_{wc}. Effective radius is assumed as 20 µm for ice particles and 10 µm for water droplets. The 1D radiative transfer solver DISORT is used to compute irradiances for an independent column with the cloud optical depths as derived for the slanted path to the Sun.

3.3 Clear-sky irradiance and smart persistence

Even though weather is highly variable, the current weather situation is often a good indicator for near future weather. The assumption of constant weather conditions is the simplest possible prediction and called persistence. However, even for constant atmospheric conditions irradiance varies during years and also during days dependent on the position of the Sun. Therefore, a smart persistence is used as a benchmark for irradiance nowcasting systems in literature (e.g.; Inman et al., 2013; Quesada-Ruiz et al., 2014; Logothetis et al., 2022) and also in this study. It assumes constant radiative properties of the atmosphere but considers the effects of changing Sun position. In the following, the method to compute smart persistence for DNI is given. The smart persistence nowcasts for DHI and GHI are retrieved analogously and are therefore not explained additionally.

The current atmospheric conditions can be parametrized as the ratio between currently measured DNI and a theoretical DNI for atmospheric reference conditions. This ratio is

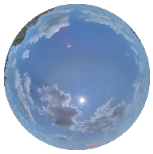

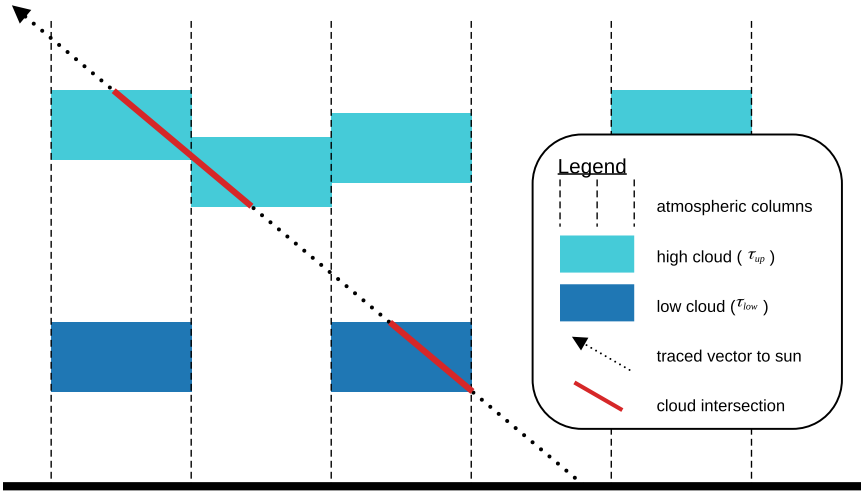

Figure 3.12: Illustration of the determination of relevant cloud optical depths for irradiance at a point below cloud optical depth fields. Atmospheric columns are created for all model pixels with ice and water cloud optical depth placed in heights according to the cloud optical depth fields. A path from the ground towards the Sun is traced and intersections with cloud optical depth layers in the atmospheric columns are calculated. Determined relevant cloud optical depths can be used for irradiance calculations.

the clear-sky index

$$k_{\mathrm{DNI}} = \frac{\mathrm{DNI}_{\mathrm{meas}}}{\mathrm{DNI}_{\mathrm{cs}}} \tag{3.34}$$

computed from measured $\mathrm{DNI}_{\mathrm{meas}}$ and modeled clear-sky $\mathrm{DNI}_{\mathrm{cs}}$ direct normal irradiance. Clear-sky indices $\mathrm{GHI}_{\mathrm{cs}}$ and $\mathrm{DHI}_{\mathrm{cs}}$ can be computed accordingly.

Clear-sky irradiances were computed using libRadtran and its implementation of the DISORT model. Values for GHI, DHI and DNI were computed for all nowcasted days in intervals of 1 min and linearly interpolated for all times in between. Sun zenith angle, sun azimuth and the annually changing distance between Sun and Earth were changed according to the desired time for every radiative transfer computation. The US standard atmosphere (Anderson et al., 1986) was assumed for all times. Atmospheric composition was adapted to comply with the aerosol optical depth as provided by the AERONET level 1.5 product (Holben et al., 1998) from the station Hohenpeißenberg, which is located approximately 42 km from the measurement setup and PV plant in Egling a.d. Paar. Daily aerosol optical depth values were used and interpolated linearly in case of missing data. US standard atmosphere profiles of water vapor and ozone were scaled to match the corresponding vertically integrated columns obtained from the ERA5 reanalysis dataset (Hersbach et al., 2023). Fig. 3.13 gives an example clear-sky day as measured in Egling a.d. Paar as well as corresponding calculated clear-sky irradiances and demonstrates the

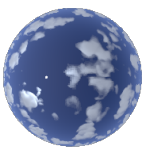

compliance between measured and modeled clear-sky irradiance. Even though the modeled clear-sky irradiances comply well with measurements, some deviations can be found. However, perfect agreement between modeled and measured irradiance is not required due to the consistent use of the clear-sky index in this work, as long as the structure of the diurnal cycle matches.

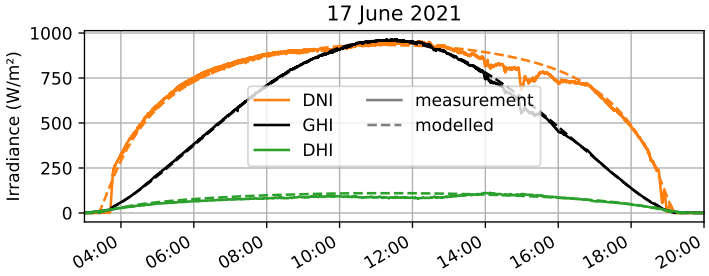

Figure 3.13: Measured irradiances and modeled clear-sky irradiances for the measurement site in Egling a.d. Paar for 17 June 2021.

For the smart persistence, clear-sky index at nowcast start time t_0 is assumed constant and converted into future irradiance for time t by

$$\mathrm{DNI}_{\mathrm{pers}}(t) = k_{\mathrm{DNI}}(t_0) \cdot \mathrm{DNI}_{\mathrm{cs}}(t). \tag{3.35}$$

In case of the synthetic experiments in Sect. 4.1.2 there is no diurnal cycle to be considered. The persistence therefore simplifies to

$$\mathrm{DNI}_{\mathrm{pers}}(t) = \mathrm{DNI}_{\mathrm{meas}}(t_0) \tag{3.36}$$

based on the latest DNI measurement $\mathrm{DNI}_{\mathrm{meas}}(t_0)$.

As stated in Sect. 1 and visible in Fig. 1.1, diffuse irradiance tends to fluctuate less than direct irradiance. In contrast to the relatively simple attenuation of direct irradiance between the Sun and the observer, diffuse irradiance relies on complex 3D scattering. Therefore, smart persistence is used for DHI nowcasting not as a nowcasting method of choice. DHI measurements up to the nowcasting start time are divided by clear-sky DHI to construct a DHI clear-sky index. The exponentially weighted mean with half-width time of 10 min of the latest DHI clear-sky index k_{DHI} is then used to compute the DHI nowcast for time t by

$$\mathrm{DHI}(t) = k_{\mathrm{DHI}} \cdot \mathrm{DHI}_{\mathrm{cs}}(t) \tag{3.37}$$

with the reference clear-sky $\mathrm{DHI}_{\mathrm{cs}}$. Using DHI and DNI nowcasts, GHI nowcasts can be constructed as

$$\mathrm{GHI}(t) = \mathrm{DHI}(t) + \mathrm{DNI}(t) \cdot \cos\theta(t) \tag{3.38}$$

with the sun zenith angle $\theta(t)$ for time t. Note, that the focus of this work is set on DNI nowcasts. DHI and GHI nowcasts are only computed and evaluated in Sect. 5.

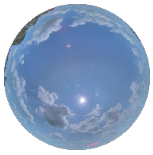

- Should I move the GHI and DHI part to the outlook or keep here?

3.4 All-sky imager based direct irradiance nowcasting model – MACIN

This section introduces the model for all-sky image based cloud and direct irradiance nowcasting MACIN consisting of methods to derive cloud information from images, an advection model, a procedure for determining the initial model state inspired by data assimilation, and a radiative transfer parametrization. *The section is based on Gregor et al. (2023) and gives extensions for the application on real-world data. Sect. 3.4.2 to 3.4.5 as well as Sect. 3.4.6 are taken from Gregor et al. (2023). Section 3.4.1is written based on Sect. 2.1.1 and Appendix A1 of Gregor et al. (2023). Fig. 3.14 was taken directly from this study.*

3.4.1 Cloud mask

As clouds are a major short-term modulator of irradiances, knowledge about their position is crucial for nowcasting. The classification of ASI image pixels as clear or cloudy and therefore the computation of a cloud mask is a first step towards this. The segmentation of images into regions of different classes is a typical computer vision task. CNN are successfully used for such segmentation tasks, also for the specific application of cloud masks (Dev et al., 2019; Hasenbalg et al., 2020; Fabel et al., 2022). For this thesis, a DeepLabV3+ CNN (Chen et al., 2018) with a ResNet-34 (He et al., 2015) pretrained on ImageNet data (Russakovsky et al., 2014) was used. In-depth theory and explanation of CNNs is omitted, as it is used for this thesis as a tool and plenty of detailed and well written descriptions are already existing.

As the distinction between clear and cloudy pixels in images is not always obvious, three cloud mask classes (clear/cloudy/undecided) are introduced. For specific training, 793 images were manually segmented to assign class labels to pixels. To speed up labeling, superpixels (Achanta et al., 2012) were calculated for the images. These are groups of similar-looking neighboring pixels. It allows users to label complete superpixels at once. To support more fine-grained labeling, recomputation of superpixels is supported, e.g., for the remaining unlabeled part of the image or with a higher number of superpixels. Due to the inhomogeneous light situation across the sky and the vague shape and definition of clouds, it is often hard to explicitly assign a superpixel clear or cloudy. The third cloud mask class undecided is offered to label uncertain pixels for which the CNN is not supposed to learn a – possibly erroneous – class. Instead, the CNN is trained to reproduce manually labeled clear and cloudy pixels. By learning the definition of these two classes, the CNN acquires the capability of consistently assigning classes also to pixels, which were manually labeled undecided. The manually labeled images can therefore be seen as sparse

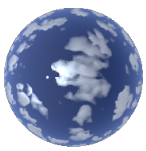

segmentation ground truth. The pixel-wise ground truth was formatted to contain one channel per class, which has a value of 1 for the assigned class and 0 otherwise. The CNN is set up to give predictions in this so-called one-hot encoding format.

For training, the image dataset was split into a training and test dataset with 635 and 158 labeled images respectively. Images were resized to 512 pixel × 512 pixel and used at this size for testing. Training images were randomly cropped to 256 pixel × 256 pixel and mirrored or rotated in steps of 90°. This augmentation artificially increases the size of the training dataset and improves the generalization of the model. The training was done using the Adam optimizer (Kingma and Ba, 2014) with a learning rate of 7×10^{-5} and batches of 26 training images per iteration. A custom sparse soft cross-entropy loss function ($ssce$) was defined to comply with the sparsely labeled data. This $ssce$ ignores pixels that were manually labeled undecided and focuses on the ones distinctively labeled as clear or cloudy. The loss for the ith image pixel is computed from the CNN prediction $y_{\mathrm{pr},i,c}$ and the ground truth $y_{\mathrm{gt},i,c}$ for this pixel and class c by

$$y_{\mathrm{mask},i} = 1 - y_{\mathrm{gt},i,undecided} \tag{3.39}$$

$$LogSoftmax(y_{i,c}) = \log\left(\frac{\exp(y_{i,c})}{\sum_d \exp(y_{i,d})}\right) \tag{3.40}$$

$$ssce_i = \sum_{c\in\{cloudy,clear\}} LogSoftmax(y_{\mathrm{pr},i,c}) \cdot y_{\mathrm{gt},i,c} \cdot y_{\mathrm{mask},i}. \tag{3.41}$$

The ground truth label $y_{\mathrm{gt},i,c}$ is 1 for the class this pixel was manually labeled as and otherwise 0. For the nowcasting application, each pixel i is assigned a class label as $arg\,\underset{c}{max}\,[y_{\mathrm{pr},i,c}]$. The $LogSoftmax$ accounts for this and rescales the CNN predictions into more decisive values, increasing the largest values and decreasing smaller values. While the loss is used to compute the increment during optimization, an additional metric is used to quantify the overall performance of the CNN, especially on the test dataset. A sparse version of mean intersections over union $mIoU$ is used as

$$I = \sum_i \sum_{c\in\{cloudy,clear\}} y_{\mathrm{gt},ic} \cdot y_{\mathrm{pr},i,c} \cdot y_{\mathrm{mask},i} \tag{3.42}$$

$$U = \sum_i \sum_{c\in\{cloudy,clear\}} (y_{\mathrm{gt},i,c} + y_{\mathrm{pr},i,c}) \cdot y_{\mathrm{mask},i} - I \tag{3.43}$$

$$mIoU = \frac{I}{U+\epsilon} \tag{3.44}$$

with $\epsilon = 10^{-7}$ to ensure numerical stability. A final $mIoU = 0.986$ was reached after 48 epochs of training. A hyperparameter search determined the training parameters.

For the usage of the CNN predictions as cloud masks within this thesis, the pixel class is determined by

$$arg\,\underset{c}{max}\,[y_{\mathrm{pr},i,c}]\,. \tag{3.45}$$

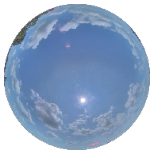

The class is then converted into scalar values with 0.0 for clear, 0.5 for undecided, and 1.0 for cloudy. Fig. 3.14 gives an overview of example images from the test dataset. Additionally, hand-labeled ground truth and segmentation computed by the trained cloud mask CNN used in this work are depicted.

3.4.2 Cloud-base height

In order to map cloud masks to 3D coordinates, cloud-base height (CBH) is required. For the experiments presented here, two ASIs are located within a 500 m north–south distance. Thus, for each time step, two viewing angles can be exploited to derive the CBH. Features from simultaneous ASI images of the same cloud scene are sparsely matched using efficient coarse to fine PatchMatch (CPM; Hu et al., 2016), a pixel-based pyramidal matching method. For a grid of pixels on the first input images, DAISY feature descriptors (Tola et al., 2010) are computed, and their best-matching counterparts in the second image are determined. As a result, we obtain a list of matched pixels from both images, which are supposed to depict the same part of a cloud. We use the derived cloud masks to filter matched pixels; valid matched pixels must be marked as cloudy in the corresponding cloud masks for both images to be accepted. Using the known camera geometry, a cloud-base height can be derived for each matched pair of pixels with the mispointing method developed by Kölling et al. (2019). This results in up to several thousand feature positions per pair of simultaneously captured images, which theoretically allows for a fine-grained treatment of the CBH. However, the nowcasting model presented in this study currently assumes a single cloud layer. Therefore, an image-wide average CBH is derived from the mean height of the feature positions.

3.4.3 Cloud motion

Cloud motion needs to be derived to predict future shading by clouds. Using the CPM matching algorithm on consecutive images taken in intervals of 60 s, we obtain matches describing the displacement of features. Computed cloud masks are used again to exclude matches lying outside of detected cloud areas. Average image cloud-base height and camera model are used to scale detected pixel movement to physical velocities within the assumed plane of clouds. A dense cloud motion field is obtained by nearest-neighbor interpolation of these sparse velocities.

3.4.4 Advection scheme

The nowcasting model is based on a 2D grid with a grid spacing of $\Delta x = \Delta y = 10\,\mathrm{m}$ and a number of grid points $N = M = 1600$ in the x and y directions, respectively, thereby covering 16 km × 16 km. Variables on each grid point are cloudiness state (cm) and cloud

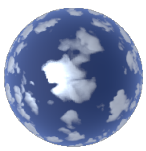

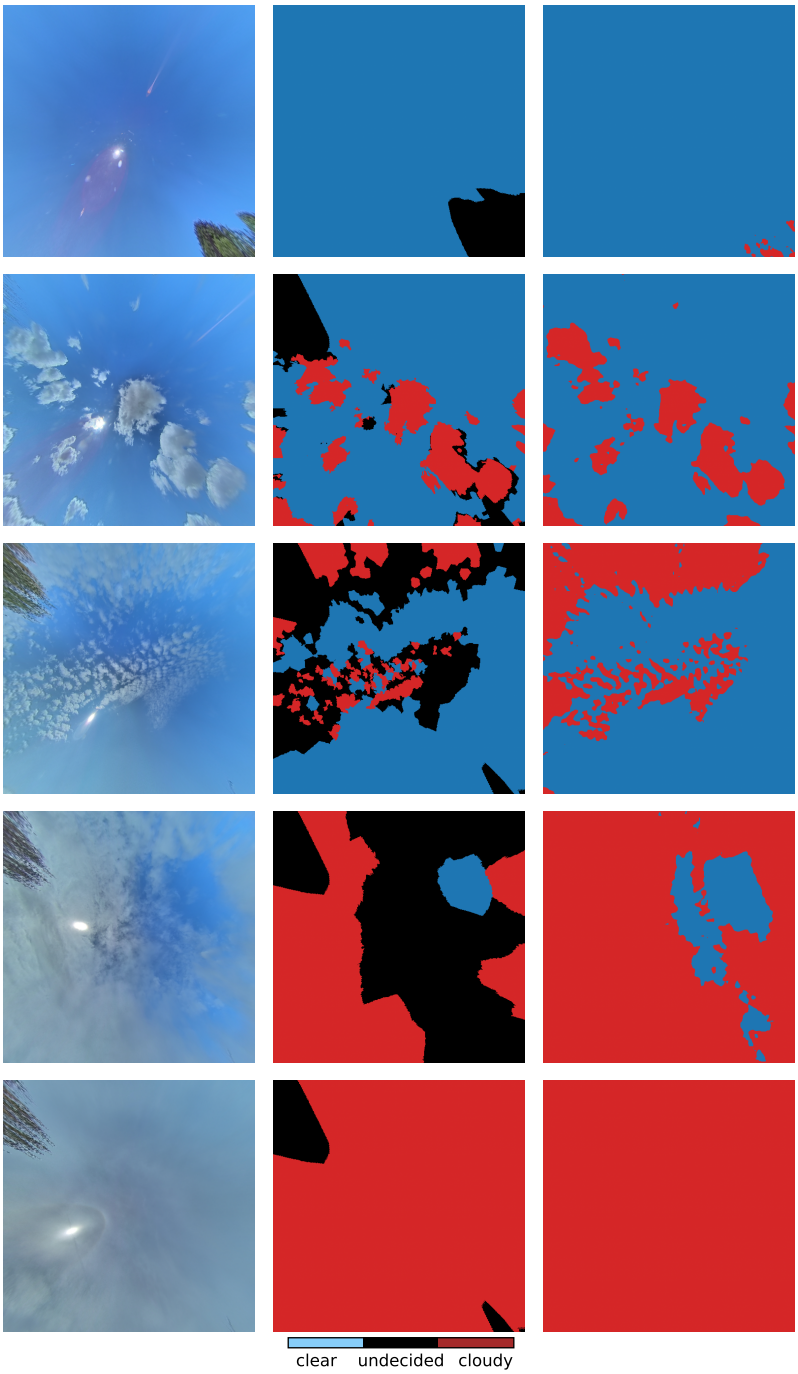

Figure 3.14: Example images from the validation set (left column) hand-labeled segmentation (middle column), and cloud mask predicted by the trained CNN (right column). *Colors were adapted from Gregor et al. (2023).*

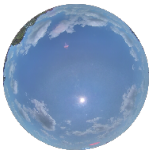

velocities (u and v) in the x and y directions, respectively. Starting from an initial state at the first iteration $t_0 = 0\,\mathrm{s}$ and a temporal resolution of $\Delta t = 60\,\mathrm{s}$, future cloudiness states at times $t_i = t_0 + i \cdot \Delta t$ are computed using advection as follows:

$$\mathrm{cm}_{t_{i+1}}(n, m) = \mathrm{cm}_{t_i}(\tilde{n}, \tilde{m}), \tag{3.46}$$

$$\tilde{n} = n - \mathrm{int}(\lambda \cdot u(n, m)), \tag{3.47}$$

$$\tilde{m} = m - \mathrm{int}(\lambda \cdot v(n, m)), \tag{3.48}$$

where $\lambda = \Delta t / \Delta x$. The coordinates $(\tilde{n}, \tilde{m})$ determined by advection using physical velocities are restricted to discrete grid coordinates and, therefore, integers. This constrains actually representable velocities to multiples of $\Delta x / \Delta t$. Continuous boundary conditions are assumed. The same advection scheme is applied to the horizontal velocities fields $u_t(n, m)$ and $v_t(n, m)$ as well.

Remark: The continuous boundary conditions can be seen as nearest neighbor extrapolation and implemented by

$$\mathrm{cm}_{t_{i+1}}(n, m) = \mathrm{cm}_{t_i}(\tilde{n}', \tilde{m}') \text{ with}$$

with

$$\tilde{n}' = \max(1, \min(\tilde{n}, N)), \; \tilde{n}' = \max(1, \min(\tilde{n}, N)).$$

In case a value outside the model grid would be desired, the value of the nearest boundary grid box within the model grid is used.

3.4.5 Initial state estimation by combination of observations[1]

The cloud mask and horizontal velocity field from one imager and time step as well as an estimation of cloud-base height would be sufficient to initialize the advection model. However, for each nowcast, we do have cloud masks and velocities from two imagers with different viewing geometries and multiple time steps. In order to make use of as much information as possible for the initial state, we employ a method similar to 4D-Var data assimilation [2] (Le Dimet and Talagrand, 1986) in numerical weather prediction models. The general idea is to define a scalar function of an initial model state that measures differences between model states and measurements. This so-called cost function is then iteratively minimized to find an optimal model state for given measurements. We reference "measurements" in this section and the following. We thereby mean the synthetic generated ASI images and simulated DNI values, not real measurements.

The difference between model state and measurements needs to be assessed at matching times. Model states for multiple time steps are therefore computed from the initial state at

[1] This section corresponds to Sect. 2.2.2 in Gregor et al. (2023). Notation was corrected to replace σ by σ^2 for better compliance with the 4D-Var terminology. Erroneous units were corrected.

[2] A comment on the use of the term "data assimilation" can be found in Sect. 2.3.

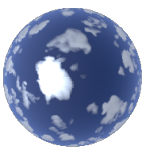

time t_0 using the previously described advection M. Model cloudiness states at time t_k will be denoted as $\mathrm{cm}(t_k) = M(\mathrm{cm}, t_k)$ with initial cloudiness state cm. Horizontal velocities u and v are described analogously. We define the cost function J for L time steps in the interval $[t_0, t_l]$ and two ASIs ($p \in 1, 2$) as follows: [3]

$$\begin{aligned} J(\mathrm{cm}, u, v) = \sum_{N,M} \sum_{l=0}^{L} \sum_{p=1}^{2} \Bigg(& \frac{1}{\sigma_{\mathrm{cm}}^2} \cdot \left(\mathrm{cm}(t_l) - \mathrm{cm}_{\mathrm{meas},l,p}\right)^2 \\ & + \frac{1}{\sigma_{uv}^2} \cdot \left(u(t_l) - u_{\mathrm{meas},l,p}\right)^2 \\ & + \frac{1}{\sigma_{uv}^2} \cdot \left(v(t_l) - v_{\mathrm{meas},l,p}\right)^2 \Bigg) \\ & + R(u, v), \end{aligned} \tag{3.49}$$

with measurements of cloud masks $\mathrm{cm}_{\mathrm{meas},l,p}$ and horizontal velocities at time step l from imager p interpolated to the model grid. Summation over all grid points is indicated by $\sum_{N,M}$ for better readability. The coefficients $\sigma_{\mathrm{cm}}^2 = 0.1$ and $\sigma_{uv}^2 = 10.0\,\mathrm{m^2\,s^{-2}}$ are supposed to account for uncertainties in the respective measurements but are mainly used as tuning parameters here. More complex, non-scalar coefficients could differentiate, for example, between varying measurement quality within ASI images or between different imagers, but they require characterization of the system, which is usually not available. The additional regularization term denoted as $R(u, v)$ is used to suppress measurement errors, especially outliers in the velocity field. In detail, it is

$$R_{uv}(u, v) = \sigma_{R,uv}^2 \cdot \left((\nabla u)^2 + (\nabla v)^2 \right), \tag{3.50}$$

with tuning parameter $\sigma_{R,uv}^2 = 250\,\mathrm{s^{-2}}$ chosen to smooth the velocity field. As cloud masks are especially hard to derive from ASI images in the bright region of the Sun, measurement values are excluded from the assimilation if they are derived from an image region of 2.5° around the Sun. Erroneous cloud mask values derived for the bright Sun and zero velocities derived from the static Sun position are thereby avoided. Figure 3.15 illustrates the measurements, first guess, and analysis state after assimilation for an example assimilation run. Due to the limited complexity of the advection scheme and the high-resolution observations from images, a background state is not used. Model states of previous nowcast runs are not used within assimilation. This means that successive nowcast runs are independent, as states from previous model runs for the nowcast start time are not considered in additional terms in Eq. (3.49). Average cloudiness state and velocities from all measurements available at the time of the initial state are used as a first guess for cost function minimization. The cost function is minimized using the bounded L-BFGS-B algorithm (Zhu et al., 1997). For efficient optimization, the advection model and cost function were implemented using

[3] Note that $\mathrm{cm}(t_l)$ is the variable to be optimized cm extrapolated forward in time with the advection scheme to the time corresponding to the observation $\mathrm{cm}_{\mathrm{meas},l,p}$.

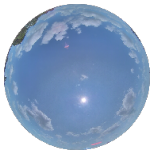

the PyTorch framework (Paszke et al., 2019), which allows for automatic calculation of the adjoint of the cost function. The optimized model state is finally used for the actual nowcast as the initial state of the advection model.

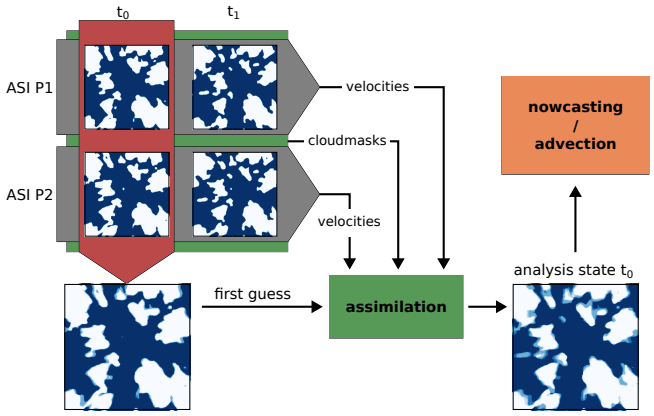

Figure 3.15: Illustration of cloud mask measurements, the derived first guess used for assimilation, and the analysis state found by assimilation for an LES time $t_0 = 8940\,\mathrm{s}$. Shown is the cloudiness state and the inner $8\,\mathrm{km} \times 8\,\mathrm{km}$ of the domain. The analysis state is less sharp on cloud edges due to the consideration of multiple cloud mask measurements. *Colors were adapted from Gregor et al. (2023).*

Enhanced measurement uncertainty estimates

This section describes an extension of MACIN over the version presented above and in Gregor et al. (2023).

The assimilation-inspired method used within MACIN is based on a cost function, which compares the state of the model with measurements and comes with an additional regularization term. Differences between single measurements and the model state are weighted against each other on the basis of the uncertainty of the measurement. This prioritizes less uncertain measurements to be considered during optimization. In full-grown 4D-var data assimilation this weighting is done using an error covariance matrix. In the simplified version of MACIN published in Gregor et al. (2023), scalar weights are used for these measurement uncertainties and as tuning parameters in (cf. Eq. 3.49). A single weight is used for all pixel values of derived cloud masks. This assumption was introduced for simplification. However, the viewing angle differs between pixels in an ASI image. More distant clouds are viewed under a larger zenith angle θ. As explored later on in Sect. 4.1.2, this leads to a misinterpretation of the cloud shape and relevant cloud mask especially for more distant pixels. Blum et al. (2022) investigated the spatial patterns of cloud shadows and fused overlapping cloud information from multiple ASIs. They suggested a cloud mask uncertainty, which varies depending on the viewing geometry for a pixel or grid point. Their formulation is closely followed for this work with adaptations as explained in the following. Changes over Blum et al. (2022) are discussed at the end of this paragraph. The goal is

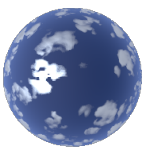

to compute a viewing zenith angle dependent cloud mask uncertainty

$$\sigma^2_{\mathrm{cm,var}}(\theta) = \sqrt{\left(\sigma^2_{\mathrm{cm}}\right)^2 + \mathrm{u}^2_{\theta} + \mathrm{u}^2_{\mathrm{bounds},\theta}} \tag{3.51}$$

for the viewing zenith angle θ of the pixel or grid point. $\sigma^2_{\mathrm{cm}} = 0.1$ is the previously used basic uncertainty associated with classification errors of the cloud mask CNN. The viewing geometry uncertainty

$$\mathrm{u}_{\theta} = A \cdot \tan(\theta) \tag{3.52}$$

gives the errors due to the viewing geometry with $A = 1/3$ according to the estimation of Blum et al. (2022). The vertical extension of the cloud is increasingly misinterpreted as horizontal cloud extension with increasing zenith angle, due to the 2D nature of camera images. For a smooth transition at the boundary of the imaged area and a maximum viewing zenith angle of $\theta_{\mathrm{max}} = 75°$,

$$\mathrm{u}_{\mathrm{bounds},\theta} = \begin{cases} 2/(\theta_{\mathrm{max}} - \theta)\,, & \text{if } \theta < \theta_{\mathrm{max}} \\ \infty, & \text{else} \end{cases} \tag{3.53}$$

is used. The major difference to the uncertainty used in Blum et al. (2022) is the neglection of a term that reflects increased uncertainty in the immediate Sun region. This is omitted here, as the Sun region is completely masked in MACIN also for a constant cloud mask uncertainty. Furthermore, the maximum viewing zenith angle was set to 75 ° in this work to obtain a smaller valid region than with 78 ° in the original publication. For a more thorough explanation of the uncertainties, the reader is referred to Blum et al. (2022). Figure 3.16 shows that the constant cloud mask uncertainty dominates for $\theta < 17°$, while for larger viewing zenith angles u_{θ} is the largest contribution to $\sigma^2_{\mathrm{cm,var}}$ until the maximum zenith angle is approached and u_{bounds} becomes the largest contribution for $\theta > 73°$.

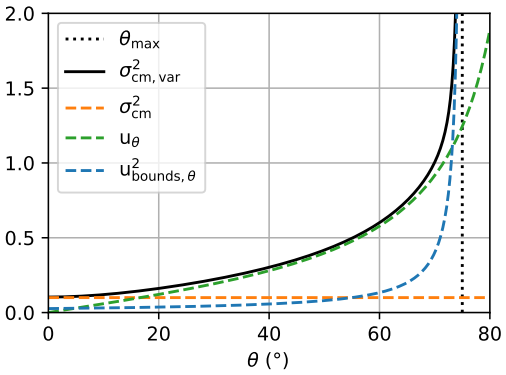

Figure 3.16: Values of the varying cloud mask uncertainty and its components over viewing zenith angle θ.

Note, that the uncertainty of derived velocities was not adapted and is assumed to be constant throughout this work. If not stated otherwise, the constant measurement uncertainties are used throughout this work, especially with the synthetic setups.

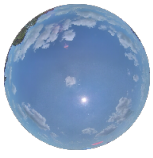

3.4.6 Radiative transfer parametrization

This section describes the radiative transfer parametrization of MACIN for synthetic data and for real-world data. *The description of the synthetic radiative transfer parametrization corresponds to Sect. 2.2.3 in Gregor et al. (2023).*

Synthetic radiative transfer parametrization

Direct solar irradiance is reduced by interaction with molecules, aerosol, and clouds. For this study, we assume that short-term changes in direct irradiance are mainly caused by clouds and neglect other variations. DNI is parameterized using previous irradiance measurements on site as well as predicted cloud masks. "Measurements" in the following do not describe real-world measurements with, for example, a pyranometer, but instead detail DNI values simulated for LES scenes. The idea of the parametrization is to derive references for occluded and non-occluded cases from measurements. Depending on the cloudiness state, the DNI is then interpolated from these references. Therefore, a time series of clear-sky index (CSI) values k is constructed from DNI measurements as the ratio of measurements and a simulated clear-sky $\mathrm{DNI}_{\mathrm{clear}}$. From this time series, values of k are extracted for two sub-series: occluded ($k > 0.9$) and non-occluded ($k < 0.1$) times. We define the occluded CSI k_{occl} and non-occluded CSI k_{clear} as the exponentially weighted mean with a half-life time of 10 min from respective measurement subsets. CSI values for a non-occluded and a fully occluded Sun are interpolated linearly. A Sun disk of 0.5° opening angle at the given Sun elevation and azimuth is projected onto the 2D model grid. The mean cloudiness state of all grid points in the Sun disk ($\mathrm{cm}_{\mathrm{sun}}$) is used to calculate DNI for time t as follows:

$$\mathrm{DNI}(t) = \mathrm{DNI}_{\mathrm{clear}} \cdot ((1 - \mathrm{cm}_{\mathrm{sun}}(t)) \cdot k_{\mathrm{clear}} + \mathrm{cm}_{\mathrm{sun}}(t) \cdot k_{\mathrm{occl}}) \,. \tag{3.54}$$

The exponentially weighted mean is used for the computation of k_{occl} and k_{clear} in order to smooth the latest fluctuations and provide a values for all times.

Measurement-based radiative transfer parametrization

Whilst the cloud mask computation from ASI images does not differ for synthetic and real ASI images, the computation of irradiance in MACIN needs to be adapted for real-world applications. This requires an adaptation of the DNI parametrization presented for synthetic data, as well as a method to additionally parametrize DHI and GHI. For real-world applications, the position of the Sun changes over time and the clear-sky irradiance is therefore a function of time. Atmospheric conditions aside from clouds may vary over time as well and impact irradiance. E.g., vertically integrated water vapor and aerosol optical depth can modulate clear-sky irradiances. Additionally, the synthetic setup is focused on shallow cumulus clouds which are usually optically thick enough to shadow

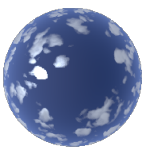

direct irradiance completely. However, many different types of clouds can be observed in real-world applications, which may be optically thinner and shadow direct irradiance partially. Future implications of clouds for direct irradiance should reflect this. As the cloud mask and cloudiness state do not differentiate between types of clouds, this is done by adapting the clear-sky index for occluded and clear sky used in Eq. 3.54. Therefore, a method is required to recognize times, in which DNI measurements can be separated into DNI for clear and occluded sky respectively. This method is explained in the following and visualized in Fig. 3.17. Basically, if there is no cloud in front of the Sun, the measured DNI is used to get an estimate of overall atmospheric conditions apart from clouds. If there is a cloud in front of the Sun, the measured DNI is used to get an estimate of DNI attenuation by clouds. To reflect also the diurnal cycle of DNI, not the DNI measurement but the computed clear-sky index is used. The challenge therefore is to recognize whether or not the DNI measurement is affected by a cloud in front of the Sun. As the DNI measurement and the ASI-16142 were co-located in a distance of about 4 m, the ASI images were used to detect occlusion of the Sun. A CNN was trained to decide whether the Sun is visible or not in ASI images. To simplify occlusion detection, only a cropped 256 pixel × 256 pixel subset of the image centered around the Sun was given to the CNN. Some examples of input images are depicted in Fig. 3.17. Overall, 1000 images were classified manually as *occluded sun*, *non-occluded sun* or *not representative* and split up into a training set of 800 images and a test set of 200 images. A fully connected layer with three outputs for the classes was appended to a ResNet-34 (He et al., 2015) pretrained on ImageNet (Russakovsky et al., 2014). A batch size of 64 images was chosen and the training with the Adam optimizer was separated into two parts. First, only the weights of the fully connected layer were optimized for 40 epochs and with a learning rate of 10^{-3}. After that, all weights of the ResNet and the fully connected layer were optimized for further 60 epochs with a learning rate of initially 10^{-4} which was reduced by a multiplicative factor of 0.9 every 10 epochs. Cross Entropy Loss was used with a relative weight of 10 for the class *not representative* as the number of samples for this class in the dataset is lower than the number of samples for the other classes.

For the RT parametrization in MACIN, the CNN is applied to ASI images taken every minute up to the forecasting time. Minutely averaged DNI measurements are divided by clear-sky DNI reference to obtain a time series of DNI clear-sky index k. All times of k for which the CNN classified the image as *occluded sun* are extracted as a sparse time series. With an exponentially weighted mean with half-life time of 10 min, a current clear-sky index for occluded sun situations k_{occl} is computed. Equally, the CNN classification as *non-occluded sun* is used to construct a current clear-sky index for non-occluded sun situations k_{clear}. These are used to convert predicted cloudiness states into DNI according to Eq. 3.54.

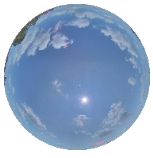

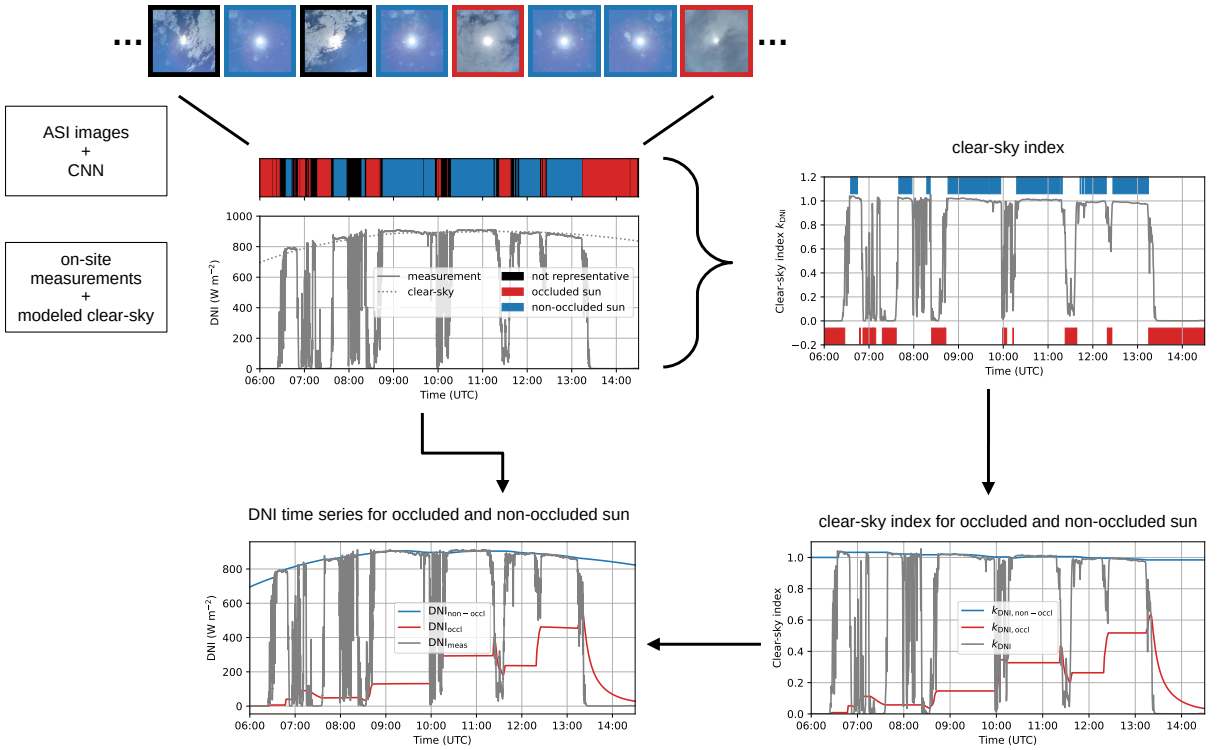

Figure 3.17: Schematic of the computation of time series of k_{occl} and k_{clear} in the radiative transfer parametrization as used for application with real-world ASI images. Illustrated on the example of 29 June 2021.

3.5 Satellite-exclusive irradiance nowcasting model

A model for satellite-based irradiance nowcasting is introduced in the following, which utilizes the method of deriving DNI from MSG images. This model combines cloud motion derived from successive satellite images, an advection scheme and utilizes the methods introduced in Sect. 3.2.3 for DNI nowcasting. An evaluation of performance of satellite-based nowcasts is given in Sect. 4.3. Note that the satellite-based irradiance nowcasting model described here was developed to showcase the use of satellite data for nowcasting and ensure the DNI derived from MSG images can be used beneficially for such applications.

3.5.1 Cloud motion and advection model

In order to nowcast future irradiances, future cloud situations need to be predicted. The cloud situation is described by the derived layers of optical thickness of an upper and lower layer τ_{low} and τ_{up} (cf. Sect. 3.2.3). Prediction is done by advection of these layers. Therefore, cloud motion is derived from the latest set of optical thicknesses at nowcast start time t_0 and the previous time $t_{-1} = t_0 - 15\,\mathrm{min}$. Cloud motion is derived separately

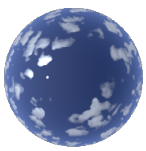

for both layers. Therefore, the fields of optical thicknesses are converted into 8-bit images and optimized for matching. Pixel values for 8-bit images are computed as

$$px(\tau, \tau_{\min}, \tau_{\max}) = \begin{cases} 0 & \text{if } \tau < \tau_{\min} \\ \left(\frac{\tau}{\tau_{\max}}\right)^{0.5} & \text{if } \tau_{\min} \leq \tau \leq \tau_{\max} \\ 1 & \text{else } (\tau_{\max} < \tau) \end{cases} \tag{3.55}$$

with the threshold values $\tau_{\min} = 0$ and $\tau_{\max} = 40$ for the lower layer and $\tau_{\min} = 0.15$ and $\tau_{\max} = 2.3$ for the upper. Analogously to the ASI images in Sect. 3.4.3, two successive images of a layer are matched using CPM (Hu et al., 2016). Matched points are filtered, only points of $\tau > 0.15$ and pixel shifts of less than 50 pixels between images are considered. The shift of the matched points describes the pixel velocity, which can be converted into physical velocites using the knowledge about metric pixel coordinates.

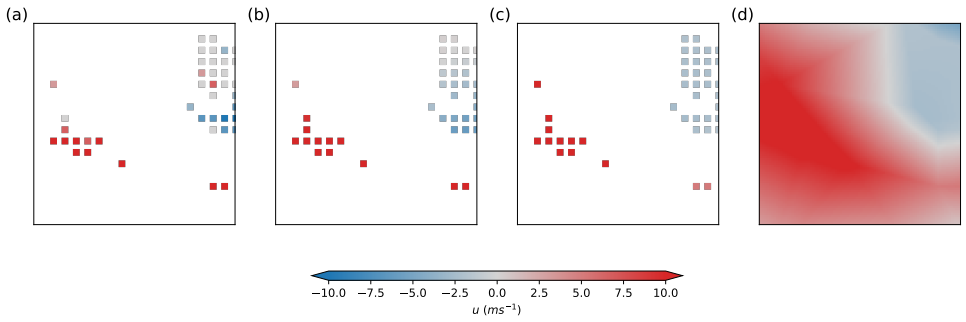

Figure 3.18: Illustration of the construction of dense motion fields from **(a)** initial zonal cloud motion derived by sparse matching of τ_{up} between 09:45:00 UTC and 10:00:00 UTC on 02 July 2021. **(b)** and **(c)** show this sparse cloud motion field after 1 and 5 iterations of smoothing by convolution with a gaussian kernel. **(d)** gives the dense motion field after interpolation. For better visibility, only a cutout of the domain is shown. Note that pixels with velocities in **(a)**, **(b)**, and **(c)** are enlarged for better visibility. The shown region is a 90 pixel × 90 pixel excerpt of the subdomain used in this work. Fig. 3.19 left equals **(d)** but shows the entire subdomain.

A dense velocity field is derived from the sparse velocities in the next step. Figure 3.18 visually accompanies the following explanation by showing intermediate states for a zoomed area of an example case. It starts from the raw sparse velocities after matching in Fig. 3.18a. Cloud areas belonging together are expected to move similarly. Therefore, derived sparse matches are smoothed locally by a 2D-convolution with a gaussian kernel. Standard deviation of the kernel was chosen as 20 pixels. Kernel size was limited to 40 pixels for a restriction to local smoothing and for computational efficiency. This smoothes intra-cloud velocities, while velocities are not smoothed in case of large gaps between clouds. By iteratively applying the convolution 5 times, velocities are smoothed for larger areas within connected cloud areas. Note, that only the sparse velocities are smoothed by these convolutions as shown in Fig. 3.18b-c.

The sparse cloud motion pixels are interpolated to obtain dense cloud motion fields in a last step as depicted in Fig. 3.18d. Interpolation between points with valid velocity is done

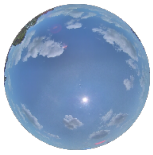

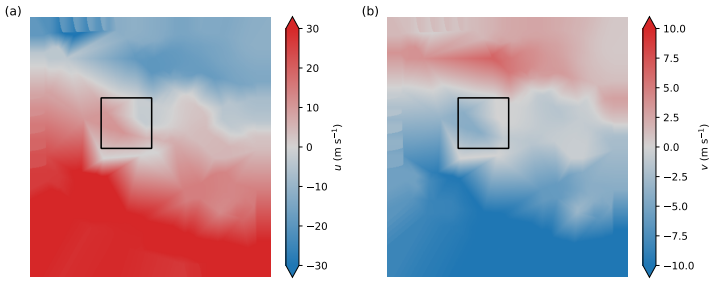

Figure 3.19: **(a)** zonal and **(b)** meridional dense cloud motion fields derived from τ_{up} between 09:45:00 UTC and 10:00:00 UTC on 02 July 2021 for the full subdomain used in this work. The black squares indicate the region used in Fig. 3.18. Note the different color scales.

linearly and values for pixels outside are set to the nearest valid value. This procedure for sparse to dense velocity interpolation with convolutions was developed to overcome shortcomings in the method used by (Sirch, 2018). This previous study derived solid cloud objects and calculated mean velocities for these. As a result, similarities between neighboring clouds were neglected and large continuous cloud fields extending hundreds of kilometers were modeled with a single speed and direction. The convolution approach described above is a simple attempt to overcome these shortcomings.

In an intermediate step, cloud optical depth, cloud-base and cloud-top height are smoothed for both cloud layers. The fields are convolved with a gaussian-kernel with standard deviation of 1 pixel and kernel size of 4 pixels. This is done to suppress possible noise by the retrieval algorithm CiPS, which processes pixels independently from each other. Furthermore, Schmetz et al. (2002) suggests that the satellite measurement takes a larger area in account than the pixel size in the discretized image implies.

Advection of quantities is done as for the ASI images using the same advection scheme as used in the ASI nowcasting model (cf. Sect. 3.4.4). Before the advection, however, all velocity and cloud optical depth fields are linearly interpolated to increase resolution by a factor of eight. This is done to avoid problems due to the restricted discrete advection step sizes. The two layers τ_{low} and τ_{up} are advected separately according to the derived velocity fields. The velocity fields, cloud top and base height are advected as well. Figure 3.20 demonstrates the advection of τ_{low} and τ_{up} fields for an example case and different lead times. An extended evaluation of the quality of the nowcasted optical depth fields was omitted in this work due to its limited extent and the focus on ASI-based nowcasting.

3.5.2 Irradiance calculations

Irradiance can be calculated for advected cloud optical depth layers as described in Sect. 3.2.3. Cloud optical depths for a given nowcast time are sampled along a path from a specific ground position towards the Sun. However, this gives an irradiance estimate for a single moment in time. Due to the resolution of the satellite instrument and the advection time

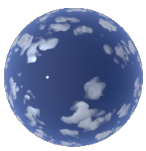

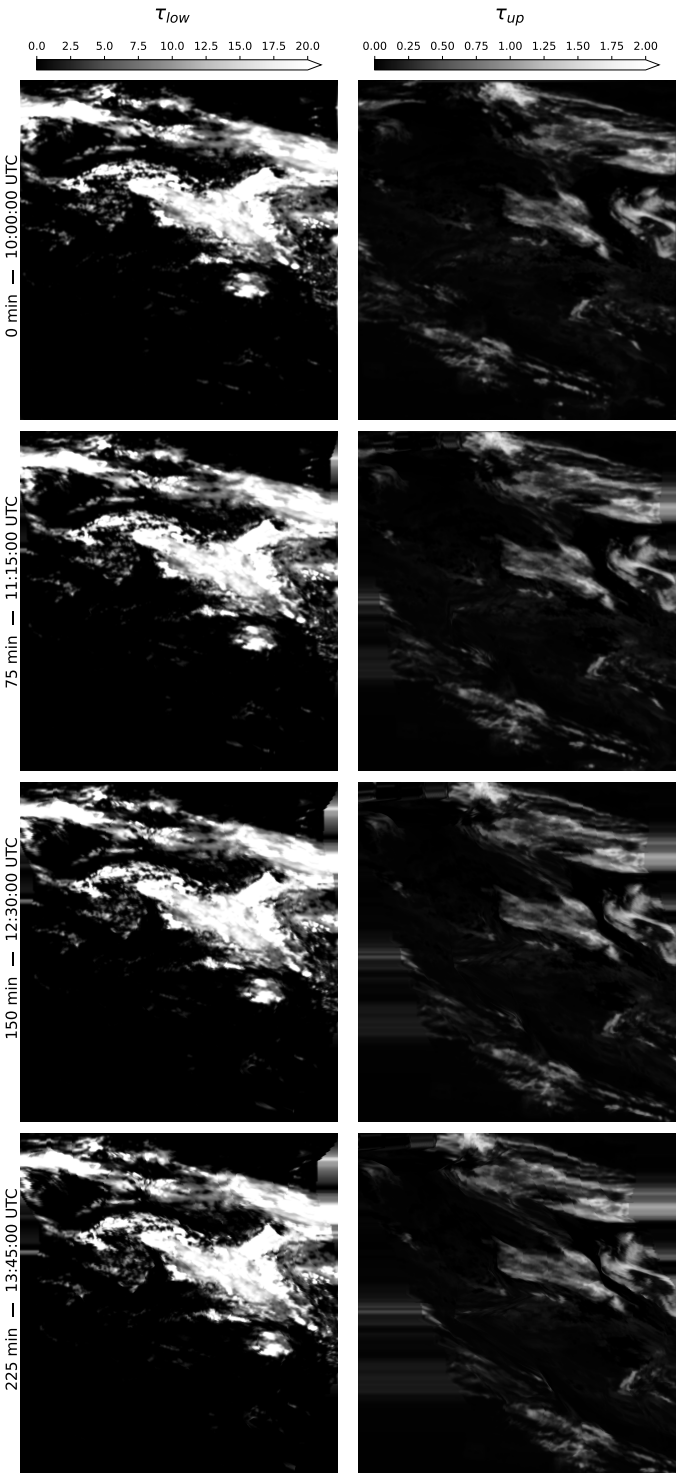

Figure 3.20: Nowcasted cloud optical depth τ_{low} (left) and τ_{up} (right) for nowcast start at 10:00:00 UTC on 02 July 2021 for various lead times.

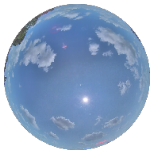

stepping, irradiance nowcasts with time resolution of single minutes or less are not realistic. Exact geometric ray-tracing for an instance in time and cloud boxes with kilometer scale resolution contradict each other. This questions the validity of a single irradiance computation for 15 min averages. To overcome this shortcoming, irradiances for multiple paths representing 1 min values are computed and averaged into a 15 min average. Due to the limited resolution of the nowcasting model, advected fields are only available in 15 min time steps. In order to create 1 min steps of the cloud field, the 15 min cloud optical depth fields are frozen and shifted according the cloud motion of the grid point of the desired location. This cloud motions is assumed constant over 15 min and in the near surrounding. For simplicity, cloud motion of upper and lower layer is averaged into a single representative velocity for both layers. Both layers are shifted accordingly. The shift of cloud optical depth fields can be implemented as shift in the desired ground position in the opposite direction. Figure 3.21 illustrates this procedure of tracing multiple paths. Irradiances are calculated for each of these paths and averaged for 15 min mean irradiances.

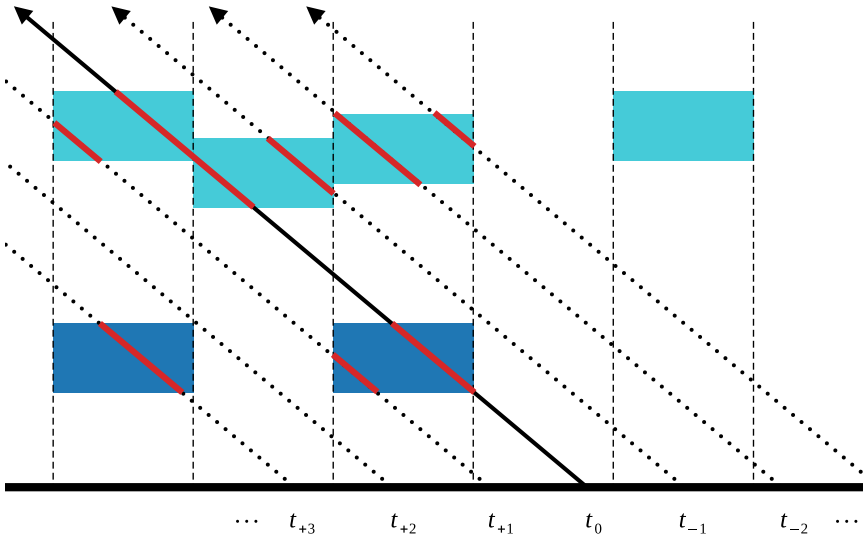

Figure 3.21: Determination of relevant cloud optical depths for a ground position from satellite cloud optical depth fields Equal to Fig. 3.12 but for multiple traced paths constructed for times relative to the 15-minute step t_0. Note that this is just an illustration and not to scale.

3.6 Combined all-sky imager and satellite-based nowcasting model – MACIN-S

The ASI-based irradiance nowcasting model MACIN is developed for minute-ahead nowcasting of spatially and temporally high resolved irradiance. Data from the MSG satellites

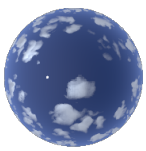

cover the whole globe, and cloud optical depth retrievals can exploit the spectral channels. High resolved ASI images allow for high resolution nowcasts but depict only a limited area of the sky. The use of binary cloud masks makes it harder to compute accurate irradiance values, as ASIs often do not provide a quantitative cloud optical thickness. This section is meant to explore a method to address the shortcomings of the ASI-based nowcasting by additional use of satellite information. This includes two aspects:

- Using satellite derived cloud estimates as boundary condition for the ASI model. Satellite-based values can be used where ASI cloud masks give no information, e.g. in distant regions of the cameras.
- Adapting the irradiance estimation in the ASI-based nowcasting model to consider the satellite-based cloud optical depth retrievals. This can be done by adapting the cloudiness state of the ASI.

In practice, both aspects can be covered at once in the assimilation-inspired implementation of the ASI-based nowcasting model.

MACIN needs to be adapted to make use of satellite data. First, a satellite-based irradiance field is computed for the nowcast start time based on the methods outined in Sect. 3.2.3. As MACIN represents clouds internally by a cloudiness state field, this irradiance field is not directly comparable to the model state. Instead, the irradiance fields are converted into a cloudiness state according to the ASI model RT parameterization. Note that the cloudiness state was originally introduced to represent a mixture of binary cloud masks in MACIN and originally does not contain detailed quantitative information about irradiance itself. Here, the satellite data provides irradiance information and by reversing the RT parametrization, a quantitatively more meaningful cloudiness is computed for satellite information. By an additional term in the cost function, this satellite-based cloudiness field is considered during the optimization of an initial model state. For grid points without valid ASI cloud mask observation, the satellite cloudiness is the only observation and therefore the satellite data is implicitly used to set boundary values. For grid points with valid ASI cloud mask observations, the model state is optimized to comply with observations from both, ASI and satellite. The comparably low spatial resolution of MSG data of more than 4 km in the region of the PV power plant is thereby the main challenge for its use in the cost function with a model grid with 10 m resolution. The cloud optical depth towards the Sun can in theory be computed for every grid point of the ASI nowcasting model. However, the satellite retrieved cloud optical depth fields are constant per satellite pixel and therefore over multiple kilometers. The resolution of clouds in MSG data is much lower than the resolution of the ASI model grid. Deriving cloud optical depth estimates for a high resolution grid from the low resolution satellite data is misleading as it artificially increases resolution. It is therefore assumed, that derived high resolution satellite information has a correlation length of about the size of MSG pixels. To account for this correlation length, averages of satellite derived information are compared with averages of the model state after bringing both quantities onto the same grid.

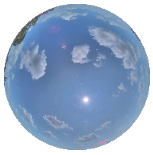

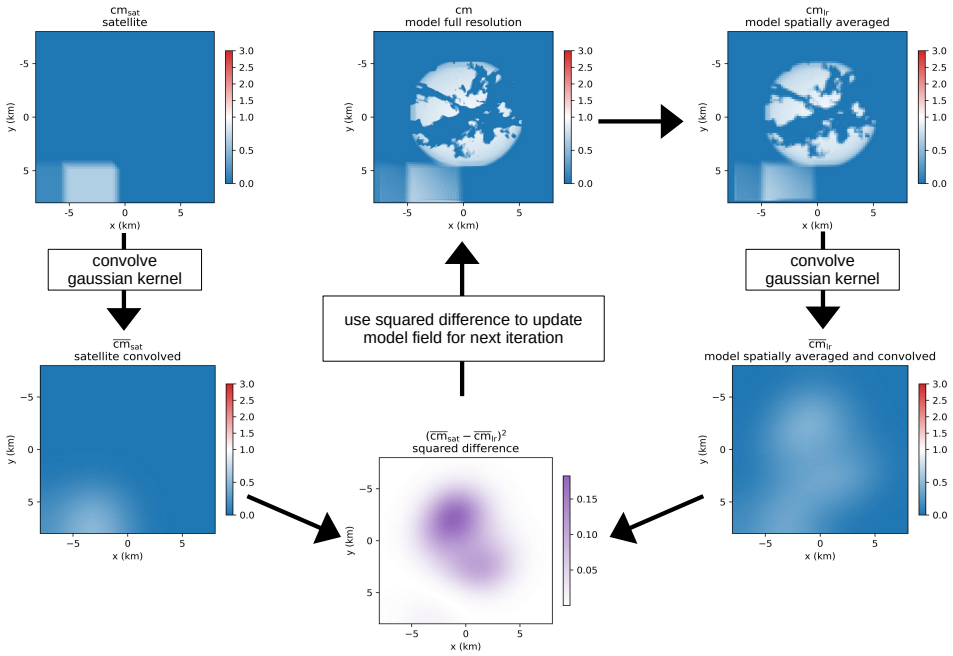

Figure 3.22: Illustration of the procedure used to compute the deviation between satellite cloudiness observations and model cloudiness state for a cumulus cloud scene at 10:00:00 UTC on 02 July 2021. Shown model states correspond to the values after two iterations of optimization. The model state (center, top) is averaged into lower resolution. Low resolution model state and satellite observations are convolved with a gaussian kernel before the difference between these two fields is computed. The squared difference is used in the cost function to compute the next step of the iterative optimization.

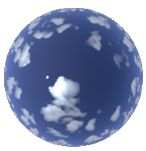

Figure 3.22 and 3.22 illustrate model fields for intermediate steps of the following explanation. Within this explanation, single values within fields of a 2D variable are indicated by an index In case of no index, the entire 2D field is meant. For every desired satellite data grid point the cloud optical depths are determined as explained in Sect. 3.2.3. For computational efficiency, the satellite irradiances are computed on a grid with lower resolution of 200 m and not for the model grid with a resolution of 10 m As for the ASI derived quantities, it is desired to compare also satellite measurements with the nowcasting model state in the model space. The satellite derived cloud optical depths are therefore converted into cloudiness values. This can be done by calculating a satellite derived clear sky index

$$k_{\mathrm{sat}} = \frac{\mathrm{DNI}_{\mathrm{sat}}}{\mathrm{DNI}_{\mathrm{cs}}} = e^{-(\tau_{\mathrm{low}}+\tau_{\mathrm{up}})}. \tag{3.56}$$

Solving the radiative transfer parametrization of Eq. 3.54 for cm, a satellite cloudiness value can be derived as

$$\mathrm{cm}_{\mathrm{sat}} = \frac{1-k_{\mathrm{sat}}}{1-\frac{k_{\mathrm{occl}}}{k_{\mathrm{clear}}}} \tag{3.57}$$

based on the current MACIN clear-sky index estimations in case of occluded sky k_{occl} and clear sky k_{clear} (cf. Sect. 3.4.6). Fig. 3.22 illustrates satellite cloudiness and schematically displays the following steps for two example times.

The model cloudiness field is blockwise averaged to the lower resolution (N', M') of the derived satellite cloudiness state over $P \times Q$ pixels

$$\mathrm{cm}_{\mathrm{lr},n',m'} = \frac{1}{P \cdot Q} \sum_{i=(n'-0.5)P}^{(n'+0.5)P} \sum_{j=(m'-0.5)Q}^{(m'+0.5)Q} \mathrm{cm}_{i,j}. \tag{3.58}$$

For pixels outside the nowcasting model domain, e.g. $i < 0$, nearest neighbor interpolation is applied. Satellite derived and low resolution model cloudiness state can theoretically be compared directly based on this. However, the size of satellite pixels is still larger than the low resolution grid size and spatial correlations of the satellite information would therefore not be represented realistically.

A convolution with a gaussian kernel g with half-width of $\sigma_c = 4\,\mathrm{km}$ is used to represent the correlation length based on the original satellite data resolution. The kernel is defined for the discrete low resolution coordinates as

$$g(i,j) = \begin{cases} \omega^{-1} e^{-\frac{i^2+j^2}{2s_c^2}} & \text{if } |i| \leq s_c \text{ and } |j| \leq s_c \\ 0 & \text{else} \end{cases} \tag{3.59}$$

with correlation length in grid coordinates $s_c = \sigma_c/\Delta x'$ for grid resolution of $\Delta x' = \Delta y'$. The limitation of the kernel size to twice the correlation length is implemented for computational efficiency. ω is chosen for normalization to 1, i.e.

$$\omega = \sum_{i=-s_c}^{s_c} \sum_{j=-s_c}^{s_c} e^{-\frac{i^2+j^2}{2s_c^2}} \tag{3.60}$$

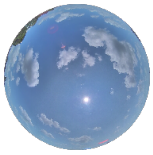

with the correlation length in pixel coordinates .

By convolution with this kernel on the discrete model grid, smoothed fields of the model cloudiness cm and satellite cloudiness $\mathrm{cm}_{\mathrm{sat}}$ are retrieved as

$$\overline{\mathrm{cm}}_{\mathrm{lr},n',m'} = G\left(\mathrm{cm}_{\mathrm{lr}}, n', m'\right) \tag{3.61}$$

and

$$\overline{\mathrm{cm}}_{\mathrm{sat},n',m'} = G\left(\mathrm{cm}_{\mathrm{sat}}, n', m'\right) \tag{3.62}$$

where

$$G(a, n', m') = \sum_{i=-s_c}^{s_c} \sum_{j=-s_c}^{s_c} a_{n'+i,m'+j} \cdot g(i,j) \tag{3.63}$$

is the convolution formulated as a sum over the discrete coordinates.

The summed squared difference of these two fields is used as the deviation between model state and satellite measurements

$$J_{\mathrm{sat}}(\mathrm{cm}) = \frac{1}{{\sigma_{\mathrm{sat}}}^2} \sum_{n'=1}^{N'} \sum_{m'=1}^{M'} \left[\left(\overline{\mathrm{cm}}_{\mathrm{lr},n',m'} - \overline{\mathrm{cm}}_{\mathrm{sat},n',m'}\right)^2 \cdot \gamma_{\mathrm{bounds},n',m'} \right] \tag{3.64}$$

with the satellite measurement uncertainty $\sigma_{\mathrm{sat}}^2 = 0.3$ and the value validity parameter $\gamma_{\mathrm{bounds},n',m'}$. Equally to the uncertainties in Eq. 3.49, σ_{sat} is roughly estimated and in detail chosen as a tuning parameter. The value validity parameter is introduced to ignore the advected boundary values in Eq. 3.64. To determine whether a value is advected from boundary values, the nowcasting model was extended by a model variable b that is additional to cm, u, and v, which is also advected. It is initialized as

$$b_{n,m}(t_0) = \begin{cases} 0 & \text{if } \; n \in \{0, N\} \;\; \text{or} \;\; n \in \{0, M\} \\ 1 & \text{else.} \end{cases} \tag{3.65}$$

Blockwise averages $b_{\mathrm{lr},n',m'}$ are computed parallel to Eq. 3.58 from $b_{n,m}$ advected to the time of the satellite observation. These are converted into

$$\gamma_{\mathrm{bounds},n',m'} = \begin{cases} 0 & \text{if } \; b_{\mathrm{lr},n',m'} = 0 \\ 1 & \text{else.} \end{cases} \tag{3.66}$$

Therefore, $\gamma_{\mathrm{bounds},n',m'}$ effectively eliminates deviations between model and satellite for low-resolution grid points, whose values are entirely determined by the boundary values. Note that this only has an influence in case of $t \neq t_0$. Nowcasting runs are started in the setup used in this work at times which are multiples of 5 min. These are exactly the times MSG rapid images would be available. As the assimilation-inspired procedure takes ASI images from earlier timesteps into account, the optimization start time t_0 is not equal to the time where MSG images are available. The use of $\gamma_{\mathrm{bounds},n',m'}$ therefore has an influence.

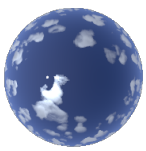

The cost function is the sum of the original ASI-only cost function J in Eq. 3.49 and the additional satellite cost function in Eq. 3.64

$$J_{\text{MACIN-S}}(\text{cm}, u, v, b) = J(\text{cm}, u, v, b) + J_{\text{sat}}(\text{cm}). \tag{3.67}$$

The derived satellite cloudiness can take values greater than 1 according to Eq. 3.57. Therefore, the bounds for cloudiness during optimization of the cost function was set to

$$0 \leq \text{cm} \leq \frac{1}{1 - \frac{k_{\text{occl}}}{k_{\text{clear}}}} \tag{3.68}$$

with the upper bound derived from the condition of non-negative DNI(cm) ≥ 0 and Eq. 3.54.

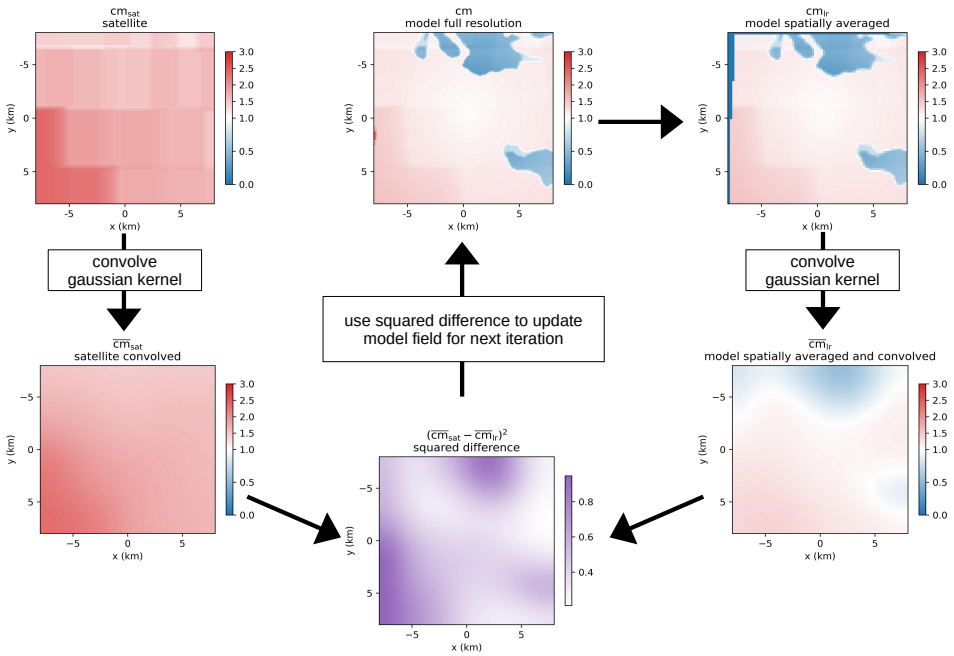

Figure 3.23: As Fig. 3.22, but for a scene with high cirrus clouds at 15:00:00 UTC on 03 July 2021. Shown model states correspond to the values after five iterations of optimization.

The satellite input field, the model state in high and low resolution, the gaussian convolved low-resolution fields, and the resulting deviation which is used to calculate the update for iterative optimization of the cost function are visualized in Fig. 3.22 for a cumulus scene and in Fig. 3.23 for a cirrus cloud scene. In the cumulus scene, the satellite does not detect clouds in the region depicted by the ASIs. This miss is most likely due to the limited resolution of MSG, its pixel size is larger than the scale of single clouds. In the cirrus scene, the satellite detects cirrus clouds for the entire model domain. Satellite

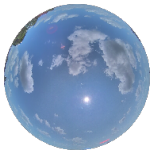

cloudiness observations larger than one thereby mean that the satellite observations suggest larger cloud optical depth, than the RT parameterization in MACIN-S would expect. Also, the satellite observations suggest spatial variations in the cloud optical depth. The derived ASI cloud masks would not be able to describe such variations and the satellite observations may contribute helpful information in this case.

Several things should be mentioned about the above presented method. The lower resolution grid was introduced for computational efficiency and the choice of 200 m is arbitrary. Also, the choice of $\sigma_c = 4\,\text{km}$ is most likely in the right order of magnitude but needs further optimization in future studies. Finally, the spatial averaging and the convolution with a gaussian filter could also be represented in an observation error covariance matrix. However, the description here follows the actual implementation and this work does not give the procedure in terms of an observation error covariance matrix.

3.7 Error Measures

This section is based on the definitions of error measures in Sect. 2.3 of Gregor et al. (2023) and extends these for this work.

To quantify the performance of applied methods, several error measures are used throughout this work. Most of them rely on a comparison of the derived or nowcasted value x_i and the reference value $x_{\text{ref},i}$. The index $i \in 1, ..., N$ is a running index that reflects that the error measures are a statistic over N values, for example, grid points and times. The error measures used are the root-mean-square-error

$$\text{RMSE} = \sqrt{\frac{1}{N}\sum_{i=1}^{N}(x_i - x_{\text{ref},i})^2}, \tag{3.69}$$

and its normalized version

$$\text{NRMSE} = \sqrt{\frac{1}{N}\sum_{i=1}^{N}\left(\frac{x_i - x_{\text{ref},i}}{x_{\text{ref},i}}\right)^2} \tag{3.70}$$

as well as the mean-bias-error

$$\text{MBE} = \frac{1}{N}\sum_{i=1}^{N}(x_i - x_{\text{ref},i}). \tag{3.71}$$

To easily benchmark nowcasts against smart persistence, skill is used as

$$\text{skill}_{\text{RMSE}} = 1 - \frac{\text{RMSE}}{\text{RMSE}_{\text{pers}}}. \tag{3.72}$$

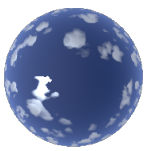

For the evaluation of cloud masks, the pixel accuracy determines how many pixels were detected correctly as clear or cloudy as

$$\mathrm{PA} = \frac{\mathrm{CCLR} + \mathrm{CCLD}}{N_{px}} \tag{3.73}$$

where CCLR and CCLD are the number of correctly clear and cloudy classified pixels compared to the overall number of pixels N_{px}.

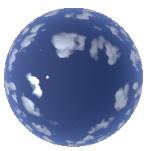

Chapter 4

Validation and application of nowcasting models

4.1 Validation of MACIN with synthetic data

MACIN and its components were validated on synthetic data as described in this section. Section 4.1.1 gives the validation of cloud information derived from ASI images. Additional to the validation of derived cloud information, the performance of MACIN DNI nowcasts in the synthetic setup is assessed in the first part of Sect. 4.1.2. Further DNI nowcasts were performed for additional synthetic setups to investigate nowcast error sources. These setups, results of nowcasts and findings are described in the remaining parts of Sect. 4.1.2. *Large parts of this section are taken from Gregor et al. (2023) and references were updated for this work. Section 4.1.1 consists of Sect. 3.1, 3.2, and 3.3 of Gregor et al. (2023). The first part of Sect. 4.1.2 corresponds to Sect. 3.4 in Gregor et al. (2023).* Note, that in accordance with Gregor et al. (2023), the ASI-based MACIN was used with constant cloud mask uncertainty (cf. Sect. 3.4.5) in this section.

4.1.1 Derived cloud information

Cloud mask

The CNN cloud mask model was successfully trained and validated on hand-labeled real-world images, as explained in Sect. 3.4.1 [...]. We evaluate derived cloud masks to show that it is reasonable to apply the cloud mask CNN to the synthetic images in this study. We calculated the path cloud optical depth (τ) for all viewing angles of our ASI and every desired time step. Together with a threshold, this gives a reference cloud mask. To validate pixel-wise cloud classifications, we use a threshold of $\tau_{\text{thresh}} = 1.0$ to create reference cloud masks from τ. Values of $\tau \geq \tau_{\text{thresh}}$ are linked to cloudy areas in these τ_{thresh} cloud masks. We evaluated CNN cloud masks from ray-marching images for position P1 and 360 time steps at 60 s intervals covering all LES times. The contingency table (Table 4.1) displays the distribution of classes of τ_{thresh} cloud masks against our CNN cloud masks. In general, we find very good compliance. Each of the cloudy and clear classes makes up about 50 % of the compared pixels, which corresponds well to the τ_{thresh} cloud masks. Cloud masks of our CNN exhibit a slight bias towards classifying too few pixels as cloudy. Pixel accuracy

Table 4.1: Contingency table for the cloud mask classes from the CNN and cloud optical depth τ in the line of sight thresholded given by $\tau_{\text{thresh}} = 1$ as a reference. All values are given as a percentage.

		Reference		
		$\tau < 1.0$	$\tau \geq 1.0$	$\sum$
CNN	Clear	46.43	2.54	48.97
	Undecided	0.22	0.25	0.47
	Cloudy	2.33	48.23	50.56
	$\sum$	48.98	51.02	100

is PA = 94.66 % against the τ_{thresh} cloud masks.

Beyond ray-marching images, we calculated 29 MYSTIC images and computed CNN cloud masks for these. By doing the same with corresponding ray-marching images, we could ensure that the derived cloud masks exhibit similar performance for both image generation approaches. As MYSTIC images are physically correct, we conclude that the usage of approximated ray-marching images does not affect the validity of our results.

Cloud-base height

We used data from for the entire LES scene and, effectively, 319 time steps with clouds for the validation of derived CBH. Ray-marching images taken at P1 and P2 were used to derive the CBH as in the nowcasting model. Computed scattering positions give the reference CBH. As our nowcasting model assumes a single cloud-base height, we average the derived CBH per image pair. Figure 4.1a shows the derived average CBH per image pair and the corresponding reference CBH. For these averaged heights, we obtain a MBE for the mispointing method of 50.7 m, an RMSE of 56.9 m, and a NRMSE of 4.0 %. When subtracting the found bias of 50.7 m from the derived image average cloud-base heights, the RMSE could be reduced to 25.6 m and NRMSE to 2.6 %. Increasing systematic error can be observed for the reference CBH up to about 1400 m. A histogram of all derived pixel heights, which are the basis for the averaged CBH, and their reference is shown in Fig. 4.1b. Similar to the image-wide average cloud-base height, derived pixel heights show good agreement with reference heights and a small systematic overestimation. Reference pixel heights show a wider distribution compared with derived values, resulting in the stripes visible in Fig. 4.1. Found height errors could result from discrete viewing directions due to the limited resolution of images, from the projection process, and from the discrete stepping of the image generation ray-marching algorithm. Error sources were not investigated further, as errors are in the range or even lower than those found in other studies with respect to derived cloud-base heights (e.g., Nguyen and Kleissl, 2014; Kuhn et al., 2019; Blum et al., 2021). Equally, no additional work was done to mitigate the observed systematic errors for use in nowcasting.

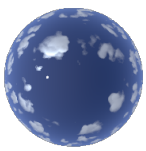

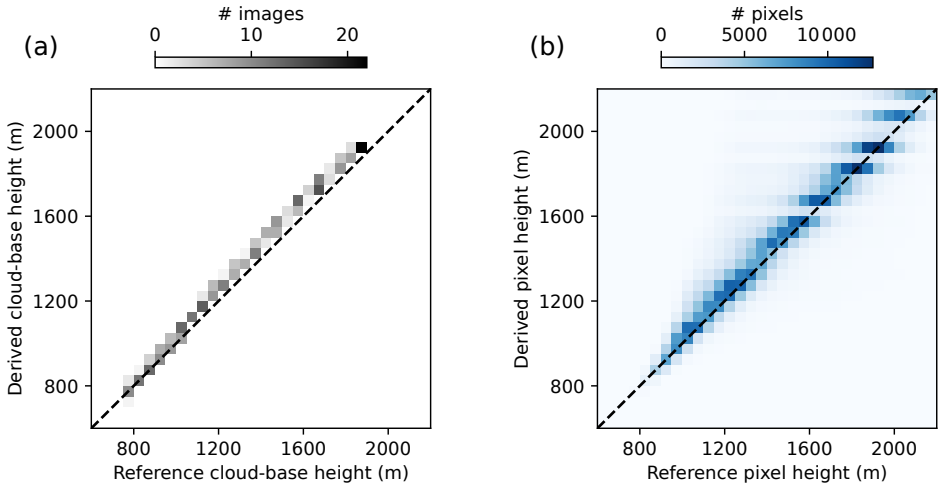

Figure 4.1: Histogram of **(a)** image mean cloud-base height and **(b)** height derived for the matched pixels of all images compared against synthetic references.

Cloud motion

As wind is not necessarily an exact benchmark for cloud motion in convective cloud scenes, we chose two ways to validate our derived cloud motion for two cases. Cloud motion according to the LES is used as a convective case where clouds also develop and decay. Additionally, we are interested in the performance when cloud motion is pure advection, i.e., only displacement of frozen cloud fields. This advective case allows one to derive an exact reference for cloud motion, and the convective case allows one to validate the quality of the derived cloud motion in the presence of clouds that change their size and shape.

Validation of cloud motion in the convective case is done on images every 60 s for LES times from 0 to 21540 s. Figure 4.2 shows cloud fraction as a function of LES time. The average displacement of the vertically integrated liquid water path (lwp) between time steps is calculated using maximum cross-correlation and used as a reference. This describes mean translation and is, therefore, a proxy for domain-averaged reference cloud motion. Cloud motion vectors derived by sparse matching are averaged per time step and ASI and are compared against this reference. Figure 4.2 shows zonal and meridional winds derived for both the ASI and the reference determined by lwp cross-correlation. The cloud fraction derived from cloud masks of an ASI at P1 is given as an indicator of the cloud situation. Up to an LES time of approximately 3600 s, no significant visually detectable clouds are present; therefore, no velocities are derived. Up to approximately 6000 s, derived velocities are relatively unstable over time, with changes in estimated velocities of up to $1.7\,\mathrm{m\,s^{-1}}$ over 60 s. We relate this to the rapidly changing nature of small convective clouds in combination with a low cloud fraction. During this time, some of the small clouds appear and disappear in between time steps and are, therefore, mismatched. After approximately 6000 s, derived zonal velocities vary in a range of $\pm 0.5\,\mathrm{m\,s^{-1}}$ between time steps. Zonal cloud motion close to zero matches the LES initialization without zonal wind. Meridional

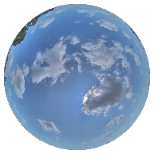

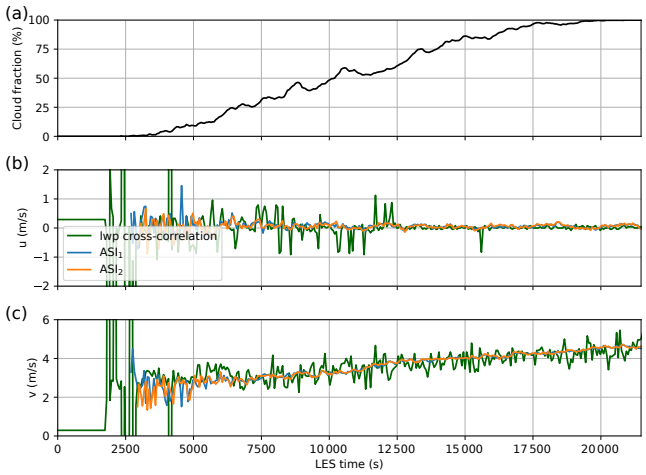

Figure 4.2: **(a)** Cloud fraction from cloud masks of the ASI at P1 for LES times. Per time step scene-averaged cloud motion derived using cross-correlation of the lwp field of the LES simulation and our cloud motion derivation based on feature matching for east to west motion u **(b)** and south to north motion v **(c)**.

velocities increase from about $3\,\mathrm{m\,s^{-1}}$ at 6000 s to a maximum of $4.7\,\mathrm{m\,s^{-1}}$. In general, our derived zonal velocities show a less noisy estimate compared with the reference. Derived velocities from both ASIs show very similar patterns. This further affirms the stability of the cloud motion derivation. However, we do not have an absolute reference to benchmark derived velocities in the convective case, as pure displacement of convective clouds is hard to capture and may differ strongly from main winds. We validate derived cloud velocities using artificially advected cloud fields to overcome this limitation. The same LES times as in the convective validation are used, but each time step is assumed to be independent. Cloud motion is generated by freezing the cloud field and shifting it for each time step. This results in an objective reference cloud motion. A shift of 500 m from north to south at a time difference of 60 s gives a theoretical u of $0\,\mathrm{m\,s^{-1}}$ and v of $-8.3\,\mathrm{m\,s^{-1}}$. No velocities were derived in the absence of clouds up to approximately 2500 s. For longer times, the derived velocities match the theoretical displacements well with an RMSE of $0.019\,\mathrm{m\,s^{-1}}$ zonally and $0.11\,\mathrm{m\,s^{-1}}$ meridionally.

Overall, these results prove that the derived cloud motions are reliable for the cloud situations used in this study. This can also be seen as a further validation of derived CBHs, as they are necessary for the calculation of physical velocities.

4.1.2 Direct normal irradiance nowcasts

MACIN DNI nowcasts on synthetic data are validated and investigated in this section. *The first part of this section is taken from Gregor et al. (2023) and addressed DNI nowcast performance. References were adapted where necessary.* Additional nowcasts for different setups and configurations are evaluated in further parts of this section to investigate now-

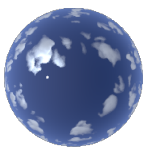

cast error sources beyond the work of Gregor et al. (2023). For better readability this work differentiates between setup and configuration to indicate two different things. A setup refers to the cloud scenes used for nowcasting, while a certain configuration stands for a specific composition of the nowcasting model.

Nowcast performance

Evaluation of the nowcasting model is done using multiple steps that are described and discussed in the following. MACIN is compared against persistence to evaluate overall performance. Additionally, variations of MACIN using ideal cloud masks were run to investigate the implications of errors in CNN-derived cloud masks. These variation runs will be called "cloud mask variation" and "continuous cloud mask variation" hereafter and explained later on. Finally, a simplification of MACIN is used to assess possible benefits of the expensive assimilation of MACIN. This variation will be referred to as "simple variation". For MACIN and all its variations, one nowcast run was started every 60 s for LES times from 60 to 21 540 s for a total of 359 nowcast runs. The maximum nowcast lead time was chosen as 20 min. Nowcast time steps exceeding the maximum LES time of 21 600 s were discarded. DNI nowcasts are always derived simultaneously for point P1 and area A1. Errors for point and area forecasts show similar characteristics. Therefore, they are discussed jointly in the following. If not stated otherwise, error values are given for the point DNI with the area DNI given in parentheses.

Figure 4.3a and b show the average RMSE and MBE for point nowcasts of persistence, MACIN, and cloud mask variation grouped by lead time. Figure 4.3c and d give the same for area nowcasts. Errors of persistence and MACIN give the overall performance of the introduced nowcasting model and are, therefore, analyzed first. Persistence nowcasts start without error at a lead time of 0 min, but the RMSE increases strongly up to approximately a constant value of 300 $\mathrm{W\,m^{-2}}$ (250 $\mathrm{W\,m^{-2}}$) after 6 min. The persistence MBE increases linearly up to approximately 50 $\mathrm{W\,m^{-2}}$ and is linked to the tendency of a growing cloud fraction over time. MACIN exhibits a nonzero RMSE at nowcast start but a smaller increase in the RMSE over time compared with persistence. In terms of the RMSE, MACIN outperforms persistence for lead times longer than 1min. Improvements over persistence for these longer lead times are thereby typically on the order of 50 $\mathrm{W\,m^{-2}}$ (50 $\mathrm{W\,m^{-2}}$) or more. In general, the RMSE of nowcasts for areas is about 50 $\mathrm{W\,m^{-2}}$ lower than nowcasts for points. The MBE is mostly negative for MACIN, with magnitudes in the range of the persistence MBE. The nonzero RMSE at a lead time of 0 min may be a result of erroneous cloud masks in the region of the Sun, errors in the radiative transfer (RT) parametrization, or smearing out during the assimilation because of multiple time steps and viewing geometries.

To further investigate the initial nowcast error discussed above, a cloud mask variation of MACIN was run. Perfect cloud masks were used as input for the nowcasting model instead of CNN cloud masks. These perfect cloud masks are derived from the LES cloud

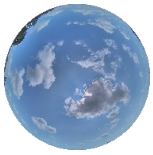

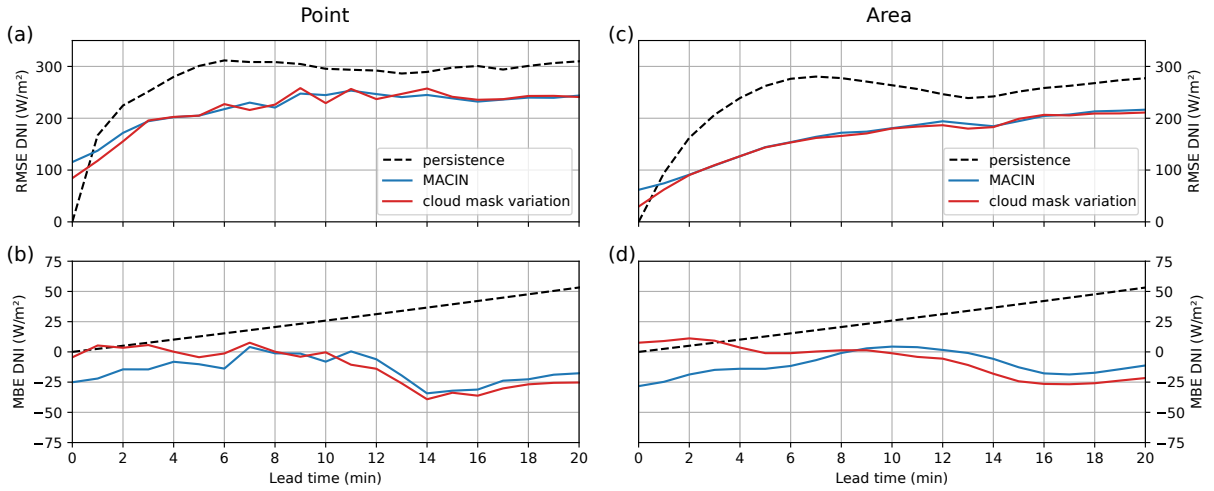

Figure 4.3: The **(a)** RMSE and **(b)** MBE for 359 point DNI nowcasts compared to DNI point reference values and evaluated per lead time. Nowcasts were done using MACIN and the cloud mask variation. Panels **(c)** and **(d)** show corresponding error values for the area nowcasts and DNI area reference.

optical depths in the line of sight τ (see also Section 3.2.1 and Fig. 3.2f) with a threshold of $\tau_{\text{thresh}} = 1.0$ to distinguish between cloudy and clear-sky conditions. By using these perfect cloud masks for nowcasting, the influence of cloud mask errors within the nowcasting model can be assessed. As for the persistence and MACIN, nowcast errors for the cloud mask variation are given in Fig. 4.3. The RMSE of the cloud mask variation is very similar to the RMSE of MACIN. This suggests that the CNN cloud masks provide a good estimate of the cloud situation for our nowcasting. However, the cloud mask variation outperforms MACIN by $31\,\mathrm{W\,m^{-2}}$ ($32\,\mathrm{W\,m^{-2}}$) for a lead time of 0 min and converges to the RMSE of MACIN for lead times of 3 min and longer. The cloud mask variation point MBE is initially about $0\,\mathrm{W\,m^{-2}}$; therefore, the negative MBE of MACIN, especially during the first minutes of the nowcasts, can be associated with erroneous cloud masks in the vicinity of the Sun. The minor improvement for longer lead times when using perfect cloud masks might also be a result of the convectively growing, shrinking, and reshaping clouds. As the nowcasting model cannot describe these processes, perfectly outlining clouds in the beginning may not be that relevant for longer lead times. The nonzero RMSE of the cloud mask variation for a lead time of 0 min may result from errors in the RT parametrization or smearing out by assimilation, as described for MACIN before. To further investigate the implications of the RT parametrization, the continuous cloud mask variation was run. It differs from MACIN only with respect to the input cloud masks. In contrast to the cloud mask variation, which gives discrete cloud mask values for clear-sky and cloudy classes, the continuous cloud mask variation relies on cloud masks with continuous values. The RT parametrization maps model cloudiness states linearly to DNI values. Model cloudiness states of MACIN usually rely on CNN cloud masks with discrete values for the three classes (clear, cloudy, and undecided), whereas actual cloud optical depth is a continuous variable. Continuous cloud masks are used to check whether this discrete representation causes a

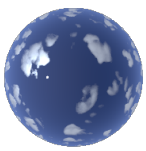

significant fraction of nowcast error. These cloud masks are derived from τ used for the cloud mask validation, but they comply with the exponential attenuation of intensity in radiative transfer by $\mathrm{cm}_{\mathrm{cont}} = 1 - \exp(\tau)$. The continuous cloud mask variation uses these continuous cloud masks. The resulting errors of the continuous cloud mask variation are not depicted, as they strongly resemble the errors of the cloud mask variation with slight improvements in the RMSE in the range of about $\pm 5\,\mathrm{W\,m^{-2}}$. Therefore, we conclude that the RT parametrization and discrete nature of cloud masks is not a major error source, and the nonzero RMSE for a lead time of 0 min is a result of smearing out during assimilation.

A further variation of MACIN was run to assess the benefits of the assimilation scheme. Therefore, the simple variation of MACIN was run with just a single cloud mask and velocity field from the ASI at P1 as input. The Sun region is not masked out in the cloud mask and velocity field for the simple variation. With this variation, we assess the possible benefits of the additional complexity and computational cost of MACIN. The resulting errors differ from the errors of MACIN, mainly for point nowcasts. For a lead time of 0 min, the RMSE of the simple variation is about $300\,\mathrm{W\,m^{-2}}$. For longer lead times, the RMSE resembles the RMSE of MACIN but is approximately $75\,\mathrm{W\,m^{-2}}$ larger. The MBE of the simple variation is strongly negative, with values of around $75\,\mathrm{W\,m^{-2}}$ and even more for a lead time of 0 min. As the Sun region is not masked out in the simple variation and the cloud mask CNN tends to classify the Sun in synthetic images as cloudy, the initial model cloudiness state is incorrect in this region, and the derived DNI for a lead time of 0 min gives large errors. In case of clear sky, the erroneously cloudy detected Sun is steady; therefore, this "cloud" does not move and gives an offset for all lead times. This explains the large RMSE offset and the large negative MBE. We are aware that these larger errors are mainly due to the co-location of the ASI and nowcasted point in our setup. Nevertheless, this demonstrates the capabilities of our nowcasting model to use multiple data sources for error reduction. For example, when using projected images of ASIs at different positions and superimposing one over the other for the derived CBH, the Sun is in different regions of the images. When we exclude, per the ASI, the immediate region of the Sun from the used cloud mask, cloud mask information from another ASI is used to fill in this region. Thus, erroneous cloud masks in the region of the Sun can be mitigated by assimilation.

In general, the nowcast quality is influenced by the variability in DNI. Completely cloud-free and also fully overcast situations result in low variability and are simple to nowcast. Broken clouds can cause strong variations in DNI and are more challenging to nowcast. Therefore, other nowcasting systems in the literature (e.g., Nouri et al., 2019a) are benchmarked not only on all available situations but also separately on situations grouped into eight variability classes. This showcases the nowcast quality under different weather conditions and variability. We investigated the performance of MACIN by computing error metrics for subsets of the 359 nowcasts of this study. The subsets were determined by the cloud fraction. Overall, a small absolute RMSE can be found, especially for small and large cloud fractions, with minor to no improvements in MACIN over persistence. Errors are larger for broken clouds and medium cloud fractions, and the improvement in MACIN over persistence increases in these cases. However, the significance of these cloud-fraction-

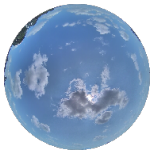

dependent results is limited due to the small number of nowcasts and the restriction to the shallow-cumulus LES data. Therefore, these results are not displayed nor discussed here in detail.

Nowcast errors from viewing geometry

All-sky imagers view clouds from below and viewing angles depend on the relative position. These viewing angles may differ from the angle in which the cloud shadow is cast. The cross section of a cloud seen by an ASI therefore can differ strongly from the cross section of the cloud relevant for the cloud shadow and therefore direct irradiance. This difference is illustrated in Fig. 4.4. The viewing geometry of an ASI converges towards the imager, while direct sun light is approximately parallel with an incidence angle dependent on the position of the Sun. Kurtz et al. (2017) found that this difference between cloud cross section as derived in ASI cloud masks and the cloud cross section relevant for shading strongly impacts the performance of ASI nowcasts.

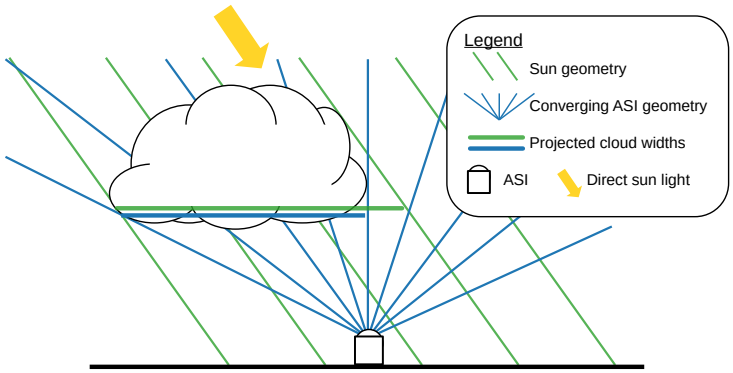

Figure 4.4: Illustration of the cross section of a cloud as viewed by an ASI due to its converging geometry and the cross section of the cloud for the parallel geometry of sun light, which is relevant for shadows on the ground.

With the synthetic setup in this study this systematic nowcasting errors due to the imperfect viewing geometry and cloud projection are revisited as described in the following. The nowcasting model was run again on the LES cloud data, but with another set of input cloud masks. To obtain cloud masks actually representing the cloud cross section relevant for shadows, previously computed direct irradiance fields were exploited. With knowledge about clear-sky $\mathrm{DNI_{cs}}$, cloud optical depth τ towards the Sun can be computed as

$$\tau = -\ln\left(\frac{\mathrm{DNI}}{\mathrm{DNI_{cs}}}\right) \tag{4.1}$$

from reference DNI computed with MYSTIC. A threshold $\tau_{\mathrm{thresh,\,sun}} = 0.3$ was chosen to construct discrete sun geometry cloud masks. The value of 0.3 was determined in order to approximately match the number of cloudy pixels in the CNN derived cloud masks.

Nowcast runs with these sun geometry cloud masks will be indicated by *sun geometry* in the following.

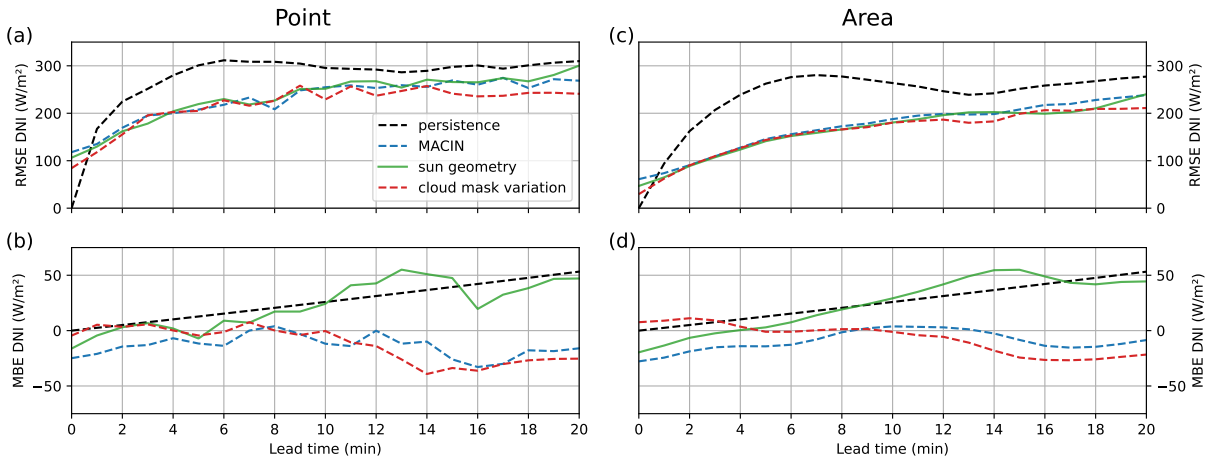

Figure 4.5: **(a)** RMSE **(b)** MBE for 359 point nowcasts with sun geometry cloud masks. As a reference, errors of persistence and corresponding MACIN nowcasts with CNN derived cloud masks as well as cloud mask variation nowcast errors are given. **(c)** and **(d)** give the same for area nowcasts.

359 nowcasts were performed, starting in intervals of 60 s for the full LES times. In the following, nowcast performance for point nowcasts is discussed with respect to the baseline MACIN and *cloud mask variation* nowcasts. RMSE and MBE for the *sun geometry* nowcasts and the reference nowcasts are given in Fig. 4.5. Similar to MACIN nowcasts, RMSE is non-zero in the beginning and increases faster for small lead times than large lead times. *Sun geometry* nowcasts outperform MACIN nowcasts for lead times up to 3 min by up to about 20 W m^{-2} and show comparable performance for longer lead times. A positive tendency can be observed in MBE of *sun geometry* nowcasts, comparable to the positive tendency of persistence nowcasts, but with variations of up to 25 W m^{-2} and not as linearly.

As the cloud masks for *sun geometry* are derived from the reference, improved RMSE performance in the beginning meets expectations due to the better initial knowledge about the cloud situation. A difference between *sun geometry* and *cloud mask variation* nowcasts for these small lead times can be explained by the different cloud optical depth thresholds used. As a $\tau_{\text{thresh}} = 0.3$ was chosen for the sun geometry cloud masks, initial RMSE and MBE differs from *cloud mask variation*, where a threshold of cloud optical depth 1.0 was assumed. While relevant cloud size is overestimated for distant clouds in converging ASI geometry, *sun geometry* cloud masks give a more objective cloud size and therefore no strong negative DNI bias. The similar tendency over lead time between *sun geometry* nowcasts and smart persistence suggest that there is no significant erroneous bias in estimated cloud fraction over time. The small improvement in RMSE over MACIN in the beginning and no significant improvement for longer times suggests once more that derived CNN cloud masks are already really good and that initial good knowledge about cloud geometry

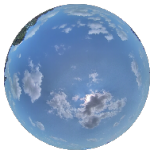

is not helpful for longer lead times, as cloud evolve and change shape which is not modeled in MACIN.

Nowcast errors from cloud evolution

In the nowcast runs of MACIN on synthetic data, also perfect cloud masks did not lead to perfect nowcasts. The RT parametrization, smoothing by the assimilation-inspired scheme and restriction of cloud evolution to simple displacement were proposed as possible error sources. A nowcasting experiment was designed, where clouds behave as represented in the nowcasting model. These clouds are only displaced over time and do not shrink, grow or reshape. The synthetic cloud data and ASI image generation allow for such a setup by freezing the LES cloud field and shifting it over time. This setup will be called *no-evolution setup* in the following. Comparability with the reference run from Gregor et al. (2023) and explained before is desired. This allows to assess the implications of complex cloud dynamics for nowcast errors. For comparison with the reference run, the corresponding LES cloud field is frozen per nowcast start time and displaced with the mean velocity derived in the reference run for this time. Due to the discrete nature of the LES cloud grid, this displacement velocity is rounded to an integer number of shifted grid cells per $\Delta t = 60\,\mathrm{s}$. However, the cloud fraction increases in the LES cloud data over time and also throughout reference nowcast runs whereas it is constant for the frozen cloud fields within a nowcast run for a single start time of the *no-evolution setup*. Therefore, the reference run was extended by additional nowcasts on the LES cloud fields. The existing forward reference runs with an increasing cloud fraction were supplemented with nowcast runs on reversed LES times backward and with decreasing cloud fraction. Within this section *evolution setup* will be used to indicate this forward and backward setup for the MACIN. Also the *no-evolution setup* describes two nowcast runs per start time. The frozen LES cloud fields are shifted once according to the forward velocities from the *evolution setup* and once according to the backward velocities. This is done to equalize the number of nowcasts between the two approaches and also account for the fact that the overall cloud movement is from south to north for the forward direction and north to south for the backward direction, i.e. the distance between clouds moving into the view of the ASI and the Sun in the images differs depending on the time direction. DNI irradiance reference fields are computed as described in Sect. 3.2.1. Also, persistence is calculated separately for the clouds of the *evolution setup* and the *no-evolution setup*.

The nowcasting errors are shown in Fig. 4.6. The *evolution setup* nowcasts show similar error patterns as observed for the forward-only reference run in Gregor et al. (2023), but the reduction of RMSE compared to the persistence is smaller. This can be attributed to the nowcast runs on the *evolution setup* being performed to LES cloud data in forward and backward time direction. In general, the nowcasting model overestimates the cloud fraction especially for larger lead times and therefore for clouds close to the horizon. The actual LES cloud fraction increases in forward time direction for the *evolution setup*. This coincidence between erroneous overestimation and actually increasing cloud fraction re-

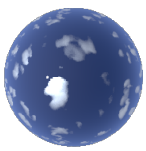

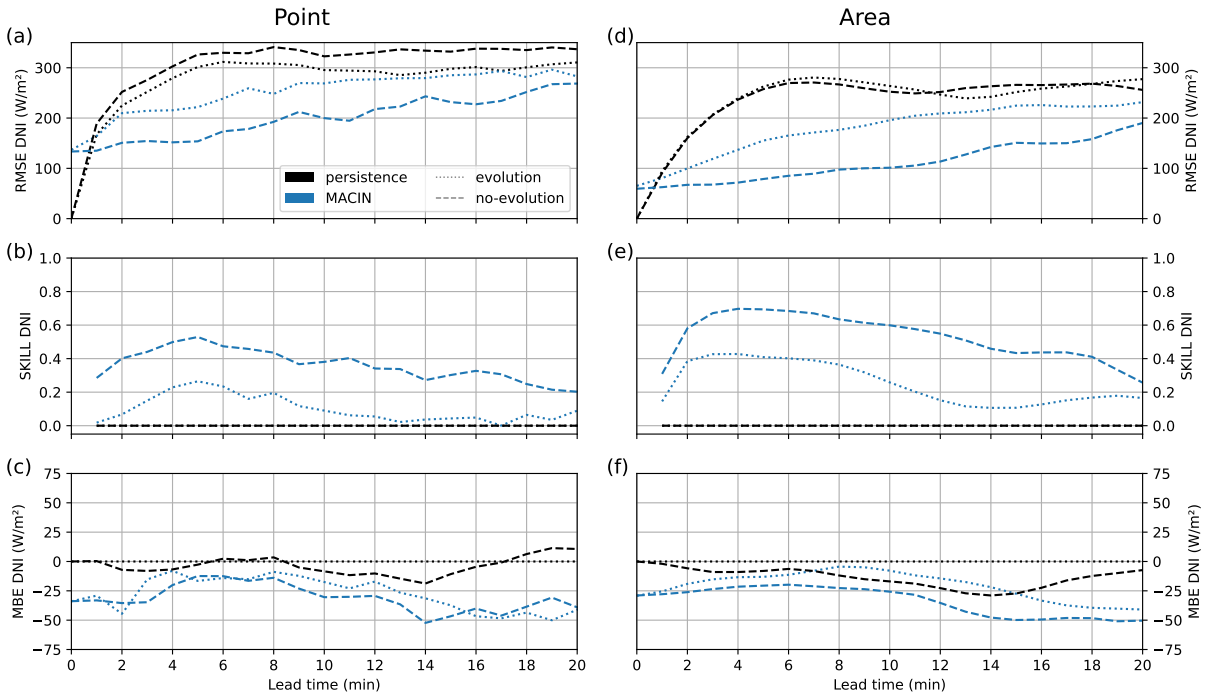

Figure 4.6: **(a)** RMSE, **(b)** skill and **(c)** MBE for 718 nowcasts performed with MACIN on synthetic cloud data with cloud evolution and without cloud evolution. As a reference, errors of persistence are given.

duces nowcast errors for the forward time direction. In contrast, LES cloud fraction for the *evolution setup* decreases in backward time direction and contradicts the nowcasting models overestimation. The nowcast errors for the backward time direction are therefore larger than for the forward time direction for the *evolution setup*. LES cloud fraction is constant per nowcast time for the *no-evolution setup* and therefore this difference between forward and backward time direction cannot be observed for this setup.

The *no-evolution setup* nowcasts exhibit the same large RMSE for nowcast start as *evolution setup* nowcasts, but only slowly increasing error over time. However, the cloud situations are not exactly equal for the *no-evolution setup* and *evolution setup* nowcasts as indicated by the difference in respective persistences. The comparison of both setups for lead times larger than 1 min is therefore done by evaluating skill, which describes the improvement over the corresponding persistence (cf. Fig. 4.6). Overall, skill of the *no-evolution setup* nowcasts shows improvements of 0.2 and more over *evolution setup* nowcasts for most lead times. This can be observed for point and area nowcasts equally. For area nowcasts and lead times of 2 min to 13 min, the skill of the *no-evolution setup* is above 0.5, the RMSE is reduced by more than 50% compared to the persistence. On the one hand, this indicates a major nowcast improvement when using the model for situations without growing, shrinking or reshaping clouds. On the other hand, the more complex cloud evolution in the *evolution setup*, which can actually take place in the real atmosphere, is a major hurdle for good nowcasts and reduces the performance of the nowcasting model

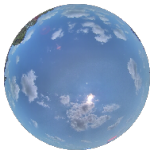

significantly.

Nowcast errors from viewing geometry and cloud evolution combined

An additional synthetic nowcasting experiment was designed to investigate the joint effect of both systematic errors described above. The combined assumption of advected, non-evolving clouds as well as the converging ASI geometry are part of MACIN and other ASI-based DNI nowcasting models. This experiment is designed to showcase the joint errors resulting from these sources. Therefore, synthetic cloud scenes of the *no-evolution setup* described above were used with one difference. Cloud masks complying to the sun geometry were derived for these cloud scenes and injected into the nowcasting model instead of the CNN derived cloud masks. The performance of nowcasts of the MACIN configuration with sun geometry cloud masks in the *no-evolution setup* is evaluated in the following. This combination of the sun geometry configuration of MACIN and the no-evolution cloud scenes will be referred to as *no-evolution sun geometry* experiment in the following.

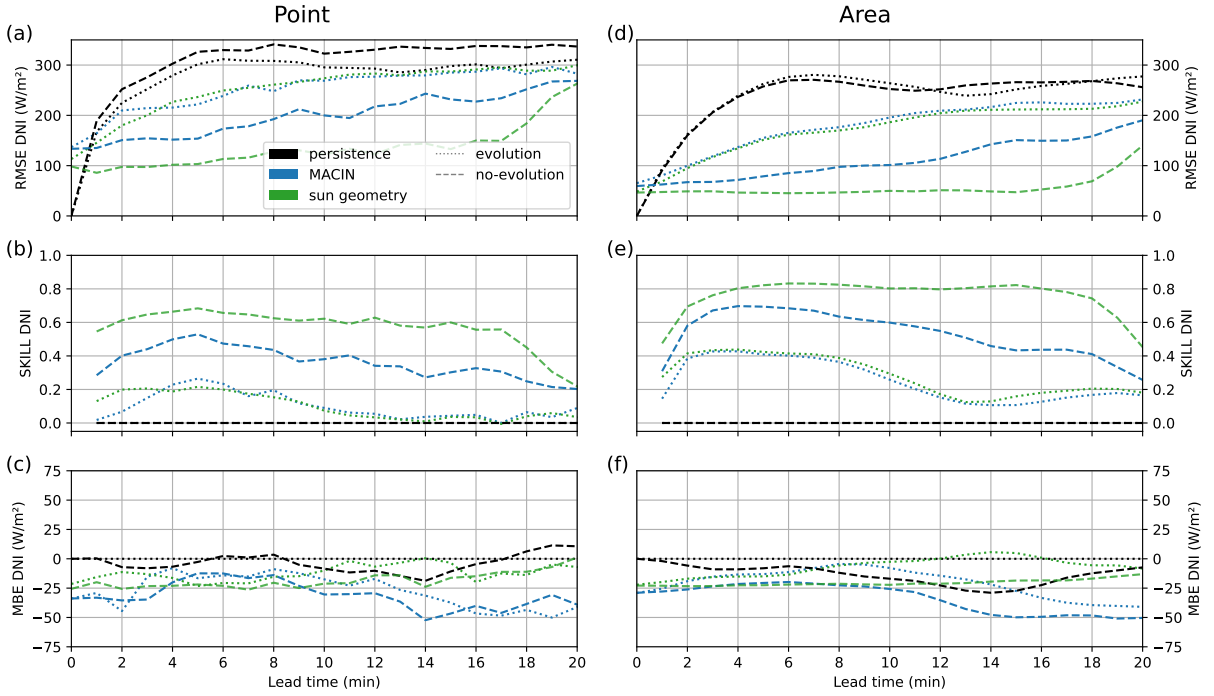

Figure 4.7: **(a)** RMSE, **(b)** skill and **(c)** MBE for 718 nowcasts performed with the sun geometry cloud masks on synthetic cloud data with cloud evolution and without cloud evolution. As a reference, errors of MACIN nowcasts and persistence are given.

The resulting nowcast RMSE, MBE and skill are given in Fig. 4.7. The focus is set in the following on point nowcasts, area nowcasts are displayed in the figure as well for completeness. A strong improvement of skill over all prior nowcasting experiments was

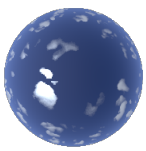

found for the *no-evolution sun geometry* experiment. Before a lead time of 2 min, skill is below 0.6. Skill of 0.6 to 0.7 is observed up to 12 min, afterwards the skill slowly declines. Smaller skill in the beginning is not strictly linked to larger nowcast RMSE of this experiment, but can be explained with smaller RMSE of the persistence during these times. Persistence RMSE and *no-evolution sun geometry* nowcast RMSE are relatively constant for longer lead times, resulting in stable skill. For lead times longer than about 16 min, skill decreases. Initially distant clouds from the ASI become more and more important for DNI at these times. Due to the limited field of view, these are not observed and represented in the nowcasting model. Instead, information outside the domain is estimated by continuous boundary condition. Obviously, this leads to larger errors in the nowcasting experiment. Meanwhile the persistence error for these times stays approximately constant, which leads to a decrease in skill. Compared to the reference run nowcasts, skill is drastically improved by up to 0.6.

Improvement in skill of *no-evolution sun geometry* nowcasts over the *no-evolution* nowcasts is approximately 0.2 and relatively stable up to lead times of about 16 min. In this case, the sun geometry cloud masks are helpful for longer lead times than for *evolution* nowcasts. This supports the hypothesis, that sun geometry nowcasts cannot outperform the reference run nowcast for lead times of more than 4 min due to the strongly evolving clouds. If cloud evolution is eliminated in the *no-evolution* experiments, the additional improvement due to the sun geometry cloud masks is steady over time. Altogether, the *no-evolution sun geometry* experiment demonstrates the potential for a strong improvement in nowcast performance if clouds could be modeled as they actually evolve and geometric representation of the clouds can be improved. Measurement configurations with multiple ASIs imaging the same cloud can help to improve the geometric representation of the cloud. E.g. Nouri et al. (2018) used 4 ASIs for a 3D-retrieval of clouds and an accordingly improved cloud geometry. As a first step towards better cloud geometry in MACIN, the assumption of cloudiness on a flat 2D plane at cloud-base height could be extended to 2D cloud layer with a vertical extent. Modeling the cloud evolution correctly on the required temporal and spatial scales brings up three major problems: physically accurate modeling of all relevant processes, knowledge about the exact initial state and computational constraints. Highly resolved numerical weather prediction models – so called large eddy simulations (LES) – are capable of simulating clouds and turbulence down to scales of 10 meters. Still, some microphysical processes like cloud droplet growth need to be parametrized. Whether these are accurate enough to exactly model evolution of a field of specific clouds for the next minutes would have to be proven. Even in case of a perfect model, chaos theory suggests that small uncertainties in the initial conditions may lead to large deviations in the predicted states. 3D knowledge about winds, temperature, water vapor and more variables would be necessary for a good initial state of a physically accurate model. Deriving this information and therefore an accurate initial knowledge about the atmosphere from 2D ASI images is very challenging. Lastly, running physics simulations on the required scales and accuracy requires large computational power and poses a further challenge as nowcasts have to be provided within single minutes. Overall, modeling cloud evolution for irradiance nowcast-

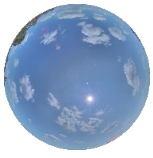

ing remains a major challenge. Statistical models and machine learning approaches can be developed to approximate relevant physical processes, extract most important information encoded in ASI images and are computationally feasible. For example Carpentieri et al. (2023) demonstrated improved nowcast performance through statistical modeling of cloud evolution.

4.2 All-sky imager based nowcast performance on real data

MACIN and its components were extensively validated on synthetic data in Gregor et al. (2023) as described in Sect. 4.1. Additionally, Sect. 3.4.5 and 3.4.6 describe changes compared to Gregor et al. (2023) for the application of MACIN to real-world data. This section evaluates MACIN nowcast performance on real data. Section 4.2.1 explains the chosen cloud situations. DNI nowcast performance is evaluated in Sect. 4.2.2. The focus is on errors of the final DNI nowcasts, intermediate steps are only investigated if necessary to explain observed errors.

4.2.1 Evaluation setup

Settings of MACIN were chosen as in the synthetic experiments, ASI images from forecast start time and 1 min before are used if available. Two ASIs and a sun-tracker with pyranometer were installed in Egling a.d. Paar for the project NETFLEX as explained in Sect. 3.2.2. ASI images are available as MACIN input in 1 min-intervals and reference DNI measurements with the pyranometer in 2 s time resolution which is resampled to 1 min averages. July 2021 was chosen as validation period and nowcasts were started in 5 min intervals between 08:00:00 UTC and 15:00:00 UTC. The restriction to these times was chosen to focus on situations with sun zenith angles less than 60° for which the ASIs capture clouds relevant for occlusion of the sun in the near future. Additionally, the PV plant is tilted towards the south, leading to an increased importance of Sun positions in the south as observed around noon. 2040 nowcasts were performed and evaluated for MACIN configurations with constant cloud mask uncertainty and varying cloud mask uncertainty respectively. 13 and 21 July 2021 were excluded due to missing data. Cloud fraction for the validation period is computed from cloud masks for the ASI-16142 as the average numeric cloud mask value of all pixels with zenith angles smaller than 50°. A tendency towards large cloud fractions was found as displayed in Fig. 4.8, but also days with low cloud fraction can be found around 21 July 2021. Equal to cloud fraction, also image average cloud-base height was computed for the validation period. As shown in Fig. 4.8, low cloud situations with cloud-base height up to 3 km dominate, but also periods with mid-level cloud-base height of about 4 km as well as high-level cloud-base height of more than 8 km are included.

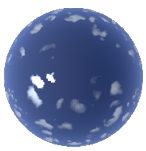

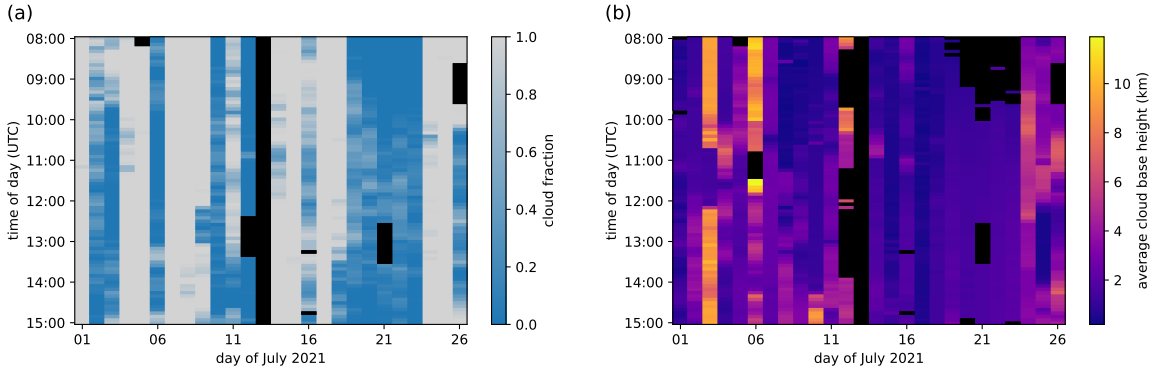

Figure 4.8: Overview of **(a)** cloud fraction and **(b)** image average cloud-base height for all nowcast start times in the evaluation period. Note that the default cloud-base height of 1 km is used in case of existing images but no detected clouds. Black indicates missing data due to missing images. As the stereographic cloud-base height retrieval requires simultaneous images from both ASIs, panel **(b)** shows more gaps.

In the real-world setup, 1 min DNI averages are used as a reference, while DNI references for the synthetic setup were computed for a specific moment in time. To comply better with these 1 min DNI averages used as a reference, the MACIN cloudiness of a larger area around the Sun is assumed to be relevant. For all real-world applications, the cloudiness used for further calculation in the MACIN radiative transfer parametrization is averaged over all model grid points within a 2.5 ° opening angle around the Sun position. For the synthetic setup, this opening angle was 0.5 °. Additionally, cloud situations in real-world situations may be more complex than the LES shallow cumulus cloud fields. The amount of shading can differ a lot more between successive clouds. To account for this, the half-width time of the exponentially weighted mean of the DNI clear-sky indices was increased from 10 min for the synthetic setup to 30 min for the real-world setup. This means, that the expected radiative effect of the next predicted clouds on DNI relies on a longer time series of the measured radiative effect of previous clouds.

4.2.2 Nowcast performance

Figure 4.9 displays RMSE and MBE of MACIN DNI nowcasts along with smart persistence as a reference. The results for the MACIN configuration with constant cloud mask uncertainty as used in the synthetic experiments are discussed first. The alternative configuration with varying uncertainty is discussed at the end of this section and explores the differences between the configurations. For lead times of more than 2 min up to about 19 min RMSE of MACIN nowcasts is approximately 20 Wm^{-2} to 25 Wm^{-2} lower than RMSE of smart persistence. This corresponds to a reduction in RMSE of approximately 7.5% to 10%. For longer lead times, no RMSE improvements are found and MACIN cannot outperform smart persistence for lead times greater than 23 min. Smart persistence is perfect for nowcast start and outperforms MACIN for lead time 1 min as well. MBE of the smart persistence

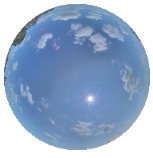

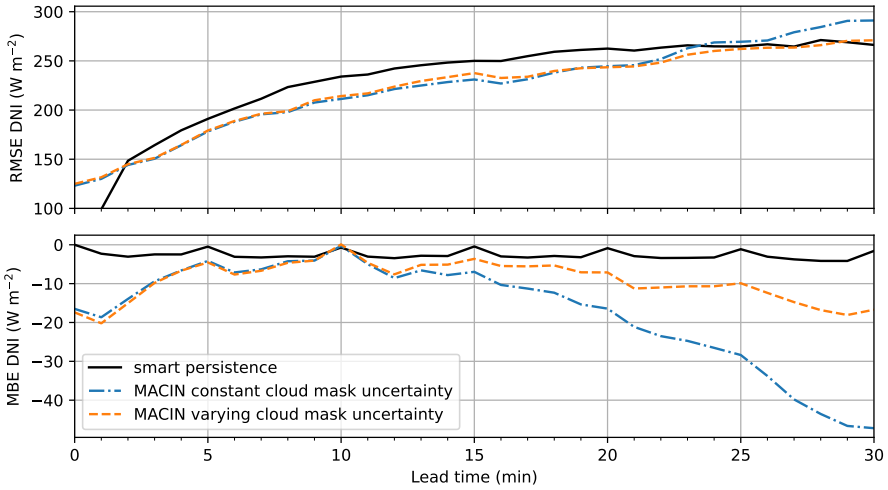

Figure 4.9: RMSE and MBE per lead time for 2040 MACIN DNI nowcasts in July 2021. Performance of smart persistence is given as a reference.

nowcasts is stable and in the range of $0\,\mathrm{Wm}^{-2}$ to $-5\,\mathrm{Wm}^{-2}$ and therefore small compared to RMSE. MBE of MACIN nowcasts is approximately $-20\,\mathrm{Wm}^{-2}$ at the beginning and approximately $0\,\mathrm{Wm}^{-2}$ for lead times of 23 min. An increasing negative MBE can be observed for larger lead times. The structure of these MACIN errors for real-world data complies well with the structure of errors for synthetic data described and discussed in Sect. 4.1.2. MACIN can therefore be used beneficially for real-world applications. However, relative nowcast improvement differs between real-world and synthetic data. Multiple reasons can explain the smaller relative nowcast improvement when applying MACIN to real-world data. These include data quality, cloud scenes, and additional errors from the DNI parametrization. Especially in smart persistence MBE, but also in MACIN MBE,

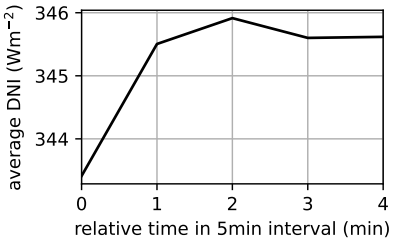

Figure 4.10: Measured DNI averaged per relative minute in 5 min intervals for all nowcast times.

less negative values are observed for times which are multiples of 5 min. This is due to a systematic in the DNI measurements used as reference and basis for the nowcasts. When averaging DNI values for every minute of 5 min intervals, values for minute 0 are on average about $5\,\mathrm{Wm}^{-2}$ less than for minutes 1 to 4 as visible in Fig. 4.10. This matches exactly the MBE structure of smart persistence. The structure within 5 min intervals is also found

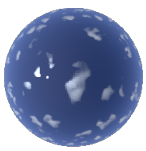

in corresponding PV power measurements (cf. Sect. 5.2.2), which was measured independently by a third party. Fluctuations in the local power grid are assumed to influence the CR6 datalogger and cause these systematics in the measurements.

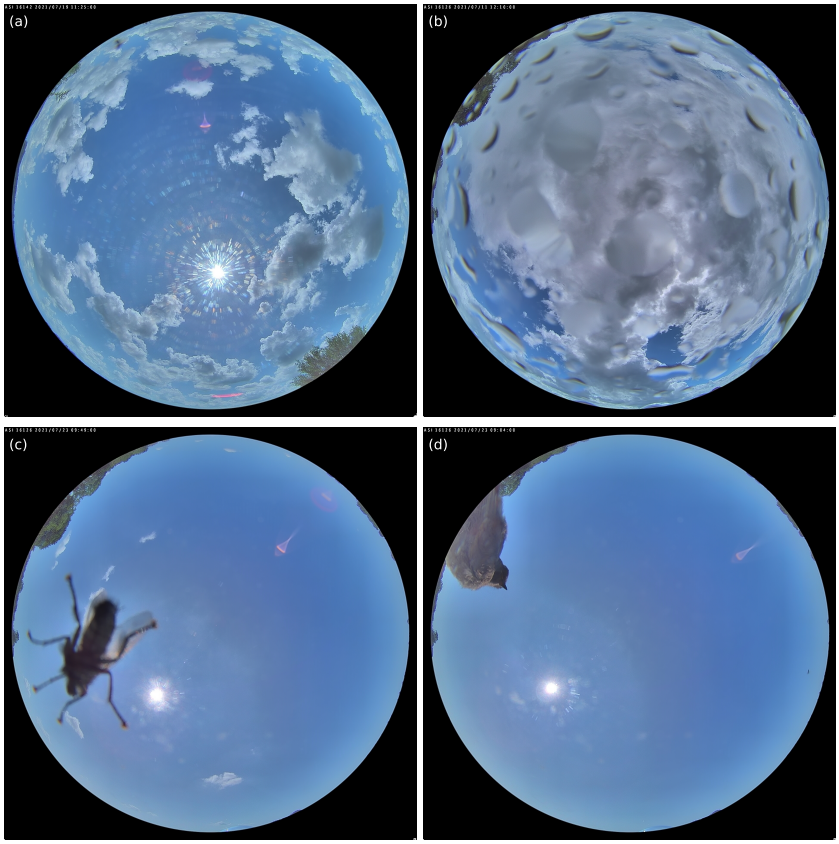

Figure 4.11: Example ASI images of limited quality. **(a)** Refraction on glass dome of ASI-16142 due to spider web at 11:25:00 UTC on 19 July 2021. **(b)** Rain on glass dome of ASI-16126 at 12:10:00 UTC on 11 July 2021. **(c)** Insect in field of view of ASI-16126 at 09:49:00 UTC on 23 July 2021. Pollution in the region of the Sun is visible as well. **(d)** Bird in field of view of ASI-16126 at 09:04:00 UTC on 23 July 2021. An additional example of strong refraction on the glass dome of ASI-16142 is given in Fig. 3.7.

Images used in the real-world cases were not quality controlled. This step was omitted purposely, as MACIN is targeted at actual solar energy applications. Consistent cleaning of the ASI glass dome cannot be guaranteed. E.g., rain drops, insects, and birds are realistic obstructions in the images. Figure 4.11 gives examples of low-quality images used in the validation.

The mis-detection of clouds due to obstruction in the images can obviously lead to increased nowcast errors. As shown in Fig. 4.8, the validation period featured plenty of times of very high or very low cloud fraction. To further investigate this, nowcasts were grouped by cloud fraction at nowcast start time into 5 bins. Error measures were computed per bin and are given in Fig. 4.12. Cloud fraction is more uniformly distributed for the synthetic

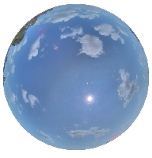

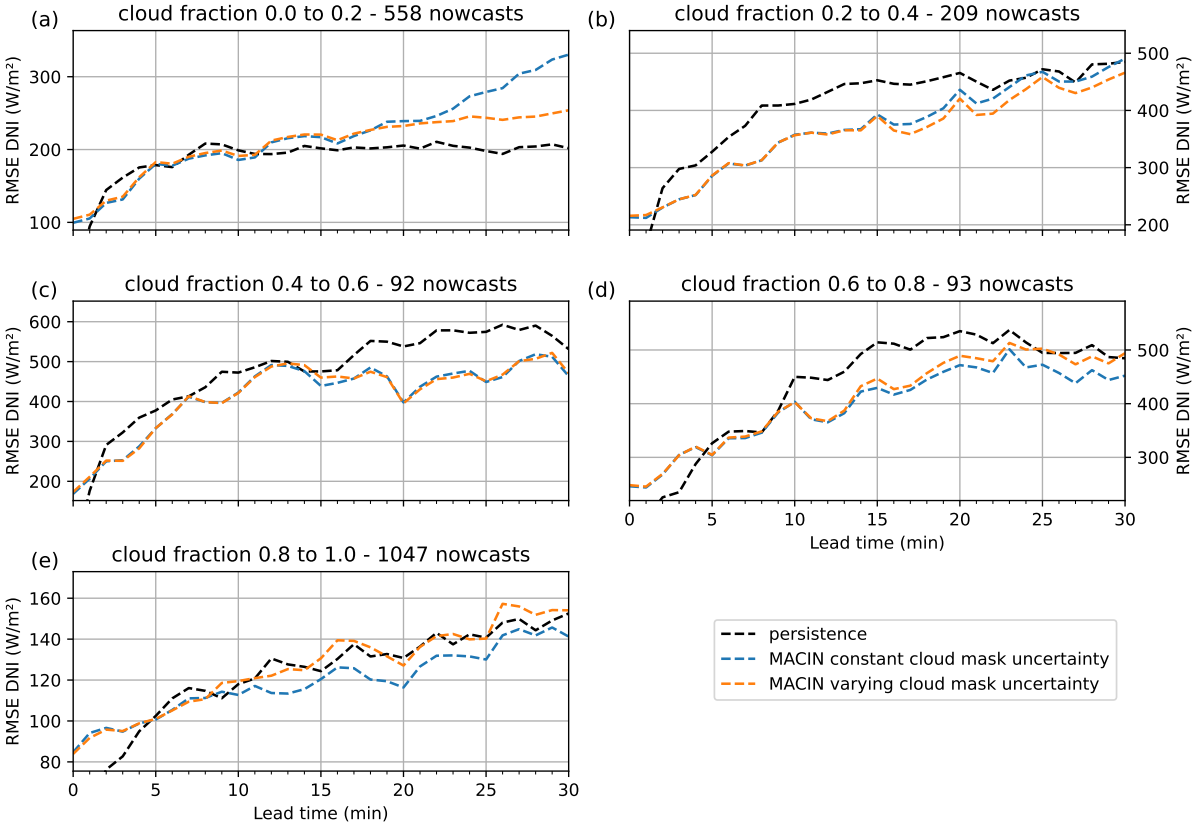

Figure 4.12: RMSE per lead time of 2040 MACIN real-world nowcasts grouped by cloud fraction at nowcast start time. The cloud fraction bin and the number of nowcasts per bin are given in the header of the respective panel. Note the differences in scaling of the Y-axes.

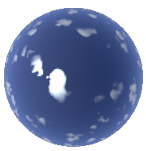

data. More than 51 % of all real-world nowcasts start with cloud fraction of at least 0.8 and more than 27 % start with cloud fraction of less than 0.2. For these extreme cloud fractions, variability is limited and persistence is therefore a good assumption. RMSE improvement of MACIN over persistence is limited for these bins (Fig. 4.12a and e). In these cases, persistence is a relatively good assumption and therefore RMSE improvement over persistence is limited for these bins (Fig. 4.12a and e). As these bins comprise the majority of nowcasts, this directly impacts RMSE performance of all nowcasts together. Outperforming persistence is therefore harder for the real-world dataset compared to the synthetic dataset. For cloud fractions in the range of 0.2 to 0.8, persistence RMSE is larger than for very high and low cloud fractions, most of the time by two or three times. MACIN shows its strength in these situations of broken clouds and large DNI changes and significant RMSE improvements of MACIN can be found. For lead times of about 7 min and more, RMSE for persistence and for cloud fractions below 0.2 is almost constant around 200 $\mathrm{W\,m^{-2}}$, while RMSE for MACIN is strongly increasing to finally about 320 $\mathrm{W\,m^{-2}}$.These striking nowcast errors are most likely connected to the overestimation of distant clouds, which are seen under a large viewing zenith angle.

The synthetic experiments featured a constant position of the sun and a single layer of shallow cumulus clouds. The large cloud optical depth of shallow cumulus clouds is linked to very low transmissivity. The DNI is therefore more or less binary. In real-world applications, all kinds of clouds can be observed, resulting in all kinds of DNI reduction. Furthermore, multilayer clouds can cause strongly different transmissivity between clouds in the same ASI image. The current DNI parameterization assumes a common transmissivity for all clouds in an image, and especially multilayer clouds are not represented in MACIN. The increased complexity of DNI in real-world data is more challenging to nowcast compared to synthetic data.

RMSE per lead time for the MACIN configuration with varying cloud mask uncertainty (cf. Sect. 3.4.5) is displayed as well in Fig. 4.9. In general, errors for both MACIN configurations are similar for lead times up to about 12 min. MBE shows a stronger negative trend for the MACIN configuration with constant cloud mask uncertainty for longer lead times. This can be explained by the use of cloud mask information with $\theta > 75°$ in case of constant cloud mask information. Cloudiness is generally overestimated for larger zenith angles due to the misinterpreted view of cloud sides. This overestimation results in a negative bias of estimated DNI. The configuration with varying cloud mask uncertainty therefore performs better for lead times larger than 21 min in terms of RMSE and is still comparable to smart persistence for these times. RMSE per lead time for the MACIN configuration with varying cloud mask uncertainty was also computed separately for the 5 cloud fraction bins discussed above It is shown in Fig. 4.12. The improved performance of the MACIN configuration with varying cloud mask uncertainty compared to the configuration with constant cloud mask uncertainty is mainly due to a reduction of RMSE for situations of low cloud fraction. Especially the considerable RMSE for cloud fractions below 0.2 and lead times of more than 15min is reduced. Overall, the consideration of nowcast errors per cloud fraction emphasizes that the overestimation of distant clouds is

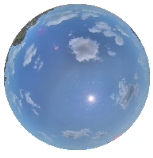

a major error source of MACIN. The varying cloud mask uncertainty partly compensates for this error in some cases. However, the configuration with constant cloud mask uncertainty gives smaller RMSE for cloud fractions larger than 0.6. This effect needs further investigation in future studies.

4.3 Satellite-exclusive nowcast performance

July 2021 was chosen as evaluation period for nowcast performance of satellite only nowcasts performed with the model introduced in Sect. 3.5, analogously to the evaluation of MACIN in Sect. 4.2. Nowcasts were done for the PV plant in Egling a.d. Paar, where DNI measurements are available. APICS and CiPS cloud information can be computed for the 5 min intervals of Meteosat-10 rapid scans, and nowcasts were started accordingly in 5 min intervals between 08:00:00 UTC and 15:00:00 UTC in compliance with the MACIN nowcasts. 2019 nowcasts were performed with the satellite-based model configured as described above. These are 21 nowcasts less than those performed with MACIN due to missing satellite imagery. Cloud optical depth layers (τ_{low} and τ_{up}) are computed according to the threshold-based layer separation. Maximum nowcasted lead time was chosen as 4 h. DNI reference measurements are averaged over 15 min centered around the relevant times. Smart persistence is also computed as a reference based on 15 min DNI measurement averages. However, to conform with the concept of smart persistence as a reference nowcast only information up to the nowcast start time t_0 can be used. Smart persistence is therefore based on an average over $t_0 - 15$ min to t_0 while the DNI reference values for t_0 are averages over $t_0 - 7.5$ min to $t_0 + 7.5$ min.

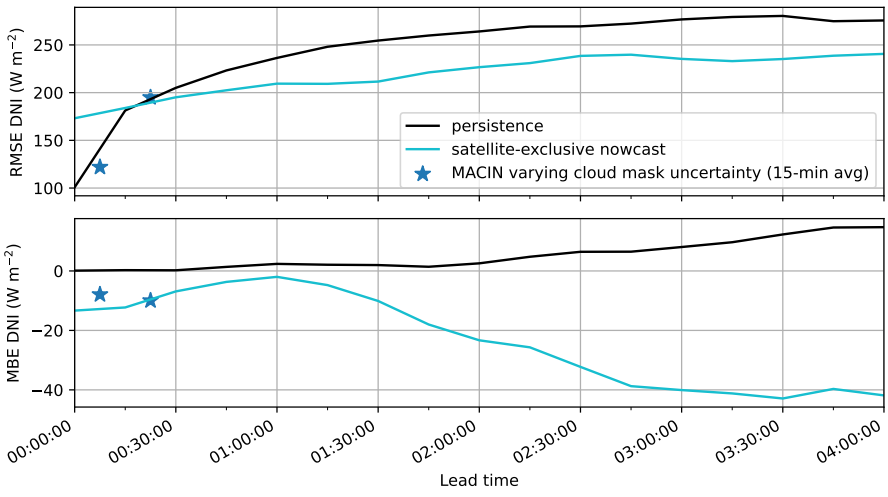

Figure 4.13: RMSE and MBE per lead time for 2019 nowcasts performed with the satellite-based irradiance nowcasting model. Smart persistence is given as a reference. Further on, errors for 15 min averages of 2040 MACIN nowcasts are indicated (averaged from 0 min to 14 min and from 15 min to 29 min).

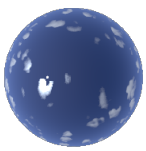

RMSE and MBE of satellite-based nowcasts are given per lead time in Fig. 4.13. For lead times of 30 min and more, satellite-based nowcasts outperform smart persistence in terms of RMSE. The largest RMSE improvement is approximately 45 Wm^{-2} or 17% for lead time 1 h 30 min and 3 h 15 min. Smart persistence RMSE is lower than satellite-based nowcast RMSE for lead times up to 30 min. This is analogously to errors of MACIN nowcasts discussed in Sect. 4.1.2 and 4.2. The initial cloud state is subject to errors in the complex satellite-based nowcasting model, while the smart persistence relies directly on a very good estimate from measurements. For longer lead times, changes to the initial state become more important and the possibility of detection of upcoming changes in satellite images leads to smaller errors compared to the smart persistence which cannot predict upcoming changes. MBE of satellite-based nowcasts is found to be negative up to $-43\,\mathrm{Wm}^{-2}$. The structure of MBE for exclusively satellite-based nowcasts resembles the MBE structure found for MACIN nowcasts but on longer timescales. Semi-large negative values in the beginning are followed my values close to zero and a negative trend for lead times larger than 1 h. As exclusively satellite-based nowcasts are only a minor part of this work, detailed investigation of error sources is omitted. Some potential error sources can, however, be named. As in MACIN, cloud evolution is modeled purely by advection in the satellite-based nowcasting model. This is a rough approximation, as complex cloud evolution on microscale, mesoscale and synoptic-scale can be relevant in the time frame of hour-ahead nowcasts. Also, the kilometer-scale resolution of MSG images limits the quality of satellite-based nowcasts. Vertical cloud mapping and according parallax correction are potentially large error sources as well.

Figure 4.13 also displays errors of MACIN nowcasts averaged over 15 min intervals as a reference. Two main messages can be derived by the comparison of these nowcasts with the satellite-based nowcasts. Firstly, ASI-based nowcasts significantly outperform satellite-based nowcasts in the first minutes, therefore justifying the additional effort of on-site measurements. Additionally, RMSE of ASI-based nowcasts is even larger than RMSE of satellite-based nowcasts for lead times on the order of about 20 min to 30 min. This similar performance indicates that the satellite images contain valuable information for nowcasting on these timescales. It further motivates the combined ASI- and satellite-based nowcasting model MACIN-S, which is evaluated in Sect. 4.4.

The configuration of a satellite-based irradiance nowcasting model presented here uses smoothed cloud layers τ_{low} and τ_{up} computed using thresholds, gaussian smoothed velocity field and 15 time subsamples averaged per nowcast step. Nowcasts with additional configurations were evaluated to find the best configuration and potentially justify major adaptations to the original model proposed by Sirch et al. (2017). Therefore, also nowcasts with alternative configurations of the satellite-based model were evaluated to investigate the effect of the most significant changes introduced compared to Sirch et al. (2017). Nowcasts were run for a total of 4 alternative model configurations, each differing in only one aspect from the configuration used in Sect. 3.5. The resulting RMSE and MBE over lead time is shown in Fig. 4.14 These are configurations with

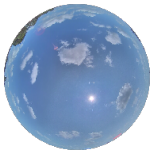

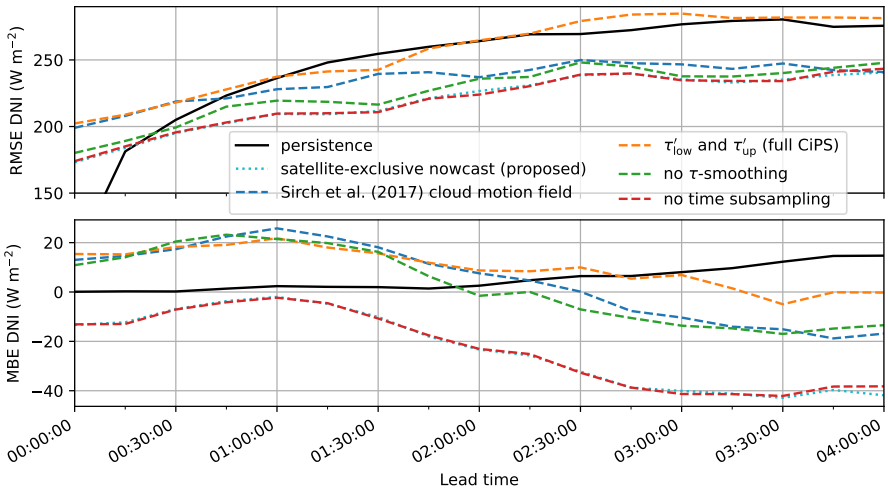

Figure 4.14: RMSE and MBE of 2019 nowcasts in July 2021 performed with four alternative configurations of the satellite-based nowcast model. Errors of nowcasts with the proposed configuration of the satellite-based nowcast model and smart persistence are given as a reference.

- velocity field interpolation according to Sirch et al. (2017) instead of the gaussian-based smoothing described in Sect. 3.5.1,
- cloud layers τ'_{low} and τ'_{up} computed according to extended CiPS information as described in Sect. 3.2.3 instead of the threshold-based cloud layers τ_{low} and τ_{up} respectively,
- cloud layers τ_{low} and τ_{up} not smoothed before advection as described in Sect. 3.5.1,
- or without the additional time subsampling explained in Sect. 3.5.2.

The nowcast performance of these configurations is briefly discussed in the following and reasons for errors are proposed but were not investigated in detail. If not stated otherwise, the errors of the proposed configuration of the exclusively satellite-based model are used as a reference. The configuration with cloud motion interpolation according to Sirch et al. (2017) shows significantly larger RMSE in the beginning, which gets closer to RMSE of the proposed configurations towards the maximum lead time of 4 h. MBE for this alternative configuration is positive up to 26 W m^{-2} in the beginning and slowly decreasing after 1h. This difference in MBE compared to the proposed configuration resembles the differences observed in RMSE and could potentially be the explanation for larger errors performance. One possible reason for the tendency towards positive MBE could be the underestimation of velocities in cloud-free regions by the Sirch et al. (2017) motion field construction. At nowcast start time, cloud optical depth fields are not yet advected and are identical to the proposed configuration. The differences in MBE despite equal cloud optical depth fields can be explained by the performed time subsampling to compute 15 min DNI averages.

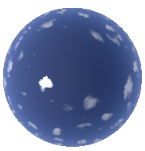

This subsampling makes use of the velocity field and can explain MBE differences at lead time 0 min for nowcasts with the Sirch et al. (2017) cloud motion field configuration.

The nowcast model configuration with cloud layers τ'_{low} and τ'_{up} shows larger RMSE and a positively shifted MBE curve. A comparison of the cloud optical depth layers τ_{low} and τ_{up} used in the proposed configuration as well as τ'_{low} and τ'_{up} is shown in Fig. 3.10. τ'_{low} exhibits cloud gaps in areas where τ_{low} shows compact cloud structures. This indicates that the additional information of CiPS is not ideally harmonized with the definition of water and ice clouds of APICS, at least for the configuration used in this work. The gaps in cloud optical depth could explain also the positive shift in MBE.

A smoothing of the cloud optical depth fields was introduced to suppress the minimal noise from CiPS retrieval, which is working on single pixels. In reality, neighboring MSG pixels are correlated and cannot be perfectly separated (Schmetz et al., 2002). RMSE is larger for nowcasts with the configuration without this cloud optical depth smoothing, suggesting that the smoothing is helpful for better representation of cloud optical depths. An extensive study on the type and extent of smoothing is omitted here, but could lead to further nowcast improvements.

The fourth alternative configuration omits the time subsampling. RMSE and MBE for nowcasts with this configuration differ only slightly compared to the proposed configuration. This shows that the time subsampling is not as important as the other adaptations as it is currently implemented. The large spatial extent of MSG pixels results in an implicit smoothing in time, which can explain why there is no improvement by the subsampling. For long lead times, errors in the cloud motion field as well as neglected cloud evolution dominate. Time subsampling is not helpful, if the advected cloud optical depth fields have limited quality for large lead times.

The development of an exclusively satellite-based nowcasting model was not a central part of this work and its performance may not be competitive with other scientific and commercial satellite-based models.

4.4 Combined all-sky imager and satellite-based nowcast performance

MACIN was designed as an irradiance nowcasting model, which can make use of multiple cloud information sources. Section 3.6 explains the method to use information derived from satellite measurements within MACIN. This extended MACIN-S was used to perform and evaluate DNI nowcasts as described in the following. The nowcast performance of MACIN-S with satellite information is evaluated on data in July 2021 for the PV plant in Egling a.d. Paar. Nowcasts were performed for the same time and location as nowcasts of MACIN without satellite data, as evaluated in Sect. 4.2. Note that only 21 out of the 2040 nowcasts are performed without satellite information. Nowcasts were performed with

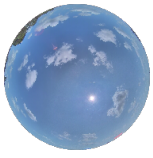

two MACIN-S configurations that differ only in the used cloud mask uncertainty. One configuration assumes constant cloud mask uncertainty (cf. Sect. 3.4.5), while the second configuration uses varying cloud mask uncertainty.

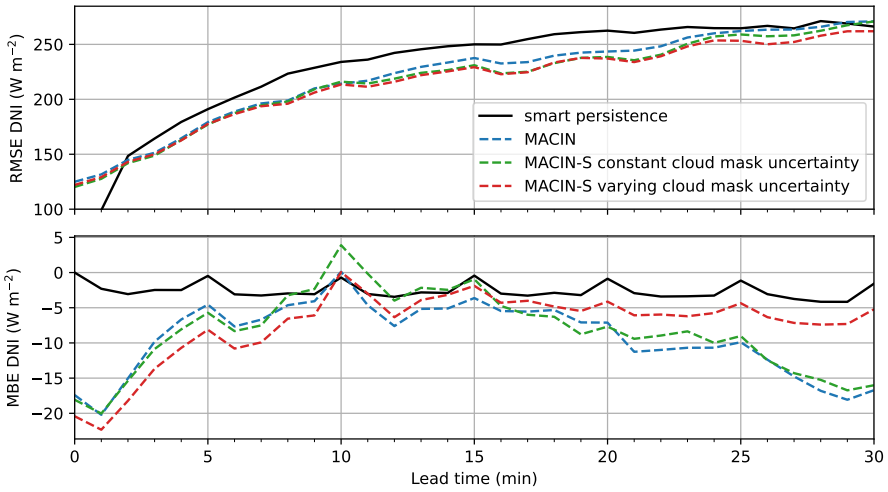

Figure 4.15: RMSE and MBE per lead time for 2040 MACIN-S DNI nowcasts in July 2021. Performance of MACIN with constant cloud mask uncertainty and smart persistence is given as a reference.

RMSE and MBE per lead time are computed for MACIN-S nowcasts and given in Fig. 4.15 along with error values for smart persistence. Additionally, error values for MACIN with varying cloud mask uncertainty but without satellite data is provided as a reference for ASI-based nowcasting without satellite information. The comparison in the following focuses on the difference between MACIN-S and MACIN to investigate possible benefits due to satellite measurements. Smart persistence is mainly given for completeness. RMSE of MACIN-S and MACIN nowcasts differs only marginally up to a lead time of 10 min. For longer lead times, the MACIN-S nowcasts show improvements in RMSE over MACIN in the range of approximately $8\,\mathrm{Wm}^{-2}$. Nowcasts for both MACIN-S configurations perform similar, with marginal differences up to lead times of about 23 min. For longer lead times, systematically lower RMSE is found for nowcasts of MACIN-S with varying cloud mask uncertainty compared to MACIN-S with constant cloud mask uncertainty. MBE of nowcasts for both MACIN-S configurations, and the MACIN reference, are structurally similar up to lead times of about 17 min with MBE differences in the range of $2\,\mathrm{Wm}^{-2}$ to $4\,\mathrm{Wm}^{-2}$. For larger lead times, MACIN-S nowcasts with constant cloud mask uncertainty show a tendency of increasing negative bias as observed for MACIN nowcasts. In contrast, MBE of MACIN-S nowcasts with varying cloud mask uncertainty is found to be in the range of $0\,\mathrm{Wm}^{-2}$ to $-5\,\mathrm{Wm}^{-2}$ for these larger lead times. For completeness, it shall also be mentioned that the RMSE of 15 min averaged MACIN-S nowcasts shows improvements over MACIN. It also fits well with the RMSE of the exclusively satellite-based nowcasts for lead times of more than 15 min as shown in Fig. 4.16. This could be expected, as the satellite observations help to estimate boundary information in MACIN-S, leading

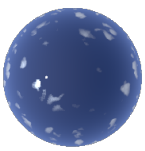

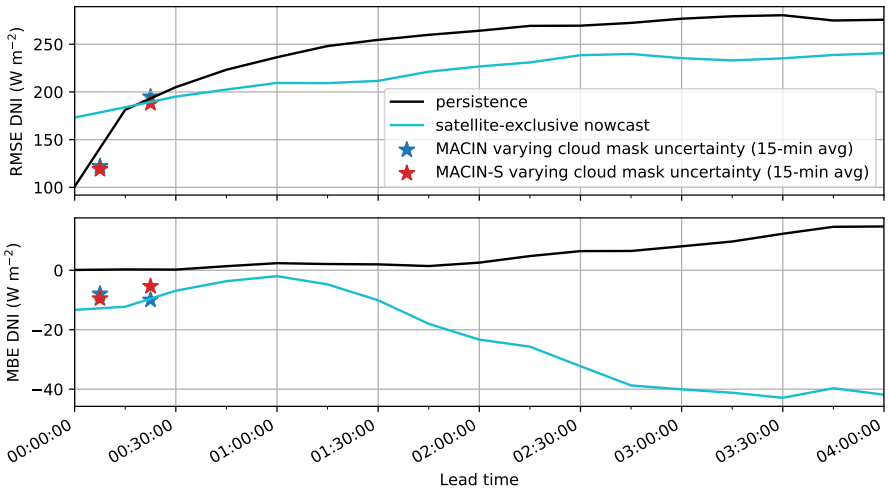

Figure 4.16: RMSE and MBE per lead time for 2019 nowcasts performed with the satellite-based irradiance nowcasting model. Smart persistence is given as a reference. Further on, errors for 15 min averages of 2040 MACIN and MACIN-S nowcasts are indicated (averaged from 0 min to 14 min and from 15 min to 29 min.

to a smooth transition between ASI- and satellite-based nowcasts.

Figure 4.17 shows the RMSE of the MACIN-S nowcasts grouped by cloud fraction, as discussed for MACIN in Sect. 4.2.2. The large RMSE of MACIN nowcasts for cloud fractions smaller than 0.2 and lead times of more than 15 min, is decreased for MACIN-S. The MACIN-S configuration with varying cloud mask uncertainty even matches the RMSE of persistence in these cases. This implies that satellite imagery provides reasonable information for distant clouds, which helps to improve the cloud representation in the model state. For situations with cloud fractions of more than 0.6 (Fig. 4.17d and e and large lead times of 15min, the nowcasts of MACIN with constant cloud mask uncertainty show a lower RMSE than all other benchmarked nowcasts. This configuration also shows the largest overestimation of cloudiness and the largest negative MBE for these lead times, which may be connected to smaller RMSE for larger cloud fractions.

Overall, the additional use of satellite data in MACIN proved beneficial for nowcasts, RMSE can be reduced especially for lead times larger than 10 min and situations of low cloud fraction. Information from the border of the ASI field of view becomes more important for larger lead times. This is extrapolated by nearest neighbor interpolation within MACIN. This extrapolation introduces a negative bias in nowcasted irradiances. The additional consideration of satellite data in the assimilation-inspired procedure provides cloud information for longer lead times. Especially the MACIN-S configuration with varying cloud mask uncertainty demonstrates the benefits of additional satellite measurements. Due to the assumed larger uncertainty of ASI cloud masks for larger viewing zenith angles, relative importance of satellite measurements gradually increases towards the border of ASI field of view. This can be seen as a confirmation of the proposed varying cloud mask

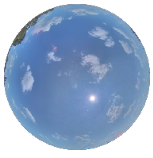

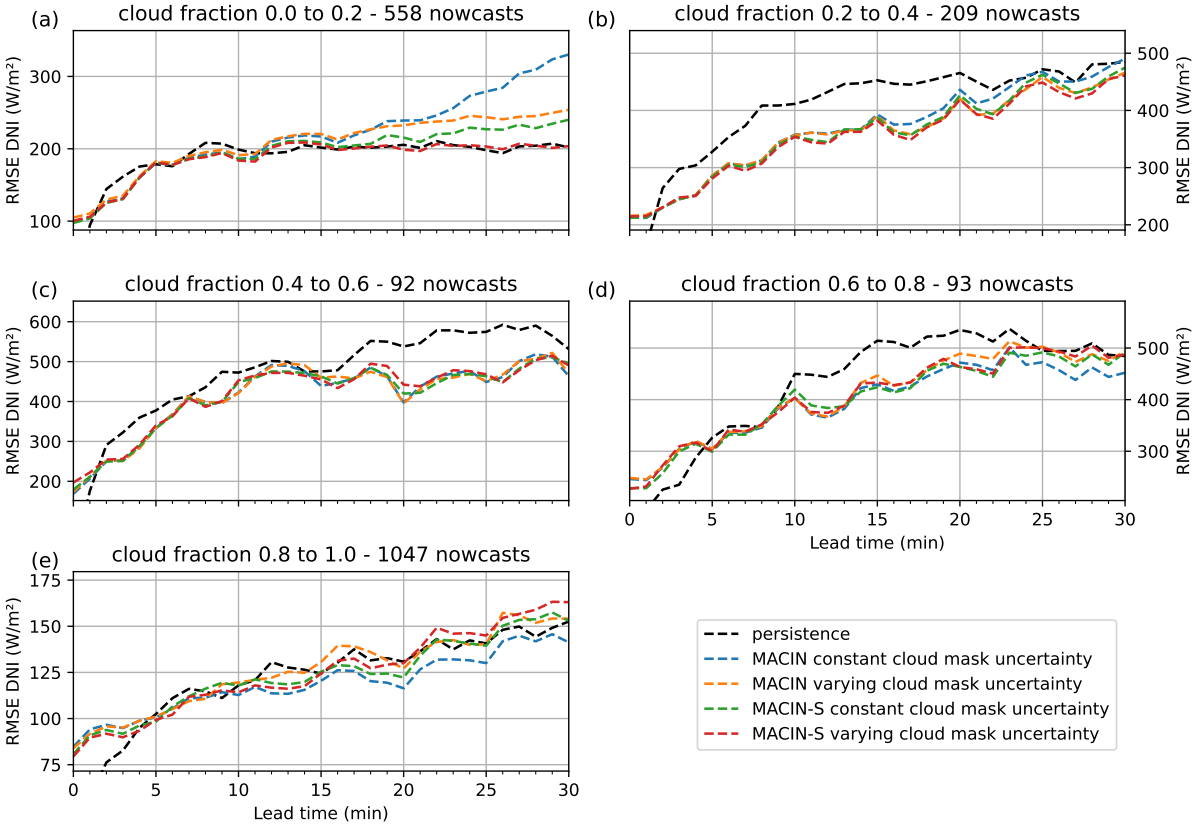

Figure 4.17: RMSE per lead time of 2040 MACIN and MACIN-S real-world nowcasts grouped by cloud fraction at nowcast start time. The cloud fraction bin and the number of nowcasts per bin are given in the header of the respective panel. Note the differences in scaling of the Y-axes.

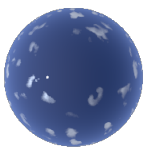

uncertainty. In the case of constant cloud mask uncertainty, the relative importance of satellite measurements is only increased for model grid points not covered by projected ASI images. The tendency for negative MBE for large lead times can be found also with satellite data in this case. An investigation of RMSE depending on cloud fraction, suggest that this negative MBE may actually contribute to slightly improved nowcast performance in case of large cloud fraction. More detailed assessments of the uncertainties of cloud masks and satellite contributions, as well as their spatial distribution, could give further insights and additional enhancements. Due to the limited extent of this work, this was not addressed here and remains for future work.

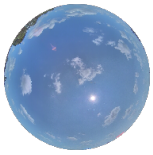

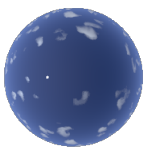

Chapter 5

Conclusion and Outlook

5.1 Conclusion

This work introduced MACIN, a novel model for all-sky image based cloud and direct irradiance nowcasting. MACIN is designed for intra-hour nowcasts up to lead times of approximately 30 min and with a time resolution of 1 min. It evaluates cloud images from two and possibly also more all-sky imagers (ASIs) to derive cloud masks with a convolutional neural network (CNN), cloud-base height (CBH) by stereography and cloud motion from consecutive images. These cloud observations are combined into a MACIN model state using a technique inspired by 4D-Var data assimilation (Le Dimet and Talagrand, 1986). The model state is extrapolated to the future using an advection scheme. Predicted cloudiness is converted into DNI by a radiative transfer (RT) parameterization, which exploits previous on-site measurements of DNI for an occluded and non-occluded Sun. The assimilation technique allows for the easy integration of additional observations for improved nowcasts. The extension of the nowcasting model by satellite data to MACIN-S demonstrates this capability.

A synthetic setup was developed for the extensive validation of MACIN, which was also published in Gregor et al. (2023). A method was developed to rapidly generate synthetic ASI images of Large eddy simulation (LES) cloud fields. Reference irradiance, CBH and motion as well as perfect cloud masks are derived for these LES cloud fields to validate MACIN in detail. Overall, the derived cloud information is very reliable with more than 94% pixel accuracy of cloud masks, 4.0% relative RMSE of CBH and RMSE of cloud motion in the order of $\pm 0.1\,\mathrm{m\,s^{-1}}$. MACIN DNI nowcasts outperform smart persistence for lead times of 1 min and more in terms of RMSE in the synthetic setup, proving MACIN to work. Multiple different nowcast experiments were conducted for detailed analysis of nowcast errors, e.g., with perfect cloud masks or shifting frozen cloud fields. This also extends the work of Gregor et al. (2023) and broadens the understanding of nowcasting errors. The initial large MACIN nowcast RMSE could be attributed mainly to imperfect cloud masks in the region of the Sun and to the RT parameterization. The strong increase in RMSE over lead time could be attributed to cloud evolution. MACIN models only the displacement of clouds, as other ASI-based irradiance models in the literature (e.g., Schmidt et al., 2016; Nouri et al., 2022). These models currently do not capture full cloud evolution with growth, decay, and reshaping. ASIs view distant clouds under large zenith angles and the vertical cloud extent is often misinterpreted as horizontal extent

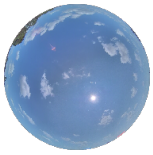

in images. Overestimation of the cloudiness of distant regions leads to a negative bias in the nowcasted DNI. Finally, the synthetic setup allows for validating nowcasts for areas directly. While real-world irradiance measurements are point measurements and area irradiance is usually not measurable directly, the synthetic setup offers the possibility of perfect area DNI references. As previous studies (Kuhn et al., 2017b; Nouri et al., 2022) suggested, the nowcast performance can be greatly improved when spatially averaged irradiances are nowcasted.

MACIN was also run with real world ASI images to evaluate DNI nowcast performance for real cloud situations. A total of 2040 nowcasts was performed for July 2021. The nowcast errors found agree well with the findings of the synthetic setup, but the improvement over the persistence of MACIN nowcasts is generally greater for real data. This was attributed to additional challenges due to imperfect ASI images and more complex cloud situations, e.g. with multiple layers. In addition, the distribution of cloud fractions differs strongly between the real data and synthetic data. Note that the real ASI images were intentionally not filtered and quality-controlled to simulate an operational use case. In conclusion, MACIN outperforms smart persistence for synthetic and real-world data.

The Meteosat second generation (MSG) and other similar geostationary satellites provide spectral cloud images with large spatial coverage. This work describes how these images can be used for DNI nowcasting. At first, a method was introduced to derive DNI from MSG images. Following Sirch et al. (2017) and using the cloud optical depth retrievals CiPS (Strandgren et al., 2017) and APICS (Bugliaro et al., 2011), two cloud layers with optical depth are derived from images. For a given ground position, the relevant cloud optical depths can be extracted from these layers to compute DNI. A satellite-based DNI nowcasting model based on these methods was described and evaluated. This illustrates the potential benefit of MSG images for irradiance nowcasting applications and validates the method to derive DNI. The method of deriving DNI from MSG images was also exploited for the main intended use in this work: an extension of MACIN. MACIN was extended to make use of MSG images in addition to ASI images. Satellite-derived DNI fields are converted into a cloudiness state, which is assimilated in the extended MACIN-S together with cloud information from ASI images. Again, 2040 DNI nowcasts were run with MACIN-S for July 2021. For lead times of more than 10 min, MACIN-S nowcasts outperform MACIN nowcasts with an RMSE reduction of approximately 8 W m^{-2} and with improved MBE for lead times of 20 min and more. Overall, this illustrates the potential of using the assimilation technique to combine ASI and MSG images for improved minute-ahead DNI nowcasting.

In summary, the key points of this work are:

- A novel model for all-sky image based cloud and direct irradiance nowcasting (MACIN) was introduced along with an extended model (MACIN-S), which makes additional use of MSG images.
- MACIN was successfully validated in a synthetic setup with extended error investi-

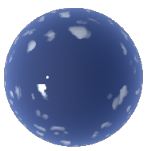

gation and evaluated on real-world data.

- The combined ASI- and satellite-based nowcasts from MACIN-S showed further performance improvements over nowcasts from MACIN.

The main part of this work focuses on the nowcasting of direct irradiance, but PV power usually depends on global irradiance. Therefore, Sect. 5.2 gives an extended outlook on GHI and PV power nowcasting based on MACIN-S and demonstrates the potential of the nowcasting model for actual applications.

MACIN was developed within a subproject of the NETFLEX project. Its irradiance nowcasts were designed for use in the minute-scale management of a biogas power plant. The processing of irradiance nowcasts and management of the biogas power plant were developed in another subproject not addressed by this work. While MACIN is able to compute DNI nowcasts operationally within one minute, he computational times of the PV power plant model developed in another NETFLEX subproject contrasted with the desired minute-scale management of the power plant. Additionally, knowledge of the state of degradation and the details of the PV plant was limited. Therefore, the MACIN nowcasts were only used as a minor contribution and the focus was shifted more to economic and engineering aspects for the management of the biogas plant. However, knowledge of upcoming irradiance and PV power fluctuations were provided the biogas management as well and potential for optimized management of the plant was found. The developed irradiance nowcasting models can be used in other applications beyond biogas power plants as well. Optimized charging or discharging of large battery storage and the management of island grids with diesel generators and PV are two possible use cases.

Remaining challenges and possible future work

While MACIN and MACIN-S were successfully validated, the improvement over smart persistence is still relatively small and nowcast errors need to be reduced. Investigating the source of errors revealed possible starting points. An improved representation of cloud evolution could drastically improve nowcast performance. Physical cloud evolution is challenging to model based only on ASI images and, e.g., LES models come with large computational cost, which may even rule out the use for minute-ahead nowcasting. In the related field of radar-based precipitation nowcasting, statistical and machine learning-based cloud modeling approaches are already becoming more and more popular, as they can potentially approximate not only a shift of clouds, but also growth, decay, and reshaping (e.g. Pulkkinen et al., 2019; Ayzel et al., 2020; Ravuri et al., 2021) from a series of two-dimensional images. Carpentieri et al. (2023) already applied one of the statistical approaches for satellite-based irradiance nowcasting. Some of these more advanced cloud modeling methods also provide probabilistic nowcasts, another potentially interesting idea for MACIN. Not only deterministic irradiances are predicted but also probabilities or a range of irradiances, e.g. by an ensemble of nowcasts. In numerical weather prediction,

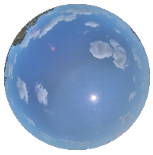

ensemble predictions are commonly used. Each member of the ensemble starts from a different initial state. Therefore, data assimilation techniques such as the Ensemble Kalman Filter (see e.g. Pu and Kalnay, 2019) can be used and could potentially be adapted for use within MACIN. It should also be mentioned here that this work focused on classical ASI-based irradiance nowcast models like MACIN. These models extract cloud information from images, plug this into a simple numerical model to extrapolate future cloud states and convert future cloud information into irradiance with an RT parameterization (Peng et al., 2015; Schmidt et al., 2016; Dittmann et al., 2021; Richardson et al., 2019; Nouri et al., 2022). Recently, more and more machine learning models have been proposed, which use ASI images and measured irradiance as input to, e.g. a CNN and output irradiance nowcasts potentially without intermediate steps (e.g.; Paletta et al., 2022; Song et al., 2022).Currently, these models show performance comparable to models based on the classical approach (Logothetis et al., 2022).

The RT parameterization of MACIN was identified as an additional source of significant errors. Nouri et al. (2019b) proposes another way of determining relevant cloud optical depth than currently used in MACIN, which could be adapted. Situations with multiple cloud layers often come with different cloud optical properties per level. A representation of more than one cloud layer in MACIN and the respective extensions to the RT parameterization could significantly improve estimated DNI. In addition to multiple cloud layers, also a vertical extent per cloud layer could be introduced in MACIN. This may help to reduce the overestimation of the cloud fraction for distant clouds. In case of multiple cloud layers, images provide only information for upper layers if there is no cloud in line of sight of the ASIs on a lower layer. The initial state of the upper layer would in such cases be partially undefined. In case of broken clouds in lower layers, the use of a data assimilation background field in MACIN can provide additional information. Parts of the upper layer which are currently out of sight, may have been visible at the previous nowcast start. This background information can be used to find a reasonable analysis state even in regions without current observations. Additionally, a background field can help in case of no images. In case of, e.g., problems with all ASIs, the cloud information of a previous nowcast run can be used. The use of a background field was omitted in this work, as the oversimplified advection scheme leads to limited quality of predicted cloudiness fields for lead times on the order of 5 min and more. The errors of the background fields are currently too large for beneficial use. However, a better model for cloud evolution could make the improved predicted cloudiness attractive as a background state. In theory, MACIN can directly make use of more than two ASI by considering additional observations in the cost function. For example, a dense network of ASIs could improve nowcast performance due to the better estimation of relevant cloud cross sections. Also other types of ground-based imagers, e.g., infrared cameras can be used to potentially improve nowcasts.

A major drawback of MSG satellite images is the comparably low resolution on the order of 3 km for the sub-satellite point and even more elsewhere. In December 2022, the first Meteosat third generation geostationary satellite was launched and is planned to become operationally available around the end of 2023. The flexible combined imager onboard this

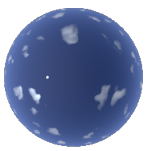

next-generation satellite will provide images with 16 spectral channels at a spatial sampling distance of 1 km for the sub-satellite point. Moreover, the image frequency will be reduced compared to MSG. This higher resolution satellite imagery can enable a leap forward in satellite- and MACIN-S-based nowcasting performance. In theory, MACIN could also be used as a satellite-based nowcasting model without ASI images. While this

LASCAT, the method developed for fast generation of synthetic images of modeled cloud scenes was not validated within this work. Future studies could validate the radiance computed with this model and investigate its ability to approximate 3D radiative transfer. Investigation of possible further enhancements is conceivable in this context, e.g. improved estimation of angular distribution of diffuse radiation.

Isolated use of MACIN demonstrated the performance of the DNI and PV nowcasts. However, even perfect nowcasts are useless if not used for a beneficial application. Therefore, it is highly desirable to evaluate the potential of MACIN for specific applications.

5.2 Outlook on global irradiance and photovoltaic power nowcasting

The nowcasts presented in the previous chapters focused on DNI. For actual use with PV power plants, nowcasts of global irradiance in plane of array (POA) are required. Ideally, even a PV power nowcast is provided to the power plant or grid operator. This section explains the necessary further steps to calculate PV power nowcasts from DNI nowcasts and demonstrates the performance of PV power nowcasts derived with simple further steps. Section 5.2.1 describes the extension to nowcasts for global horizontal irradiance and the resulting nowcast performance. The final setup and performance of the PV power nowcasts are given in Sect. 5.2.2.

5.2.1 Global horizontal irradiance nowcasts

Global irradiance on a horizontal plane was measured on the PV plant in Egling a.d. Paar with an Eko MS-80 pyranometer (cf. Sect. 3.2.2). GHI nowcasts can be seen as a first step towards PV power nowcasts and are explained in the following. Global horizontal irradiance is the sum of direct and diffuse contributions as

$$\mathrm{GHI} = \mathrm{DHI} + \mathrm{DNI}\ \cos\theta_{\mathrm{sun}} \tag{5.1}$$

where DNI is converted onto a horizontal plan by accounting for the sun zenith angle θ_{sun} (see also Sect. 2.1.1). For GHI nowcasts, DNI nowcasted by MACIN-S can be used, and additional DHI nowcasts are required. Diffuse irradiance usually varies less than direct irradiance and depends on complex 3D RT. Smart persistence is therefore commonly used

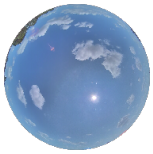

to nowcast diffuse irradiance (e.g.; Nouri et al., 2018). Analogously to smart persistence for DNI (Eq. 3.35), smart persistence DHI nowcasts for time t can be computed by

$$\mathrm{DHI}_{\mathrm{pers}}(t) = k_{\mathrm{DHI}}(t_0) \cdot \mathrm{DHI}_{\mathrm{cs}}(t) \tag{5.2}$$

based on the diffuse clear-sky index

$$k_{\mathrm{DHI}} = \frac{\mathrm{DHI}_{\mathrm{meas}}}{\mathrm{DHI}_{\mathrm{cs}}} \tag{5.3}$$

for the nowcast start time t_0. In this work, the exponentially weighted mean with a half-width time of 10 min is used to determine $k_{\mathrm{DHI}}(t_0)$ from a series of clear-sky indices. This averaged $k_{\mathrm{DHI}}(t_0)$ is desired since $\mathrm{DHI}_{\mathrm{meas}}$ is a point measurement and intended to be used to compute the PV power, which depends on large area irradiance. Here, the spatial coverage and averaging of irradiance by the PV plant is reflected by a temporal average of the diffuse irradiance.

The nowcasted GHI value for time t can then be formulated as

$$\mathrm{GHI}_{\mathrm{MACIN\text{-}S}}(t) = \mathrm{DHI}_{\mathrm{pers}}(t) + \mathrm{DNI}_{\mathrm{MACIN\text{-}S}}(t) \tag{5.4}$$

where the MACIN-S configuration with varying cloud mask uncertainty was chosen to compute DNI because of its improved performance (cf. Sect. 4). GHI smart persistence was calculated additionally as a combination of smart persistence of DHI and DNI according to Eq. 5.1.

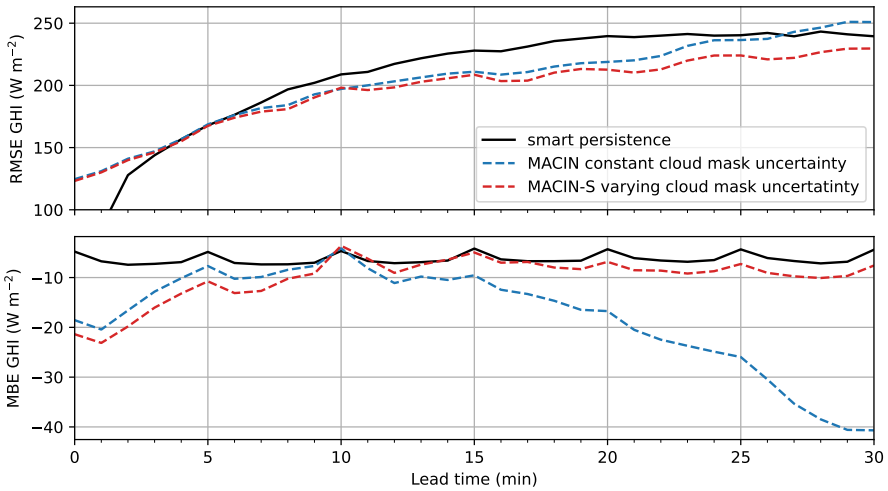

Figure 5.1: RMSE and MBE per lead time for 2040 GHI nowcasts based on MACIN and MACIN-S. Errors for smart persistence are given as a reference.

Figure 5.1 shows the results of GHI nowcasts with smart persistence and MACIN-S as well as MACIN. The structure and systematic resemble DNI nowcasts and are therefore

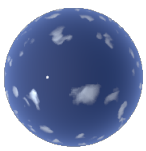

not discussed here in detail. MACIN-S nowcasts give a lower RMSE than smart persistence for lead times greater than 5 min. As for DNI nowcasts, MACIN-S is able to outperform MACIN. In conclusion, the developed ASI-based DNI nowcasting model can be extended to nowcast GHI for improved performance over smart persistence.

5.2.2 Photovoltaic power nowcasts

PV power plants convert incident radiation on PV panels into electrical power. The key factors for the magnitude of electrical power are the incoming radiative power (irradiance) and the PV panel temperature. PV panel efficiency decreases with increasing temperature Mavromatakis et al. (e.g.; 2014). Accurate PV power plant models need to consider not only these two variables, but also the wiring of panels, regulation of inverters, spectral response and pollution of PV panels, degradation of components and cables, as well as operational constraints like a maximum allowed power production. This section addresses PV power nowcasts based on irradiance nowcasts and is intended as a demonstration of possible benefits. As PV power models are not the focus of this work, a simple statistical PV model is described and used to illustrate the performance of the PV power nowcast.

Plane of array irradiances

The PV panels of the power plant in Egling a.d. Paar are installed in lines from east to west and facing south with a tilt. For PV power applications, measured and predicted irradiances should be given for this plane of array (POA) orientation. The orientation of direct normal irradiance depends on time and can be described by a vector in the direction of the Sun $\vec{r}_{\mathrm{DNI}}(\theta_{\mathrm{sun}}, \phi_{\mathrm{sun}})$ in spherical coordinates with the zenith angle θ_{sun} and the azimuth angle ϕ_{sun} under which the Sun is observed for a given time. Parallel to this, a panel normal vector $\vec{r}_{\mathrm{panel}}(\theta_{\mathrm{panel}}, \phi_{\mathrm{panel}})$ with zenith $\theta_{\mathrm{panel}} = 30°$ and azimuth angle $\phi_{\mathrm{panel}} = 180°$ for the PV power plant in Egling a.d. Paar. The angle between these two vectors θ_{inc} describes the difference in orientation between the DNI plane and POA and therefore the relative angle of incidence. It can be derived using the dot product between the normal vectors as

$$\cos\theta_{\mathrm{inc}} = \frac{\vec{r}_{\mathrm{DNI}} \cdot \vec{r}_{\mathrm{panel}}}{||\vec{r}_{\mathrm{DNI}}||\,||\vec{r}_{\mathrm{panel}}||}. \tag{5.5}$$

DNI is converted into direct plane of array irradiance by

$$E_{\mathrm{dir,POA}} = \max\left(0, \mathrm{DNI}\,\cos\theta_{\mathrm{inc}}\right). \tag{5.6}$$

On the contrary, the measured DHI has no single direction, but is composed of diffuse radiances from potentially all angles. The conversion of DHI into POA strongly depends on the distribution of these radiances. Efforts have been made to approximate typical angle distributions for given atmospheric conditions (e.g.; Kuchler, 1979; Perez et al., 1988; Hay,

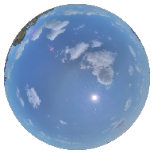

1993) and formulate parameterization for the conversion from DHI to diffuse POA irradiance. To keep things simple, a very basic approximation was chosen for this work. Diffuse irradiance is assumed to be isotropic; i.e., diffuse radiance is assumed to be independent of angles. For DHI, these are only radiances from the sky. The contribution of reflected light from the ground is not considered. The diffuse POA irradiance can be described following Hottel and Woertz (1942) as

$$E_{\mathrm{dif,POA}} = \mathrm{DHI}\,\frac{1+\cos\theta_{\mathrm{panel}}}{2} \tag{5.7}$$

which is DHI scaled by the fraction of sky seen for a panel with zenith angle θ_{panel}. Total plane of array irradiance can be calculated as

$$E_{\mathrm{tot,POA}} = E_{\mathrm{dir,POA}} + E_{\mathrm{dif,POA}}. \tag{5.8}$$

Note that the position of the Sun changes over time and therefore the relation between $E_{\mathrm{dir,POA}}$ and DNI changes over time. However, sun zenith and azimuth angle changes over 15 min are assumed to be small and time averaged $\overline{E}_{\mathrm{dir,POA}}$ is computed as the POA irradiance for time averaged DNI

$$\overline{E}_{\mathrm{dir,POA}} \approx \max\left(0, \overline{\mathrm{DNI}}\,\cos\overline{\theta}_{\mathrm{inc}}\right). \tag{5.9}$$

Photovoltaic power measurements

The PV power plant is monitored by the company GP JOULE GmbH which provided measurements of grid input PV power in 15 min intervals for years 2020 and 2021 as well as 1 min values for July 2021. Figure 5.2 gives an overview of the 15 min values. Data

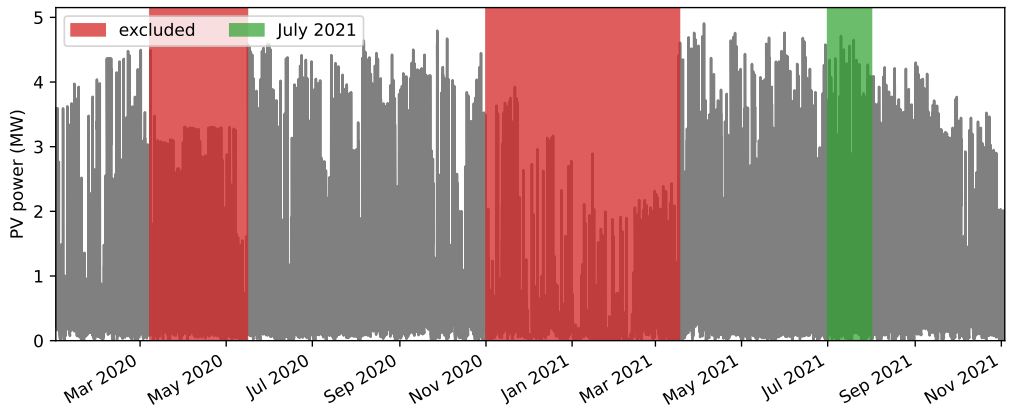

Figure 5.2: Available 15 min PV power measurements for the years 2020 and 2021. Highlighted regions indicated times excluded due to obvious malfunctions or limitations of the power plant and the evaluation month July 2021.

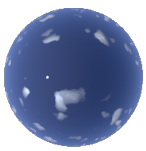

between 08 March 2020 and 16 May 2020 as well as between 01 November 2020 and 18 March 2021 were excluded due to obvious external limitation or partly malfunction of the PV power plant. The 15 min values are used to fit the PV model in the following and the 1 min values are used as a reference for PV power nowcasts in the following. According to personal communication with the owners of PV power plants, the maximum power input to the electric grid is limited to 5000 kW. PV power is an area quantity, while the available irradiance measurements give values for a single point. To partly compensate for this, the 15 min PV power and 15 min GHI mean are used to fit the PV model. The temporal averaging is assumed to represent the missing spatial coverage and the averaging of measured GHI. For 1 min PV power nowcasting, MACIN-S DNI nowcasts are derived for areas and DHI persistence is assumed to be valid for areas as well.

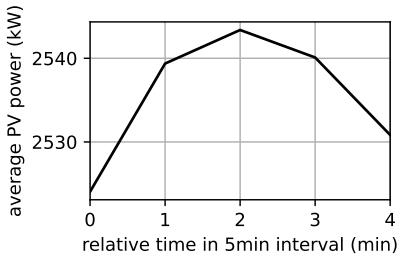

Figure 5.3: 1 min PV power production averaged per relative times within 5 min intervals for all times in the DNI nowcasts.

Averaging the 1 min PV power values per minute in 5 min intervals gives a structure similar to that described for the DNI equivalents in Sect. 4.2.2. As shown in Fig. 5.3, the average PV power is lower for minute 0 than for the other minutes. Although the CR6 datalogger recording irradiance measurements is not at the same location as the PV grid input measurement, both are in the same electric sub-grid of the PV power plant. The coincidence of this structure suggests that either the PV power input varies every fifth minute and influences the CR6 datalogger or the measurement of the PV power input and DNI both are influenced by variations in the electricity sub-grid.

Photovoltaic power plant model

For this study, the PV power plant in Egling a.d. Paar is modeled statistically. A linear regression is fitted to describe PV power as a function of $E_{\mathrm{tot,POA}}$ and air temperature T in K as an indicator for panel temperature. 15 min averages of PV power and POA irradiances are used. POA irradiances are calculated from the 15 min averages of the measured DHI and DNI. Air temperature measurements are available in 10 min intervals from the DWD weather station 06346 in Maisach-Galgen (48.2070°N, 11.2035°E) approximately 15 km east of the PV power plant. Data were restricted to times with measured PV power in the range of 0 kW to 5000 kW. These are interpolated to 15 min intervals as well. The resulting

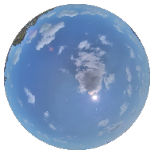

Table 5.1: Parameter values for the linear PV power model.

parameter	value	unit
a_0	-25.18600964	kW
a_1	4.70735819	$10^3\,\mathrm{m}^2$
a_2	0.16957067	$\mathrm{K}^{-1}\,\mathrm{kW}$

linear regression is

$$\mathcal{M}_{\mathrm{PV,raw}} = a_0 + a_1\, E_{\mathrm{tot,POA}} + a_2\, T \tag{5.10}$$

with the parameter values given in Tab. 5.1. Taking into account the allowed limits of PV power for the power plant in Egling a.d. Paar gives the PV power model

$$\mathcal{M}_{\mathrm{PV}} = \begin{cases} 0\,\mathrm{kW} & \text{if} \quad \mathcal{M}_{\mathrm{PV,raw}} < 0\,\mathrm{kW} \\ 5000\,\mathrm{kW} & \text{if} \quad \mathcal{M}_{\mathrm{PV,raw}} > 5000\,\mathrm{kW} \\ \mathcal{M}_{\mathrm{PV,raw}} & \text{else.} \end{cases} \tag{5.11}$$

RMSE of $\mathcal{M}_{\mathrm{PV}}$ PV power for the data used for fitting is 293 kW while the average measured PV power is 1333 kW. Note that a_2 is positive and therefore indicates increasing PV power for higher temperatures in this model. This is contrary to the previous statement about the theoretical relation of these quantities. The linear regression does not state anything about physical causality; temperature may also be used here as a only proxy variable, e.g., indicating diurnal and annual cycle of sun zenith angle. Given the latitude of the PV plant and the tilt of the panels, this can be expected to be positively correlated. This is one possible explanation for $a_2 > 0$. Further on, nowcasted irradiance is integrated over the solar spectrum. The spectral response of PV panels is not uniform in this wavelength range (e.g., Gouvêa et al., 2017), an enhanced physical model of the PV plant would need to take this into account.

Photovoltaic power nowcast performance

The MACIN-S irradiance nowcasts were performed as described in Sect. 4.4, but for an area that approximately covers the PV plant. Two squares 300 m × 300 m define this nowcast area, one with the lower right corner at ASI-16142 and one with the lower left corner 300 m north of this imager. MACIN-S DNI nowcasts were computed with 10 m resolution for these squares and spatially averaged. DHI was assumed to be spatially constant and smart persistence nowcasts based on localized measurements were assumed to be suitable. The nowcasted irradiances were converted into nowcasts of global POA irradiance and fed into the model of the PV power plant described above to compute 2040 PV power nowcasts for July 2021 with 1 min time resolution. PV power persistence serves as a reference and is calculated from 1 min PV power measurements at the nowcast start time. Note that the

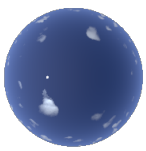

PV power persistence is not a smart persistence but gives a constant value over lead time in contrast to the smart persistence of DNI and DHI. Due to the lack of an exact PV model, the diurnal cycle of PV power for cloud-free conditions cannot be accurately modeled. For nowcast horizons of 30 min and nowcasts for times between 08:00:00 UTC and 15:00:00 UTC, the diurnal cycle is, however, a limited influence, and PV power persistence is still considered to be a relevant baseline nowcast for comparison.

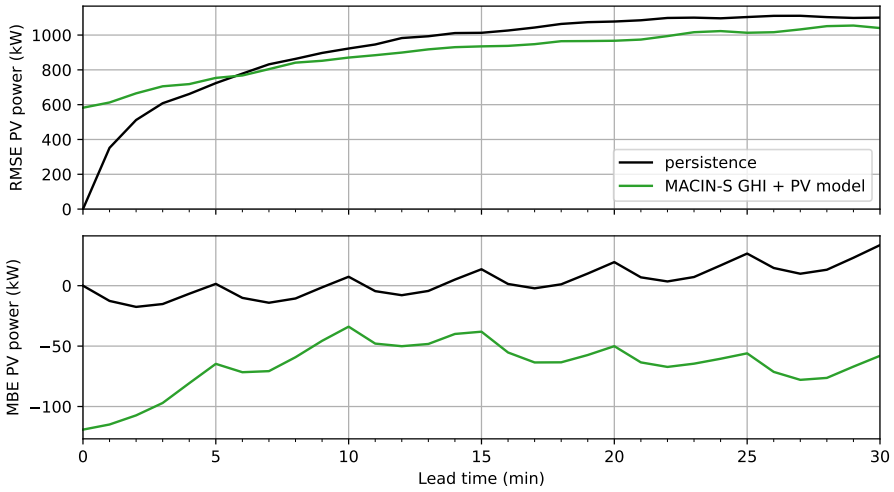

Figure 5.4: RMSE and MBE per lead time for 2040 PV power nowcasts in July 2021. Nowcasts are computed from PV power persistence, and MACIN-S-based irradiance nowcasts.

Figure 5.4 gives the resulting RMSE and MBE over lead time for PV power persistence and MACIN-S-based nowcasts. The RMSE of the PV power persistence is 0 kW at the beginning and increases up to about 1100 kW for lead times of 22 min and more. RMSE increases strongest for small lead times and levels out for longer lead times. MACIN-S-based nowcasts give RMSE of 574 kW for lead time 0 min with a steady increase up to about 982 kW for lead time 22 min and about 1027 kW for lead time 30 min. MACIN-S-based nowcasts give lower RMSE than PV persistence for lead times of more than 5 min. MBE of the persistence nowcasts is in the range of −20 kW to 40 kW with a positive trend for longer lead times. It exhibits a 5 min interval structure with most positive values for lead times which are multiples of 5 min. MBE of the nowcasts based on MACIN-S is constantly negative, starting at −105 kW with a positive trend towards −22 kW for lead time 10 min and a negative trend for even longer lead times up to −64 kW at lead time 27 min. The 5 min interval structure in MBE is also observable for MACIN-S-based nowcasts. Overall, the MBE structure MACIN-S-based PV power nowcasts resembles the structure found for the corresponding DNI nowcasts with an additional negative offset and stronger 5 min interval structure.

The RMSE improvements of the MACIN-S-based PV power nowcasts over the PV persistence nowcasts demonstrate the potential of MACIN-S for PV power applications. Due to the main focus of this work on DNI nowcasting, multiple components are implemented

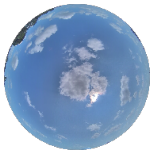

in simplified ways to calculate the PV power nowcasts based on these MACIN-S DNI nowcasts. The use of smart persistence for DHI, the simplified conversion of diffuse irradiance to POA, and the roughly approximated PV power plant model leave room for improvement. Therefore, the performance of the presented MACIN-S-based PV power nowcasts is a conservative estimate of the possible benefits achievable by using the MACIN-S DNI nowcasts as a basis for PV power nowcasts.

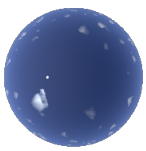

Bibliography

Achanta, R., Shaji, A., Smith, K., Lucchi, A., Fua, P., and Süsstrunk, S. (2012). SLIC Superpixels Compared to State-of-the-Art Superpixel Methods. *IEEE Transactions on Pattern Analysis and Machine Intelligence*, 34(11):2274–2282.

Anderson, G. P., Clough, S. A., Kneizys, F. X., Chetwynd, J. H., and Shettle, E. P. (1986). AFGL atmospheric constituent profiles (0–120 km). Technical Report 954, Air Force Geophysics Lab Hanscom AFB MA.

Andrews, D. G. (2000). Atmospheric radiation. In *An Introduction to Atmospheric Physics*, pages 55–96. Cambridge University Press.

Ayzel, G., Scheffer, T., and Heistermann, M. (2020). RainNet v1.0: A convolutional neural network for radar-based precipitation nowcasting. *Geoscientific Model Development*, 13(6):2631–2644.

Beekmans, C., Schneider, J., Läbe, T., Lennefer, M., Stachniss, C., and Simmer, C. (2016). Cloud photogrammetry with dense stereo for fisheye cameras. *Atmospheric Chemistry and Physics*, 16(22):14231–14248.

Blanco-Muriel, M., Alarcón-Padilla, D. C., López-Moratalla, T., and Lara-Coira, M. (2001). Computing the solar vector. *Solar Energy*, 70(5):431–441.

Blum, N. B., Nouri, B., Wilbert, S., Schmidt, T., Lünsdorf, O., Stührenberg, J., Heinemann, D., Kazantzidis, A., and Pitz-Paal, R. (2021). Cloud height measurement by a network of all-sky imagers. *Atmospheric Measurement Techniques*, 14(7):5199–5224.

Blum, N. B., Wilbert, S., Nouri, B., Stührenberg, J., Lezaca Galeano, J. E., Schmidt, T., Heinemann, D., Vogt, T., Kazantzidis, A., and Pitz-Paal, R. (2022). Analyzing Spatial Variations of Cloud Attenuation by a Network of All-Sky Imagers. *Remote Sensing*, 14(22):5685.

Bodhaine, B. A., Wood, N. B., Dutton, E. G., and Slusser, J. R. (1999). On Rayleigh Optical Depth Calculations. *Journal of Atmospheric and Oceanic Technology*, 16(11):1854–1861.

Boudreault, L.-É., Liandrat, O., Braun, A., Buessler, É., Lafuma, M., Cros, S., Gomez, A., Sas, R., and Delmas, J. (2018). Sky-Imager Forecasting for Improved Management of a Hybrid Photovoltaic-Diesel System. *3rd International Hybrid Power Systems Workshop*, (May):1–6.

Bradski, G. (2000). The OpenCV Library. *Dr. Dobb's Journal of Software Tools*.

Bugliaro, L., Zinner, T., Keil, C., Mayer, B., Hollmann, R., Reuter, M., and Thomas, W. (2011). Validation of cloud property retrievals with simulated satellite radiances: a case study for SEVIRI. *Atmospheric Chemistry and Physics*, 11(12):5603–5624.

Buras, R., Dowling, T., and Emde, C. (2011). New secondary-scattering correction in DISORT with increased efficiency for forward scattering. *Journal of Quantitative Spectroscopy and Radiative Transfer*, 112(12):2028–2034.

Carpentieri, A., Pulkkinen, S., Nerini, D., Folini, D., Wild, M., and Meyer, A. (2023). Intraday probabilistic forecasts of solar resources with cloud scale-dependent autoregressive advection.

Chandrasekhar, S. (1950). Radiative Transfer Clarendon Press.

Chen, L.-C., Zhu, Y., Papandreou, G., Schroff, F., and Adam, H. (2018). Encoder-Decoder with Atrous Separable Convolution for Semantic Image Segmentation. *Lecture Notes in Computer Science (including subseries Lecture Notes in Artificial Intelligence and Lecture Notes in Bioinformatics)*, 11211 LNCS:833–851.

Chen, X., Du, Y., Lim, E., Fang, L., and Yan, K. (2022). Towards the applicability of solar nowcasting: A practice on predictive PV power ramp-rate control. *Renewable Energy*, 195(June):147–166.

Chow, C. W., Urquhart, B., Lave, M., Dominguez, A., Kleissl, J., Shields, J., and Washom, B. (2011). Intra-hour forecasting with a total sky imager at the UC San Diego solar energy testbed. *Solar Energy*, 85(11):2881–2893.

Deuzé, J., Herman, M., and Santer, R. (1989). Fourier series expansion of the transfer equation in the atmosphere-ocean system. *Journal of Quantitative Spectroscopy and Radiative Transfer*, 41(6):483–494.

Dev, S., Manandhar, S., Lee, Y. H., and Winkler, S. (2019). Multi-label Cloud Segmentation Using a Deep Network. *2019 USNC-URSI Radio Science Meeting (Joint with AP-S Symposium), USNC-URSI 2019 - Proceedings*, pages 113–114.

Dittmann, A., Holland, N., and Lorenz, E. (2021). A new sky imager based global irradiance forecasting model with analyses of cirrus situations. *Meteorologische Zeitschrift*, 30(2):101–113.

Emde, C., Buras-Schnell, R., Kylling, A., Mayer, B., Gasteiger, J., Hamann, U., Kylling, J., Richter, B., Pause, C., Dowling, T., and Bugliaro, L. (2016). The libRadtran software package for radiative transfer calculations (version 2.0.1). *Geoscientific Model Development*, 9(5):1647–1672.

Fabel, Y., Nouri, B., Wilbert, S., Blum, N., Triebel, R., Hasenbalg, M., Kuhn, P., Zarzalejo, L. F., and Pitz-Paal, R. (2022). Applying self-supervised learning for semantic cloud segmentation of all-sky images. *Atmospheric Measurement Techniques*, 15(3):797–809.

Geschäftsstelle der Arbeitsgruppe Erneuerbare Energien-Statistik (AGEE-Stat) am Umweltbundesamt (2023). Erneuerbare Energien in Deutschland - Daten zur Entwicklung im Jahr 2022. Technical report, Umweltbundesamt.

Gouvêa, E., Sobrinho, P., and Souza, T. (2017). Spectral Response of Polycrystalline Silicon Photovoltaic Cells under Real-Use Conditions. *Energies*, 10(8):1178.

Gregor, P., Zinner, T., Jakub, F., and Mayer, B. (2023). Validation of a camera-based intra-hour irradiance nowcasting model using synthetic cloud data. *Atmospheric Measurement Techniques*, 16(12):3257–3271.

Grob, H., Emde, C., Wiegner, M., Seefeldner, M., Forster, L., and Mayer, B. (2020). The polarized Sun and sky radiometer SSARA: design, calibration, and application for ground-based aerosol remote sensing. *Atmospheric Measurement Techniques*, 13(1):239–258.

Hammer, A., Kühnert, J., Weinreich, K., and Lorenz, E. (2015). Short-term forecasting of surface solar irradiance based on Meteosat-SEVIRI data using a nighttime cloud index. *Remote Sensing*, 7(7):9070–9090.

Hasenbalg, M., Kuhn, P., Wilbert, S., Nouri, B., and Kazantzidis, A. (2020). Benchmarking of six cloud segmentation algorithms for ground-based all-sky imagers. *Solar Energy*, 201(March):596–614.

Hay, J. E. (1993). Calculating solar radiation for inclined surfaces: Practical approaches. *Renewable Energy*, 3(4-5):373–380.

He, K., Zhang, X., Ren, S., and Sun, J. (2015). Deep Residual Learning for Image Recognition. *Proceedings of the IEEE Computer Society Conference on Computer Vision and Pattern Recognition*, 2016-Decem:770–778.

Hersbach, H., Bell, B., Berrisford, P., Biavati, G., Horányi, A., Muñoz Sabater, J., Nicolas, J., Peubey, C., Radu, R., Rozum, I., Schepers, D., Simmons, A., Soci, C., Dee, D., and Thépaut, J.-N. (2023). ERA5 hourly data on single levels from 1959 to present.

Hillaire, S. (2016). Physically Based Sky, Atmosphere and Cloud Rendering in Frostbite. *SIGGRAPH 2016 Course*.

Holben, B. N., Eck, T. F., Slutsker, I., Tanré, D., Buis, J. P., Setzer, A., Vermote, E., Reagan, J. A., Kaufman, Y. J., Nakajima, T., Lavenu, F., Jankowiak, I., and Smirnov, A. (1998). AERONET - A federated instrument network and data archive for aerosol characterization. *Remote Sensing of Environment*, 66(1):1–16.

Hottel, H. C. and Woertz, B. B. (1942). The Performance of Flat-Plate Solar-Heat Collectors. *Transactions of the American Society of Mechanical Engineers*, 64(2):91–103.

Hu, Y., Song, R., and Li, Y. (2016). Efficient Coarse-to-Fine Patch Match for Large Displacement Optical Flow. In *2016 IEEE Conference on Computer Vision and Pattern Recognition (CVPR)*, volume 2016-Decem, pages 5704–5712. IEEE.

Inman, R. H., Pedro, H. T., and Coimbra, C. F. (2013). Solar forecasting methods for renewable energy integration. *Progress in Energy and Combustion Science*, 39(6):535–576.

ISO/TR 9901 (2021). Solar energy – Pyranometers – Recommended practice for use. Standard, International Organization for Standardization, Geneva, CH.

Jakub, F. and Gregor, P. (2022). UCLA-LES shallow cumulus dataset with 3D cloud output data.

Katiraei, F. and Agüero, J. R. (2011). Solar PV integration challenges. *IEEE Power and Energy Magazine*, 9(3):62–71.

Katsafados, P., Mavromatidis, E., and Spyrou, C. (2022). *Numerical Weather Prediction and Data Assimilation*. Wiley.

Kazantzidis, A., Tzoumanikas, P., Blanc, P., Massip, P., Wilbert, S., and Ramirez-Santigosa, L. (2017). Short-term forecasting based on all-sky cameras. In *Renewable Energy Forecasting*, number Ccd, pages 153–178. Elsevier.

Kingma, D. P. and Ba, J. (2014). Adam: A Method for Stochastic Optimization. *3rd International Conference on Learning Representations, ICLR 2015 - Conference Track Proceedings*, pages 1–15.

Kölling, T., Zinner, T., and Mayer, B. (2019). Aircraft-based stereographic reconstruction of 3-D cloud geometry. *Atmospheric Measurement Techniques*, 12(2):1155–1166.

Kuchler, T. M. (1979). Evaluation of models to predict insolation on tilted surfaces. *Solar Energy*, 23:111–114.

Kuhn, P., Nouri, B., Wilbert, S., Hanrieder, N., Prahl, C., Ramirez, L., Zarzalejo, L., Schmidt, T., Yasser, Z., Heinemann, D., Tzoumanikas, P., Kazantzidis, A., Kleissl, J., Blanc, P., and Pitz-Paal, R. (2019). Determination of the optimal camera distance for cloud height measurements with two all-sky imagers. *Solar Energy*, 179(September 2018):74–88.

Kuhn, P., Wilbert, S., Prahl, C., Schüler, D., Haase, T., Hirsch, T., Wittmann, M., Ramirez, L., Zarzalejo, L., Meyer, A., Vuilleumier, L., Blanc, P., and Pitz-Paal, R. (2017a). Shadow camera system for the generation of solar irradiance maps. *Solar Energy*, 157:157–170.

Kuhn, P., Wilbert, S., Schüler, D., Prahl, C., Haase, T., Ramirez, L., Zarzalejo, L., Meyer, A., Vuilleumier, L., Blanc, P., Dubrana, J., Kazantzidis, A., Schroedter-Homscheidt, M., Hirsch, T., and Pitz-Paal, R. (2017b). Validation of spatially resolved all sky imager derived DNI nowcasts. In *AIP Conference Proceedings*, volume 1850, page 140014.

Kuhn, P., Wirtz, M., Killius, N., Wilbert, S., Bosch, J. L., Hanrieder, N., Nouri, B., Kleissl, J., Ramirez, L., Schroedter-Homscheidt, M., Heinemann, D., Kazantzidis, A., Blanc, P., and Pitz-Paal, R. (2018). Benchmarking three low-cost, low-maintenance cloud height measurement systems and ECMWF cloud heights against a ceilometer. *Solar Energy*, 168(February):140–152.

Kurtz, B., Mejia, F., and Kleissl, J. (2017). A virtual sky imager testbed for solar energy forecasting. *Solar Energy*, 158(May):753–759.

Kurucz, R. L. (1994). Synthetic Infrared Spectra. *Symposium - International Astronomical Union*, 154(13):523–531.

Law, E. W., Kay, M., and Taylor, R. A. (2016). Evaluating the benefits of using short-term direct normal irradiance forecasts to operate a concentrated solar thermal plant. *Solar Energy*, 140:93–108.

Le Dimet, F.-X. and Talagrand, O. (1986). Variational algorithms for analysis and assimilation of meteorological observations: theoretical aspects. *Tellus A: Dynamic Meteorology and Oceanography*, 38(2):97–110.

Lenoble, J., Herman, M., Deuzé, J., Lafrance, B., Santer, R., and Tanré, D. (2007). A successive order of scattering code for solving the vector equation of transfer in the earth's atmosphere with aerosols. *Journal of Quantitative Spectroscopy and Radiative Transfer*, 107(3):479–507.

Li, Q., Lu, W., and Yang, J. (2011). A hybrid thresholding algorithm for cloud detection on ground-based color images. *Journal of Atmospheric and Oceanic Technology*, 28(10):1286–1296.

Liou, K. N. (2002). *An Introduction to Atmospheric Radiation*. International Geophysics. Elsevier Science.

Logothetis, S. A., Salamalikis, V., Wilbert, S., Remund, J., Zarzalejo, L. F., Xie, Y., Nouri, B., Ntavelis, E., Nou, J., Hendrikx, N., Visser, L., Sengupta, M., Pó, M., Chauvin, R., Grieu, S., Blum, N., van Sark, W., and Kazantzidis, A. (2022). Benchmarking of solar irradiance nowcast performance derived from all-sky imagers. *Renewable Energy*, 199(September):246–261.

Lohmann, U., Lüönd, F., and Mahrt, F. (2016). *An Introduction to Clouds: From the Microscale to Climate*. Cambridge University Press.

López-Cuesta, M., Aler-Mur, R., Galván-León, I. M., Rodríguez-Benítez, F. J., and Pozo-Vázquez, A. D. (2023). Improving Solar Radiation Nowcasts by Blending Data-Driven, Satellite-Images-Based and All-Sky-Imagers-Based Models Using Machine Learning Techniques. *Remote Sensing*, 15(9):2328.

Masuda, R., Iwabuchi, H., Schmidt, K. S., Damiani, A., and Kudo, R. (2019). Retrieval of Cloud Optical Thickness from Sky-View Camera Images using a Deep Convolutional Neural Network based on Three-Dimensional Radiative Transfer. *Remote Sensing*, 11(17):1962.

Mavromatakis, F., Kavoussanaki, E., Vignola, F., and Franghiadakis, Y. (2014). Measuring and estimating the temperature of photovoltaic modules. *Solar Energy*, 110:656–666.

Mayer, B. (2009). Radiative transfer in the cloudy atmosphere. *The European Physical Journal Conferences*, 1:75–99.

Mayer, B. and Kylling, A. (2005). Technical note: The libRadtran software package for radiative transfer calculations - description and examples of use. *Atmospheric Chemistry and Physics*, 5(7):1855–1877.

Motamedi, M., Rastegar, S., LeCarpentier, G., and Welch, A. J. (1989). Light and temperature distribution in laser irradiated tissue: the influence of anisotropic scattering and refractive index. Technical Report 12.

Nakajima, T. and King, M. D. (1990). Determination of the Optical Thickness and Effective Particle Radius of Clouds from Reflected Solar Radiation Measurements. Part I: Theory. *Journal of the Atmospheric Sciences*, 47(15):1878–1893.

Nakajima, T. Y. and Nakajma, T. (1995). Wide-Area Determination of Cloud Microphysical Properties from NOAA AVHRR Measurements for FIRE and ASTEX Regions. *Journal of the Atmospheric Sciences*, 52(23):4043–4059.

Neggers, R. A. J., Duynkerke, P. G., and Rodts, S. M. A. (2003). Shallow cumulus convection: A validation of large-eddy simulation against aircraft and Landsat observations. *Quarterly Journal of the Royal Meteorological Society*, 129(593):2671–2696.

Nguyen, D. A. and Kleissl, J. (2014). Stereographic methods for cloud base height determination using two sky imagers. *Solar Energy*, 107:495–509.

Nouri, B., Blum, N., Wilbert, S., and Zarzalejo, L. F. (2022). A Hybrid Solar Irradiance Nowcasting Approach: Combining All Sky Imager Systems and Persistence Irradiance Models for Increased Accuracy. *Solar RRL*, 6(5):1–12.

Nouri, B., Kuhn, P., Wilbert, S., Prahl, C., Pitz-Paal, R., Blanc, P., Schmidt, T., Yasser, Z., Santigosa, L. R., and Heineman, D. (2018). Nowcasting of DNI maps for the solar field based on voxel carving and individual 3D cloud objects from all sky images. *AIP Conference Proceedings*, 2033(November).

Nouri, B., Wilbert, S., Kuhn, P., Hanrieder, N., Schroedter-Homscheidt, M., Kazantzidis, A., Zarzalejo, L., Blanc, P., Kumar, S., Goswami, N., Shankar, R., Affolter, R., and Pitz-Paal, R. (2019a). Real-time uncertainty specification of all sky imager derived irradiance nowcasts. *Remote Sensing*, 11(9).

Nouri, B., Wilbert, S., Segura, L., Kuhn, P., Hanrieder, N., Kazantzidis, A., Schmidt, T., Zarzalejo, L., Blanc, P., and Pitz-Paal, R. (2019b). Determination of cloud transmittance for all sky imager based solar nowcasting. *Solar Energy*, 181(December 2018):251–263.

Paletta, Q., Arbod, G., and Lasenby, J. (2022). Omnivision forecasting: combining satellite observations with sky images for improved intra-hour solar energy predictions.

Paletta, Q., Arbod, G., and Lasenby, J. (2023). Omnivision forecasting: Combining satellite and sky images for improved deterministic and probabilistic intra-hour solar energy predictions. *Applied Energy*, 336(January):120818.

Paszke, A., Gross, S., Massa, F., Lerer, A., Bradbury, J., Chanan, G., Killeen, T., Lin, Z., Gimelshein, N., Antiga, L., Desmaison, A., Kopf, A., Yang, E., DeVito, Z., Raison, M., Tejani, A., Chilamkurthy, S., Steiner, B., Fang, L., Bai, J., and Chintala, S. (2019). PyTorch: An Imperative Style, High-Performance Deep Learning Library. In Wallach, H., Larochelle, H., Beygelzimer, A., d\textquotesingle Alché-Buc, F., Fox, E., and Garnett, R., editors, *Advances in Neural Information Processing Systems 32*, pages 8024–8035. Curran Associates, Inc.

Peng, Z., Yu, D., Huang, D., Heiser, J., Yoo, S., and Kalb, P. (2015). 3D cloud detection and tracking system for solar forecast using multiple sky imagers. *Solar Energy*, 118:496–519.

Perez, R., Stewart, R., Seals, R., and Guertin, T. (1988). The Development and Verification of the Perez Diffuse Radiation Model. *Sandia National Labs.: Albuquerque, NM, USA; State University of New York: Albany, NY, USA*, (October):176.

Planck, M. (1901). Ueber das Gesetz der Energieverteilung im Normalspectrum. *Annalen der Physik*, 309(3):553–563.

Pu, Z. and Kalnay, E. (2019). *Numerical Weather Prediction Basics: Models, Numerical Methods, and Data Assimilation*.

Pulkkinen, S., Nerini, D., Pérez Hortal, A. A., Velasco-Forero, C., Seed, A., Germann, U., and Foresti, L. (2019). Pysteps: an open-source Python library for probabilistic precipitation nowcasting (v1.0). *Geoscientific Model Development*, 12(10):4185–4219.

Quesada-Ruiz, S., Chu, Y., Tovar-Pescador, J., Pedro, H. T. C., and Coimbra, C. F. M. (2014). Cloud-tracking methodology for intra-hour DNI forecasting. *Solar Energy*, 102:267–275.

Ravuri, S., Lenc, K., Willson, M., Kangin, D., Lam, R., Mirowski, P., Fitzsimons, M., Athanassiadou, M., Kashem, S., Madge, S., Prudden, R., Mandhane, A., Clark, A., Brock, A., Simonyan, K., Hadsell, R., Robinson, N., Clancy, E., Arribas, A., and Mohamed, S. (2021). Skilful precipitation nowcasting using deep generative models of radar. *Nature*, 597(7878):672–677.

Rayleigh, L. J. S. (1871). XV. On the light from the sky, its polarization and colour. *The London, Edinburgh, and Dublin Philosophical Magazine and Journal of Science*, 41(271):107–120.

Richardson, W., Cañadillas, D., Moncada, A., Guerrero-Lemus, R., Shephard, L., Vega-Avila, R., and Krishnaswami, H. (2019). Validation of All-Sky Imager Technology and Solar Irradiance Forecasting at Three Locations: NREL, San Antonio, Texas, and the Canary Islands, Spain. *Applied Sciences*, 9(4).

Rodríguez-Benítez, F. J., López-Cuesta, M., Arbizu-Barrena, C., Fernández-León, M. M., Pamos-Ureña, M. Á., Tovar-Pescador, J., Santos-Alamillos, F. J., and Pozo-Vázquez, D. (2021). Assessment of new solar radiation nowcasting methods based on sky-camera and satellite imagery. *Applied Energy*, 292(March):116838.

Russakovsky, O., Deng, J., Su, H., Krause, J., Satheesh, S., Ma, S., Huang, Z., Karpathy, A., Khosla, A., Bernstein, M., Berg, A. C., and Fei-Fei, L. (2014). ImageNet Large Scale Visual Recognition Challenge.

Saleh, M., Meek, L., Masoum, M. A., and Abshar, M. (2018). Battery-less short-term smoothing of photovoltaic generation using sky camera. *IEEE Transactions on Industrial Informatics*, 14(2):403–414.

Samu, R., Calais, M., Shafiullah, G. M., Moghbel, M., Shoeb, M. A., Nouri, B., and Blum, N. (2021). Applications for solar irradiance nowcasting in the control of microgrids: A review. *Renewable and Sustainable Energy Reviews*, 147(December 2020):111187.

Schmetz, J., Pili, P., Tjemkes, S., Just, D., Kerkmann, J., Rota, S., and Ratier, A. (2002). An Introduction to Meteosat Second Generation (MSG). *Bulletin of the American Meteorological Society*, 83(7):977–992.

Schmidt, T., Kalisch, J., Lorenz, E., and Heinemann, D. (2016). Evaluating the spatiooral performance of sky-imager-based solar irradiance analysis and forecasts. *Atmospheric Chemistry and Physics*, 16(5):3399–3412.

Schneider, A. (2015). The Real-time Volumetric Cloudscapes of Horizon: Zero Dawn. *SIGGRAPH 2015 Course*.

Schneider, A. (2018). Real-time volumetric cloudscapes. In *GPU Pro 360 Guide to Lighting*, pages 473–504. AK Peters/CRC Press.

Shields, J., Karr, M., Burden, A., Johnson, R., Mikuls, V., Streeter, J., and Hodgkiss, W. (2009). Research toward Multi-site Characterization of Sky Obscuration by Clouds, Final Report for GrantN00244-07-1-009. Technical report, Marine Physical Laboratory, Scripps Institution of Oceanography, University of California,, San Diego, USA.

Sirch, T. (2018). Multi-resolution nowcasting of clouds and DNI with MSG/SEVIRI for an optimized operation of concentrating solar power plants.

Sirch, T., Bugliaro, L., Zinner, T., Möhrlein, M., and Vazquez-Navarro, M. (2017). Cloud and DNI nowcasting with MSG/SEVIRI for the optimized operation of concentrating solar power plants. *Atmospheric Measurement Techniques*, 10(2):409–429.

Song, S., Yang, Z., Goh, H. H., Huang, Q., and Li, G. (2022). A novel sky image-based solar irradiance nowcasting model with convolutional block attention mechanism. *Energy Reports*, 8:125–132.

Stamnes, K., Tsay, S.-C., Wiscombe, W., and Jayaweera, K. (1988). Numerically stable algorithm for discrete-ordinate-method radiative transfer in multiple scattering and emitting layered media. *Applied Optics*, 27(12):2502.

Stephens, G. L. (1994). Remote sensing of the lower atmosphere: An introduction. In *Remote sensing of the lower atmosphere: An introduction*, page 523 pp. Oxford University Press, New York.

Stevens, B., Moeng, C.-H., Ackerman, A. S., Bretherton, C. S., Chlond, A., de Roode, S., Edwards, J., Golaz, J.-C., Jiang, H., Khairoutdinov, M., Kirkpatrick, M. P., Lewellen, D. C., Lock, A., Müller, F., Stevens, D. E., Whelan, E., and Zhu, P. (2005). Evaluation of Large-Eddy Simulations via Observations of Nocturnal Marine Stratocumulus. *Monthly Weather Review*, 133(6):1443–1462.

Strandgren, J., Bugliaro, L., Sehnke, F., and Schröder, L. (2017). Cirrus cloud retrieval with MSG/SEVIRI using artificial neural networks. *Atmospheric Measurement Techniques*, 10(9):3547–3573.

Tola, E., Lepetit, V., and Fua, P. (2010). DAISY: An Efficient Dense Descriptor Applied to Wide-Baseline Stereo. *IEEE Transactions on Pattern Analysis and Machine Intelligence*, 32(5):815–830.

Vicente, G. A., Davenport, J. C., and Scofield, R. A. (2002). The role of orographic and parallax corrections on real time high resolution satellite rainfall rate distribution. *International Journal of Remote Sensing*, 23(2):221–230.

Wang, P., van Westrhenen, R., Meirink, J. F., van der Veen, S., and Knap, W. (2019). Surface solar radiation forecasts by advecting cloud physical properties derived from Meteosat Second Generation observations. *Solar Energy*, 177(August 2018):47–58.

West, S. R., Rowe, D., Sayeef, S., and Berry, A. (2014). Short-term irradiance forecasting using skycams: Motivation and development. *Solar Energy*, 110:188–207.

Xie, W., Liu, D., Yang, M., Chen, S., Wang, B., Wang, Z., Xia, Y., Liu, Y., Wang, Y., and Zhang, C. (2020). SegCloud: A novel cloud image segmentation model using a deep convolutional neural network for ground-based all-sky-view camera observation. *Atmospheric Measurement Techniques*, 13(4):1953–1961.

Ye, L., Cao, Z., and Xiao, Y. (2017). DeepCloud: Ground-Based Cloud Image Categorization Using Deep Convolutional Features. *IEEE Transactions on Geoscience and Remote Sensing*, 55(10):5729–5740.

Zdunkowski, W., Trautmann, T., and Bott, A. (2014). *Radiation in the Atmosphere*. Cambridge University Press.

Zhu, C., Byrd, R. H., Lu, P., and Nocedal, J. (1997). Algorithm 778: L-BFGS-B. *ACM Transactions on Mathematical Software*, 23(4):550–560.

Acknowledgements

First and foremost I would like to thank my supervisors Bernhard Mayer and Tobias Zinner for their continuous support and help throughout this work. I am grateful that you gave me the opportunity to work on this topic and guided me in fruitful discussions and with experienced advise while leaving room for me to explore new techniques and aspects. Thank you for your patience with me, e.g. on the many occasions when my explanations were confusing to anyone else than me or even myself.
I thank Fabian Jakub for sharing his expertise and thoughts on many aspects of this work outside of it. The LES runs, which are a fundamental part of this work, were run and provided by Fabian Jakub. I greatly value the on- and off-topic discussions with you and learned a lot, formally and informally.
I greatly value the help and advise of Markus Garhammer with the measurement side of this work. Without the support and experience of him and also Anton Lex, Meinhard Seefeldner, and Tobias Zinner the measurements would have been a lot more demanding.
Also, I want to thank my colleagues for the cooperative, friendly and inspiring working environment at the institute. This includes all of the colleagues mentioned above, my office mates and all others that shared thoughts, a smile, and a good time with me. Thanks to all colleagues helping in the image labeling for the training of the cloud mask CNN.
I greatly value the support of Dr. Josef Schreder on behalf of the CMS - Ing. Dr. Schreder GmbH, who lent the ASI-16142 to the institute for this work and helped with his experience on all-sky imagers.
I thank Christoph Wörl, Martin Sieber and Herbert Grundler, the owners and operators of the PV and biogas plant in Egling a.d. Paar for providing access to the PV plant and their support throughout the measurements. It was always a joy meeting one of you.
Last but not least, I am thankful for the support from my friends and family throughout the last decades and years. Thank you, Katrin Wolf for your support and also for helping me to improve the layout of this work. I also greatly value the input of Alexandra Mangold, who proof-read several parts and versions of this document.
This work was funded through the Fachagentur Nachwachsende Rohstoffe e.V. project NETFLEX (FKZ22400318) on behalf of the German Federal Ministry of Food and Agriculture (BMEL).
I hope I could give something back for all the support.

Transparency The software WriteFull, LanguageTool and Grammarly were used to improve the grammar and language in this work.